Optimization of CT Scanning and Reconstruction for Clinical Ear Imaging

by

Mag. Karin Eibenberger BSc.

Presented to the Faculty of Health and Social Sciences of the
University of Applied Sciences Upper Austria
in Partial Fulfillment of the Requirements
for the Degree of

Master of
Science in Engineering
(Dipl. Ing.)

Baltimore – Waidhofen/Ybbs
June 28th 2012

Advisors

Prof. John Carey, MD
Johns Hopkins University School of Medicine, Baltimore, MD, USA
Department of Otolaryngology and Head and Neck Surgery

Prof. (FH) PD Dr. Thomas Haslwanter
University of Applied Sciences Upper Austria, School of Applied Health and Social Services
Department of Medical Engineering, Linz, Austria

Declaration of Authorship

I hereby declare and confirm that this thesis is entirely the result of my own original work. Where other sources of information have been used, they have been indicated as such and properly acknowledged. I further declare that this or similar work has not been submitted for credit elsewhere.

Baltimore – Waidhofen/Ybbs
June 28th, 2012

_____
Karin Eibenberger

Acknowledgements

Quite frankly, without my advisor Thomas Haslwanter, I would not have continued my studies at the University with the Master's program in biomedical engineering. Instead, I would now live a real business life, earn real money and would have real holidays and maybe even free time on the weekends. And I would live a boring life. I cannot explain in words how deeply grateful I am that I had the opportunity to learn from him and to work with such a professional researcher. I'm still impressed by his experience, creativity, knowledge, dedication and energy. I wish there would be more people like him.

He also made my research stay at Johns Hopkins possible which was I guess the best experience of my entire life (besides my first motorcycle ride). I could hardly fight against the tears when I had to leave – and this was true for two reasons: First, I loved my work there. Second, I was not only whole-heartedly welcomed at the Department of Otolaryngology, I was fully integrated and became part of the team. I was not just a stupid engineering student. And I had the same luck as in Austria: I got the best advisor I can think of: John Carey. I learned so much from him that I came back as a different person. And he is not only a fantastic researcher but also probably one of the only physicians who understands technical issues and is able to combine two worlds. I'm not only deeply impressed by the trust and faith he had in me, but also by his kind and generous nature – if I had to choose a role model, it would probably be him. I'm very happy to have met and worked with him. Oh, and he always knew when it was time to get me a coffee.

Then there is Bernhard – of course! – my loving husband, best friend, lover, long term partner and the best belayer I can think of while I'm on lead. I know he will always catch me should I fall. Thanks for coming with me to Baltimore and to work with me through nights, days and sunny weekends.

And then all the others! Thanks to all of them – they made my stay so fantastic as it was: Dale Roberts (high five for the chair project!), David Zee, Geraldine Zuniga-Manrique, Marcela Davalos-Bichara, Tina Ehtiati, James Dolberg, Jeff Siewerdsen, Michael Schubert, Adrian Lasker, Beatriz Kohler, Georgios Mantokoudis, Angela Wenzel, Carolina Trevino, Bryan Ward, Bryan Woodhead, Jay Burns, Peter Elfert, Phillippe Gailloud, Mohamed Lehar, Charley della Santina and Richard Penninger, my predecessor. Again, thanks to all of you and I hope you enjoy the Karin&Bernhard coffee fund. Finally I want to thank my parents who supported us to manage our stay in Baltimore and who are always so proud on what I'm doing. Sorry for hiking the West Coast Trail and the Alaskan wilderness, but the black bears weren't even after us (at least not on the West Coast Trail). So nothing to worry about.

Abstract

Semicircular Canal Dehiscence (SCD) is a symptom where the upper part of the superior semicircular canal of the vestibular system is either very thin or open. This causes clinical symptoms like massive vertigo or patients hearing their own heart beat or their eyes move. Multi Slice Computed Tomography (MSCT) is the gold standard for the diagnosis of SCD. However, recent studies (Penninger et al. 2011; Tavassolie et al. 2012) have shown that due to partial volume averaging and filtering MSCT might overestimate the size of the dehiscence of the canal. It has also been extensively studied that Cone Beam Computed Tomography (CBCT) might provide a better spatial resolution for the application of temporal bone scans (Damstra et al. 2011; Fahrig et al. 2006; Kau et al. 2009; Miracle and Mukherji 2009b; Peltonen et al. 2009). Most of these studies are human observer-based giving just qualitative results. In our study we developed an algorithm to quantitatively compare the spatial resolution of CT scans of MSCT and CBCT. We used bone cement phantoms with holes of different diameters to show that we can distinguish between image noise and hole by comparing the standard deviations of different regions of interest. Then we prepared a human head specimen and thinned the superior canal to create an artificial dehiscence with a very thin layer of bone overlying the canal. On the basis of scans with the head specimen we developed an algorithm to process a 3D DICOM stack of dehiscence scans so that we can do the same statistical evaluation on the upper part or the superior canal to find out if there is still bone overlying the canal.

Kurzfassung

Eine Dehiszenz des Superior Kanals – *Semicircular Dehiscence Sdyndrome* (SCDS) – ist ein Symptom des Vestibularorgans, das auf Grund einer Verdünnung beziehungsweise auf Grund des Fehlens der obersten Knochenschicht des betroffenen Kanals auftritt. Klinische Symptome dafür sind massive Schwindelprobleme. Manche Patienten hören zum Beispiel auch ihren eigenen Herzschlag sehr laut; oder ihre Augenbewegungen. Der Gold Standard für die Diagnose der Dehiszenz ist Multi-Slice Computertomographie (MSCT). In letzter Zeit wurden allerdings Studien publiziert, die eine Überbewertung der Größe der Dehiszenz durch MSCT nachweisen(Penninger et al. 2011; Tavassolie et al. 2012). Gleichzeitig wurde der neuen Technik der Cone Beam Computertomographie (CBCT) ein besseres Auflösungsvermögen bestätigt, was vor allem für Scans am Schläfenbein interessant ist (Damstra et al. 2011; Fahrig et al. 2006; Kau et al. 2009; Miracle and Mukherji 2009b; Peltonen et al. 2009). Die meisten der oben genannten Studien basieren auf der Befragung von Beobachtern und nur auf qualitativen Maßstäben. Wir haben nun ein Verfahren und Algorithmen entwickelt, um die Scans von verschiedenen CT Techniken (MSCT und CBCT) quantitativ miteinander zu vergleichen. Die Entwicklung der Analyseverfahren fand mit Hilfe von Knochenzement-Phantomen statt. Mit unseren Algorithmen konnten wir mit statistischer Aussagekraft Löcher in den Phantomen vom Rauschen des Scans unterscheiden. In weiterer Folge präparierten wir einen menschlichen Kadaverschädel und dünnten den obersten Kanal aus um eine künstliche Dehiszenz zu erzeugen. Auf Basis von diesen Kadaverscans entwickelten wir dann einen Algorithmus um ein DICOM 3D Volumen soweit zu bearbeiten, dass die selbe statistische Auswertung wie mit den Knochenzementphantomen möglich wurde und wir die dünne Knochenschicht über dem Kanal noch nachweisen konnten.

Executive Summary

Semicircular Canal Dehiscence Syndrome (SCDS) is a symptom where the upper part of the superior canal of the vestibular system is thin or completely opened (Minor et al. 2001; Minor et al. 1998). This dehiscence causes clinical signs and symptoms: massive vertigo, eye movements after loud sound or pressure induced stimuli that align with the plane of the affected canals and hearing loss. Patients also suffer from hearing their own heart beat or their eyes move.

Beside clinical examinations like eye movement recordings or the recording of vestibular evoked myogenic potentials, the gold standard for the diagnosis of superior canal dehiscence is Multi Slice Computed Tomography (MSCT). However, recent studies showed that MSCT tend to overestimate the size of the dehiscence, sometimes even leading to a false=positive diagnosis with an unnecessary surgery as outcome (Penninger et al. 2011; Tavassolie et al. 2012). In addition, the novel technique of Cone Beam Computed Tomography (CBCT) provides better spatial resolution and is considered ideal for temporal bone scans (Damstra et al. 2011; Fahrig et al. 2006; Kau et al. 2009; Miracle and Mukherji 2009b; Peltonen et al. 2009). Most of the current studies which evaluate CBCT for temporal bone applications are human observer based, which can lead to bias by the observers and the viewing modalities like different workstations, DICOM viewers and screens. In our study, we developed an algorithm and approach to quantitatively assess and compare the spatial resolution of CT scans from different scanners like CBCT and MSCT.

To develop the algorithms, we made bone cement phantoms and inserted surgical sutures with different diameters (ranging from 0.1 to 0.4 mm). By generating slices orthogonal to the holes we could place a 5x5 pixel matrix over a hole and noise respectively. To compare hole vs. noise within such a 5x5 pixel matrix, the standard deviations can be compared with the Fligner-Killeen test for not normally distributed populations of data. We showed that every scanner – MSCT and CBCT – can resolve even the thinnest hole so that it is statistically different from image noise. The p-values to detect a 0.1 mm hole versus noise are 0.0052, 0.0079 and 0.0005 for a Toshiba MSCT, a Siemens CBCT and a Siemens High-resolution CBCT, respectively. In theory, the Siemens High-resolution CBCT should have the highest spatial resolution, but to detect very small structures, the noise level was found being too high. To overcome this problem, an optimization of the scanning parameters (tube current, tube voltage, beam hardening, dose and reconstruction parameters) is proposed. Another method is using noise reduction filters or averaging over multiple DICOM slices.

After showing that small holes on CT scans can be detected with statistical methods, we transferred this knowledge for analysis of SCD scans. To acquire scans of a SCDS case on different imaging modalities, we used a human cadaveric head specimen. We opened the head and thinned the bone of the superior canal of the right side of the head so that it was translucent, but still

intact. Then we developed an algorithm to process a 3D volume containing the superior semicircular canal to do the same analysis with this geometry. The approach can be described as a series of projections and rotations. The center of the canal is found by a optimized hole detection filter and a circle is fitted into it. The aim of this is to create a set of slices orthogonal to the upper part of the canal. From this slices, a path is cut out from the center of the canal towards the outside. With this, we could measure whether there is still bone overlying the canal or not.

Table of Contents

1. Preliminaries

A medical imaging system is a machine
that transforms people into numbers.
M. Kessler

This chapter deals with an informal introduction to the motivation of the study conducted at the Department of Otolaryngology and Head and Neck Surgery at the Johns Hopkins Hospital in Baltimore, Maryland, USA. It describes the aims and approach of the scientific work and the structure of this thesis.

1.1. Motivation

Our department, the *Department of Otolaryngology and Head and Neck Surgery* at the *Johns Hopkins University School of Medicine*, is famous for a long list of things, amongst them the quite young finding by Lloyd Minor (now provost of the Johns Hopkins School of Medicine) of a completely new syndrome: the *Superior (Semicircular) Canal Dehiscence Syndrome* (SCD) (Minor et al. 1998; Minor 2000). SCD is a condition where the superior canal in the bony labyrinth is connected to the posterior fossa, causing severe vertigo, unsteadiness, dizziness, hearing loss and pathologic eye movements. And 14 years after the first publication, Johns Hopkins is still the worldwide leading research group for the diagnosis and treatment of SCD, with John Carey, MD, now heading the research. Surgery on SCD patients is performed about every other week, and the number of patients diagnosed with these symptoms is steadily increasing. In fact, a temporal bone survey by (Carey et al. 2000) showed a prevalence of dehiscence of 0.5%. And a thinning of the bone overlying the superior semicircular canal was prevalent in 1.9%. Since Johns Hopkins has been voted *Best Hospital* in the United States for 21 years in a row (US News and Health Report 2011), it is not surprising that the most challenging and interesting patients come to this institution. This is also the case with canal dehiscence patients, where Johns Hopkins is famous for the diagnosis, treatment and post-op-rehabilitation. But still dehiscence is not easy to diagnose or treat, and even the best state-of-the-art medical devices – like high resolution Multi Slice Computer Tomography – cannot diagnose dehiscence with 100% certainty, leading occasionally to a false positive diagnosis and – in worst case – to surgery where no surgery is necessary (Penninger et al. 2011).

Besides his interest in SCD, John Carey also studies the effects of gentamicin injections on the vestibular function in patients with Meniere's disease. And Charley della Santina, who works at the same department, is one of the leading researchers in the new field of vestibular implants to restore vestibular functions for patients who have lost their labyrinth function. He also supervises the implantation of cochlear implants (CI), which are performed almost daily.

In order to diagnose SCD correctly, several conditions have to be documented prior to surgery. This includes strong complaints about vertigo and dizziness, combined with the finding of abnormal vestibular physiology, abnormal eye movements (e.g. pressure induced nystagmus and/or abnormal function on Head Impulse Tests (HIT) or Vestibular Evoked Myogenic Potentials (VEMP), hyperacusis and a CT scan showing or at least indicating the dehiscence. In fact, amongst all diagnosis tools, imaging is still the most important one, but with some drawbacks. Some CT modalities – i.e. Multi Slice CTs (MSCT) - tend to overestimate the size of the dehiscence and can in worst caste falsely indicate a dehiscence where there is none. It has already been shown that Cone Beam CT (CBCT) is superior to MSCT for the diagnosis of SCD (Penninger et al. 2011), (Tavassolie et al. 2012).

1.2. Aims and Approach

The aim of this thesis is to compare the results of different Computed Tomography imaging modalities, ranging from the (still) gold standard for diagnosis and image guidance, Multi Slice CT (MSCT), over the novel Cone Beam CT (CBCT) technique to the standard in high resolution imaging: Micro CT (µCT).

A first step was the analysis of CT scans of a bone cement phantom with drilled holes of various known diameters, providing another method of determining the actual accuracy of the different imaging systems.

To compare the different imaging techniques and the different scanners, a male cadaveric head specimen was used. Both ears were scanned; one control side and one side with an artificially thinned superior canal. After scanning the head on multiple CTs and with different imaging parameters and different reconstructions, the vestibular organs were surgically removed and scanned in a µCT. An algorithm was developed to quantitatively evaluate image quality and spatial resolution of different scanners. The thickness of the remaining bone overlying the superior canal was measured with statistical and image processing tools. This is not only feasible for measuring a dehiscence but also to evaluate the thicknesses of the stapes footplates – the stapes footplate, with a thickness of about 100 µm and the superstructure of the inner ear ossicles are usually hard to recognize on conventional CT and therefore a good measurement of the high resolution power of CBCT (and µCT as control measurement). The usage of the whole head specimen also guarantees a very accurate estimation of the patient radiation dose during scans, since other studies – conducted mainly on temporal bone specimen – cannot take their dose measurements into account; dose, as a product of kVp and mAs, is automatically adjusted by any clinical MSCT or CBCT.

In addition, three cadaveric temporal bones were drilled open and cochlear implants (CIs) were inserted. Another temporal bone specimen was provided with both, a cochlear implant and a vestibular implant. The question we want to answer with the CI scans is if it is possible to see the exact placement of the electrodes in the cochlea or canals. This can be of interest for intra-operative CT imaging, since re-implantation after electrode migration of CIs is still a problem (van der Marel et al. 2012).

1.3. Structure

The thesis emphasizes on the comparison of MSCT with CBCT and the high-accuracy μCT and proves that CBCT could be the new gold standard for any kind of inner ear imaging – from SCD over CI and other demands of clinical routine. Of interest are also the best modality settings for the imaging of dehiscence – as question answered by multiple scans on a cadaveric head specimen – from the best accuracy related to patient dose to the optimal secondary reconstruction algorithms on a newly by Siemens, Erlangen, developed 1x1 binning protocol and workstation for a CBCT combined with a metal artifact reduction algorithm suitable for high resolution imaging of CIs – eventually leading to new applications for intra-operative assessment and guidance during CI surgery or even vestibular implant procedures – where the exact placement of the stimulation electrodes is even more crucial than in regular CIs.

The thesis starts out with giving a background of the structure and function of the vestibular system, with an emphasis on the diagnosis and treatment of Superior Canal Dehiscence Syndrome. Then, the basics of Computed Tomography (CT) relevant for this thesis are explained. A focus is also set on the differences of Multi Slice CT and Cone Beam CT as well as on topics like dose, filtering, image quality and backprojection and reconstruction of CT images, as our scans were acquired with a newly developed 1x1 high resolution binning protocol and also compared to a clinical standard CBCT without the 1x1 binning.

Chapter three, the Methods section, presents the measurement equipment and the preparation of the specimen and phantoms, as well as the used scanner settings, the reconstruction algorithms and the software and tools used for data analysis. Chapter four explains the results in detail, and in Chapter five an outlook and conclusions are given, summarizing the study and the project at Johns Hopkins.

2. Introduction

2.1. The Vestibular System and Inner Ear

2.1.1. Structure and Function of the Vestibular System

Just like a multi axis accelerometer, our vestibular system senses head movement to hold images steady upon the retina and to provide us with information about movement and orientation in space. This *ocular gyroscopic function* (Leigh and Zee 1999) responds to both the angular (rotational) and linear (translational) components of head movements, but angular and linear motion are detected by two different subsystems: the *semicircular canals* and the *otolith organs*. Both are located in the petrous part of the *temporal bone*, right beside the *cochlea*, the auditory sensory organ – all of them build the so-called *membranous labyrinth* (Figure 1).

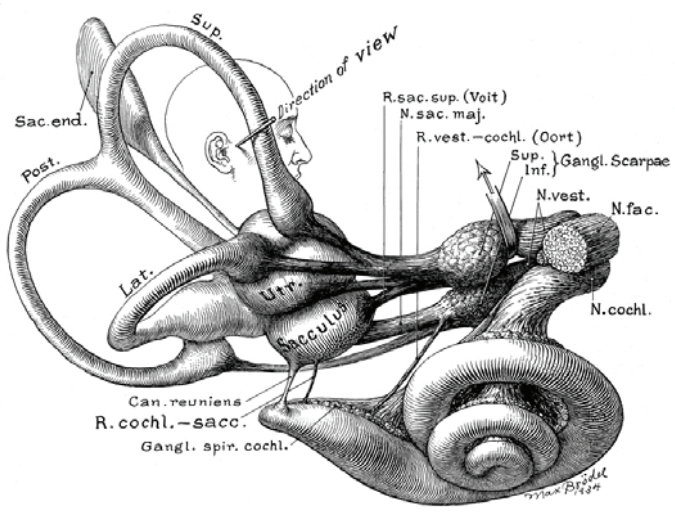

Figure 1 The vestibular and auditory sensory organs in the petrous part of the temporal bone (Brödel 1936).

The three semicircular canals are arranged in three approximately orthogonal planes and are sensitive to rotational acceleration. Each canal tube is filled with endolymph and presents a dilatation on one end, the membranous *ampulla*, containing the saddle-shaped *crista* and finally the gelatinous *cupula* (Figure 2A). The crista contains type I and type II hair cells and the processes of each hair cell consists of a number of *stereocilia* and one *kinocilium*. The cilia react to shearing forces; deflection of the stereocilia towards the kinocilium depolarizes and therefore excites the hair cell, deflection in the opposite direction causes hyperpolarization (inhibition).

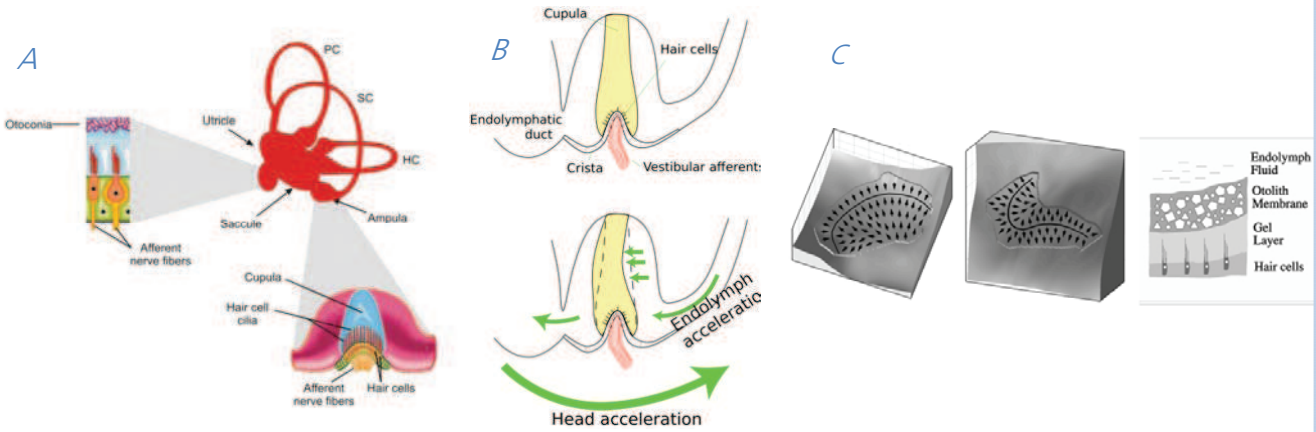

Figure 2A The vestibular system. PC: posterior canal, SC: superior canal, HC: horizontal canal (2007). B Cross section through the ampulla (Haslwanter 2011a). C Cross section of the otoliths (Haslwanter 2011b).

Head movement causes the fluid within the canals to lag behind and to bend the cupula, changing the otherwise constant discharge rate of the hair cells (Figure 2B). Due to the hydrodynamic properties of the endolymph in the canals – and mainly because of the increase in viscous properties of the fluid in the small diameter (< 0.3 mm) tubes (Curthoys et al. 1977) – the semicircular canals act basically as integrator, integrating the angular head acceleration signals and providing the brain with a head velocity signal.

In contrast, the otolith organs respond to linear accelerations with the maculae of sacculus and utriculus as their sensors. They sense both, direction and magnitude of gravity and transient linear accelerations due to movement. The hair cells of the maculae and their processes are embedded in a gelatinous membrane; attached to this are *otoconia*, calcium carbonate crystals. Sacculus and utriculus are both curved structures, and although the utricle lies approximately in the horizontal plane and the macula of the saccule in the parasagittal plane, they both sense linear accelerations in all three dimensions due to their shape (Figure 2A+C).

2.1.2. The Auditory System

The ear consists of three sections, divided into outer, middle and inner ear (Figure 3A). Whereas the outer ear is primarily responsible for the collection of sound and for performing spectral filtering for sound localization, the middle ear is responsible for impedance matching for an adequate energy transfer from sound waves in air to the fluid filled *cochlea*. Malleus, incus and stapes, the three *ossicles*, transmit the vibration from the *tympanic membrane* to the *oval window* at the base of the cochlear in the inner ear. The inner ear is responsible for the signal transformation from sound waves to electrophysiological action potentials and is the sensor part of the ear.

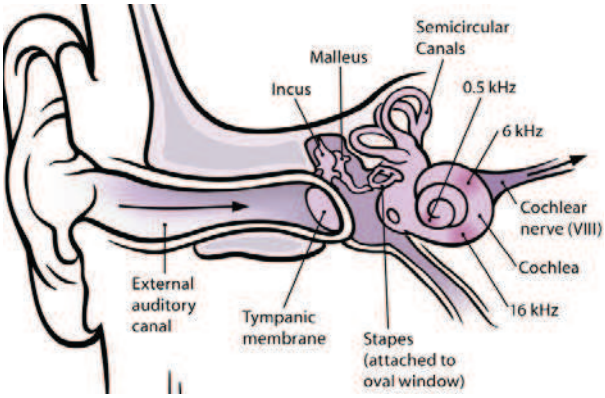

A

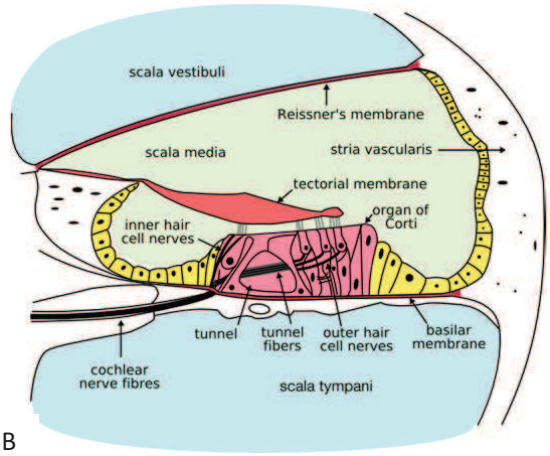

B

C

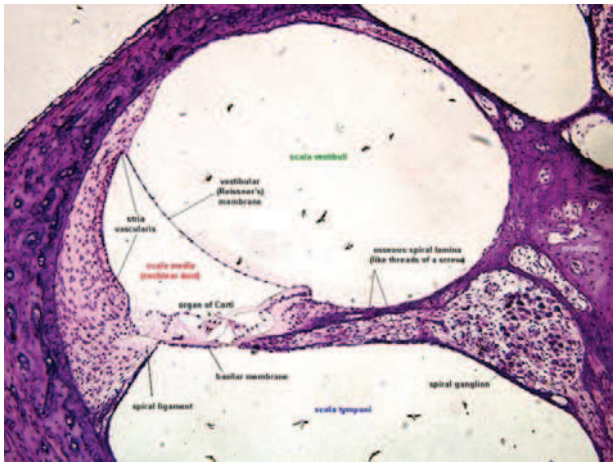

Figure 3A Anatomy of the human ear (Chittka and Brockmann 2005).B Cross section of the cochlea (Manske 2004). C Inner ear histology. (2011)

The cochlea has three sections, the *scala tympani, scala media* and *scala vestibuli* (Figure 3B). Inside the scala media and separated by *Reissner's membrane* lies the *organ of Corti* with its hair cells. The hair cells in the cochlea transform the deflection of the basilar membrane of the scala media into the final nerve signals, similar to the excitation of hair cells in the vestibular system. If the transduction of sound waves into the inner ear is impaired resulting in hearing loss, a cochlear implant can be implanted, stimulating the hair cells and the cochlear nerve fibers electrically instead of through the stretching or compressing due to the movement of the membrane causing the tip links to open ion channels producing a receptor potential.

2.2. Superior Canal Dehiscence Syndrome

Superior Semicircular Canal Dehiscence Syndrome (SCDS) is a condition of the inner ear which presents itself mostly in patients suffering from sound- and/or pressure induced vertigo. SCDS was first discovered by Lloyd B. Minor in 1995 and described by Lloyd B. Minor et al. in 1998, where a series of case studies of patients with a thinning or complete absence of the overlying temporal bone over the superior canal was reported (Minor et al. 1998). The patients were referred to the Johns Hopkins Outpatient Center in Baltimore, MD, USA, because of severe hearing and balance disorders.

2.2.1. Symptoms and Signs of SCDS

Dehiscence of bone overlying the superior canal leads to significant symptoms and signs induced by pressure or loud sound. Patients with this condition show transient vestibular hypersensitivity induced by loud sound – commonly known as *Tullio phenomenon* and first described around 80 years ago – or by pressure changes either at the external ear canal – known as *Hennebert sign* – or associated with *Valsalva maneuvers*[1] with evoked eye movements (Minor et al. 2001; Minor 2000; Minor 2005). The evoked vertical-torsional eye movements align with the plane of the dehiscent canal, which was shown using video goggles and magnetic scleral dual search coils for recording three dimensional eye movements (Minor et al. 2001). However, larger dehiscences with hypofunction in the affected semicircular canal can result in alignment of the evoked eye movements in other planes (Cremer et al. 2000). Patients also experience chronic disequilibrium and vertigo and may feel nauseated over a prolonged period. *Hyperacusis*, an over=sensitivity to certain frequency ranges of sound, is another typical sign of SCDS due to a better transformation of bone-conducted sound. On the other hand, hearing loss can be seen in a number of patients due to a decrease of air-conduction of sound. *Autophony*, the unusually loud hearing of a person's own voice, breathing and self-generated sounds, might occur. Patients have reported hearing their own heart beat or even their eye muscles move. Other symptoms are pulsatile tinnitus, positional vertigo, sound evoked head tilt and fatigue.

2.2.2. Pathophysiology

Normally, the labyrinth is encased by a dense layer of bone with only two points of increased compliance: the oval and the round window are the only openings in the hydrodynamic inner ear

[1] A Valsalva maneuver is an attempted exhalation against either pinched nostrils or against a closed glottis. Nose-pinched Valsalva forces air through the Eustachian tube and into the middle ear; glottic Valsalva increases the intrathoracic pressure and decreases the jugular venous return, raising the intracranial pressure.

system. Sound waves enter the inner ear through the oval window and the round window releases sound and the mechanical energy from the scala tympani.

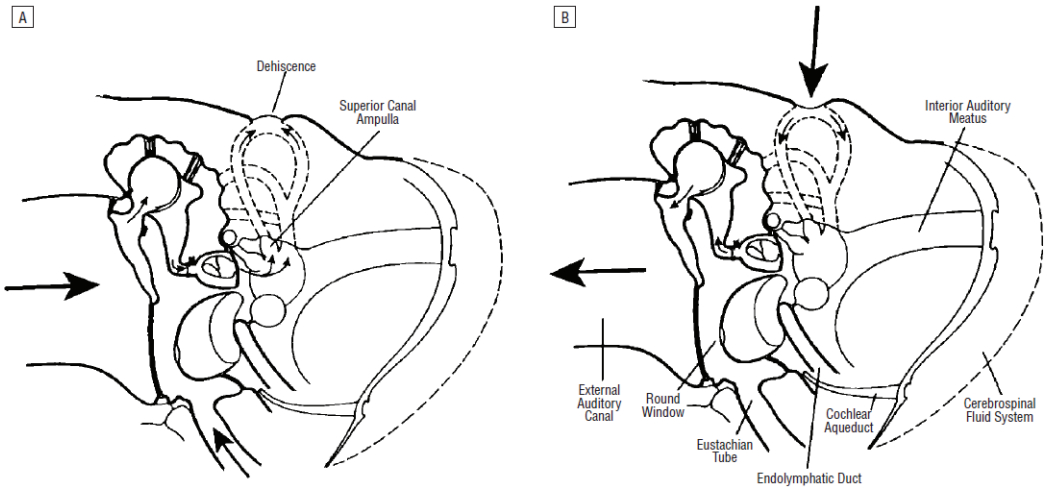

Figure 4 Schematic of Superior Semicircular Canal Dehiscence (Minor et al. 1998).

Traveling sound waves cause an inward bulging of the oval window which is in terms compensated through an outward bulging of the round window. With the condition of dehiscence, positive pressure in the external auditory canal causes bulging of the membranous canal into the cranial and *ampullofugal* flow. Negative pressure causes bulging of the cranial contents into the superior canal and *ampullopetal* flow (Minor and Carey 2010). The dehiscence of the superior canals is also referred to as a *third mobile window*, and an alternate route for sound and low-frequency pressure changes entering the labyrinth through the oval window (Carey et al. 2000). The resulting unregulated movements of the inner ear fluids resulting from loud sound stimuli cause an excitatory stimulus for the vestibular system during ampullofugal deflection of the superior semicircular canal cupula. Maneuvers like the Valsalva maneuver cause ampullopetal flow of the endolymph and result in inhibitory responses for the vestibular nerve.

2.2.3. Prevalence of SCDS

The true incidence of patients with Superior Semicircular Dehiscence Syndrome is yet unknown, but using a bone collection of over 1,000 temporal bones from 596 adults at the Johns Hopkins University School of Medicine, measurements of minimum bone thickness over the superior canal in 108 randomly chosen specimen revealed that a clear dehiscence of the superior canal was present in 0.5% of all temporal bone specimen (Carey et al. 2000). In addition, 1.4% of the scans showed a markedly thin bone overlying the superior canal (≤ 0.1 mm, significantly less than in measured control specimen). The study indicated that the thin layer of bone was such that it might appear dehiscent on even state-of-the-art ultra-high-resolution CT scans of the temporal bone. Sites

affected were in the middle fossa or a deep groove for the superior petrosal sinus, and dehiscence was often seen bilaterally. (Carey et al. 2000)

2.2.4. Diagnosis of SCDS

Since the first description of the symptoms of SCDS through Lloyd B. Minor, the diagnosis has been based upon the symptoms that are characteristic for the syndrome:

- the vertical-torsional eye movements evoked by pressure and/or sound which can be clinically observed using Frenzel goggles or videooculography
- lowered thresholds for responses to *vestibular evoked myogenic potentials* (VEMPs)
- audiograms and CT imaging of the temporal bone.

Patients coming to an outpatients center usually complain about *oscillopsia,* where objects appear to oscillated in the visual field, and dizziness and are asked whether they experience vertigo evoked by sound or induced by changes of the middle ear or intracranial pressure such as straining, sneezing, coughing – eventually combined with *hyperacusis,* an oversensitivity to sound (Minor et al. 2001).

Vestibular Evoked Myogenic Potentials (VEMPs)

Cervical vestibular evoked myogenic potentials (*cervical VEMPs*, cVEMPs) were first described by Colebatch (Colebatch et al. 1994). cVEMPs are now widely used for diagnosis of patients suffering from peripheral vestibular lesions. Usually, short clicks or tone bursts of around 500 Hz with intensities around 100 – 120 dB (Sound Pressure Level - SPL)[2] are used to evoke early P13-N23 potentials of the sterno-cleido-mastoid (SCM) muscle (Chiarovano et al. 2011) and trigger a vestibular-neck reflex which can be recorded using surface electrodes for electromyography (EMG). Generally speaking, the term *VEMPs* always refers to inhibitory potentials recorded in the contracting muscles. . Just like other evoked potentials, VEMPs are small signals that can only be detected by averaging over a series of stimuli. It is believed that the main pathway for the probably saccule-induced inhibitory postsynaptic potentials to the ipsilateral SCM motoneurons is the medial vestibulospinal tract which descends within the medial longitudinal fasciculus and is a marker for saccule and sacculo-spinal function (Shin et al. 2009; Halmagyi and Colebatch 1995; Welgampola et al. 2009; Curthoys et al. 2011).

Recently, a new method of VEMP tests has been developed which induces the same relaxation reflex on the extra-ocular muscles and is therefore called *ocular VEMP* (oVEMP) (Curthoys et al.

[2] Sound Pressure Level: 120dB (SPL) ≙ 20 Pa Sound Pressure ≙ 1 W/m^2 Sound Intensity

2011; Welgampola et al. 2008; Welgampola et al. 2009; Welgampola and Carey 2010). Again the stimulus can be air conducted sound in form of short tone bursts or clicks with frequencies around 500 Hz and 100 – 120 dB (SPL), or brisk taps on the forehead or mastoid with a reflex hammer or a special mechanical device (type Minishaker, Brüel & Kjær, Nærum, Denmark). Figure 5 shows the typical electrode placement and measurement procedure during clinical VEMP recordings.

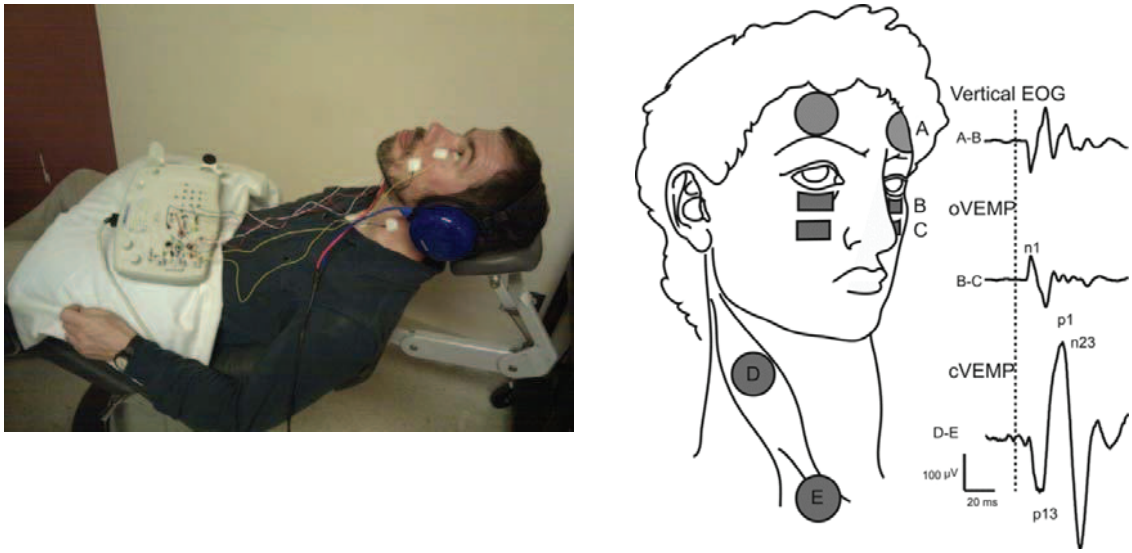

Figure 5A Subjectduring a VEMP recording at Johns Hopkins Hospital. B Montage of surface EMG electrodes during oVEMP and cVEMP recordings and according VEMP responses in normals (Welgampola et al. 2008).

Ocular VEMPs differ in their appearance from cervical VEMPs. oVEMPs are recorded from the contralateral extra ocular-muscle and in response to a typical stimulus consist of two early waves called n1-p1, differing from the p13-n23 waves both in polarity and peak-to-peak amplitude. Although still not certain, oVEMPs are considered a test for the assessment of utricle and utriculo-ocular pathway function (Welgampola et al. 2009).

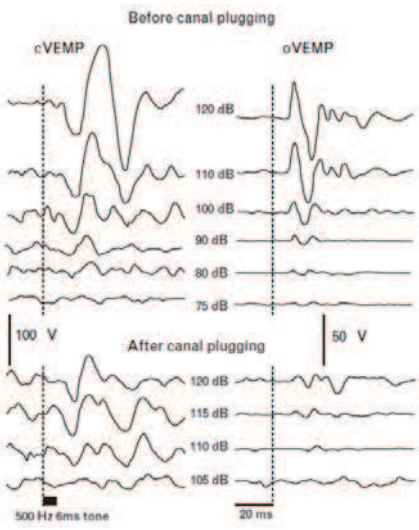

Figure 6 VEMP responses before and after SCD plugging. (Chien et al. 2011)

For the case of semicircular canal dehiscence, patients usually show very low thresholds in SPL for VEMP responses (Figure 6). Studies evaluating the oVEMP and cVEMP threshold pre- and post-surgery also show a significant difference comparing pre to post surgery data and compared to control subject with normal VEMP thresholds (Vanspauwen et al. 2006; Welgampola et al. 2008). VEMP testing is considered an upcoming new method for the diagnosis of SCD patients together with high resolution CT scans.

Click evoked VOR

It is known that loud sounds produce vestibular *nystagmus,* an involuntary jerky eye movement, in SCD patients. Furthermore, loud clicks also induce low-threshold, short latency vestibulo-ocular reflexes. Recent studies explored the parameters and conditions under which click-evoked VOR response can indicate a dehiscence in a patient (Aw et al. 2010; Aw et al. 2006; Brandt and Strupp 2010).

Figure 7 Dual scleral search coil experiment. Left picture: inserting the coil. Right picture: wires coming out of the eyes and adjustment of the coils.

In clinical routine, VOR examinations are usually performed either using Frenzel goggles or video oculography. However, the gold standard for eye movement recordings are still binocular dual magnetic scleral search coils (Figure 7). A series of case reports was shown by Cremer (Cremer et al. 2000) where they found out that during VOR recordings after loud tone bursts of patients with dehiscence, the evoked eye movement aligns with the plane of the abnormal canal. Usage of Video Oculography (VOG) systems for such recordings is currently under development; scleral search coil experiments are not feasible for daily routine diagnostic testing in an outpatient facility due to the effort and complexity of the test and the invasiveness of the eye coils.

Audiograms

Together with VEMP recordings, audiograms are still amongst the standard test for patients who are considered suffering from SCDS. Patients with a dehiscence typically experience conductive hearing loss and conductive hyperacusis caused by the artificial third mobile window.

High Resolution Computed Tomography

(Crane et al. 2008) showed that CT scans and multi planar reconstructions are the most sensitive test for the diagnosis of SCDS. Now, high resolution CT (HR-CT) scans are the gold standard for the diagnosis of dehiscence, although Multi-Slice CTs (MSCT) (still the gold standard amongst CT scans) tend to overestimate the size of the dehiscence (Penninger et al. 2011; Tavassolie et al. 2012) and can create an *artificial* dehiscence: due to partial volume averaging and filtering, thin bone might appear dehiscent on a scan. Partial volume averaging in this case means that in a CT scan, structures can lie only partly within a *voxel* (a discrete 3D volume element) or *pixel*, resulting in an averaging of the CT signal intensities in the adjacent voxel. Basics of Computed Tomography are explained in more detail in the next chapter. An increasing number of studies focus on the novel imaging technique of Cone Beam computed tomography (CBCT) for small area and interventional imaging. CBCT has advantages compared to MSCT like better spatial resolution, less radiation dose and faster volumetric image acquisition. Due to the coverage of the whole volume within (less than) one rotation it has also a decreased risks of motion artifacts (Chen and Ning 2002; Fahrig et al. 2006; Kapila et al. 2011; Ludlow and Ivanovic 2008; Peltonen et al. 2009; Ludlow and Ivanovic 2008; Vandenberghe et al. 2007).

2.3. Computed Tomography

The aim of this chapter is to give a short overview over the general principles of computed tomography (CT) to understand the work done within this thesis. The chapter starts with a quick introduction to x-ray and then goes into more detail when it comes to radiation and dose. The difference between Multi Slice CT and Cone Beam CT with flat panel detectors is explained. Furthermore, some insight is given regarding reconstruction algorithms and image analysis of DICOM images.

2.3.1. X-Ray Technology Introduction

Physically speaking, *x-rays* is a form of electromagnetic radiation with waves of a wavelength between 0.01 and 10 nanometers an energy from 100 eV to 100 keV; x-rays up to 10 keV are regarded as *soft* x-rays and from 10 to 120 keV as *hard* x-rays that can penetrate liquids and solids, but have an attenuation effect on the x-rays.

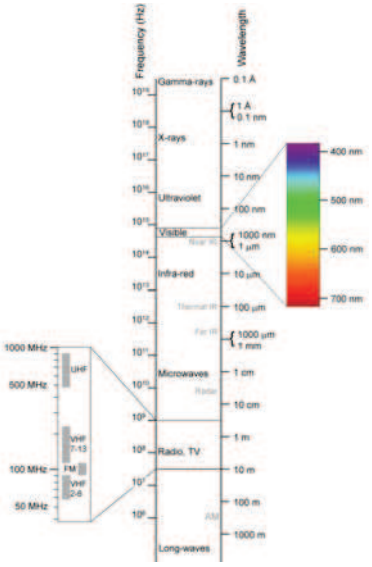

Figure 8 Spectrum of electromagnetic waves. (Source: http://upload.wikimedia.org/wikipedia/commons/8/8a/Electromagnetic-Spectrum.png; 2012-05-30).

X-rays in medicine are used for both, diagnosis and treatment. One of the main applications of x-rays is imaging – besides others such as fluoroscopy and radiation therapy. Typical applications in conventional x-ray or conventional radiology are the detection of pathologies of the skeletal system and disease processes in soft tissue. The basic application of x-rays for imaging is planar 2D imaging – plain x-rays – where x-rays penetrate the body, are attenuated to a certain level and a 2-dimensional projection of the imaged region is acquired. Today, flat panel detectors are widely used to acquire the images instead of older film technologies. Other CT technologies facilitate 3-dimensional imaging which is typically done by rotating the x-ray source and a detector unit around the object. The detector can either be a row of single detector elements with a collimator in front of them to direct only parallel x-ray beams onto the scintillator, or it is a whole two dimensional detector matrix – again a flat panel detector – without the possibility of having a collimator in front. By mathematical operations, the 1D signal obtained by a Multi Slice CT detector row or the 2D projection obtained by a Cone Beam CT is stacked together to a 3D data set or stack. Details about x-ray sources, detectors and CT geometry are explained in the next chapter. 3D computed tomography with c-arms and flat panel detectors is a relatively new imaging technique to acquire *CT-like* images (Siewerdsen and Jaffray 2000).

2.3.2. CT Systems

X-Ray Sources and Detectors for CT

The basic components of any x-ray machine are an x-ray tube, the x-ray generator and a control system. They determine the tube voltage, tube current and irradiation time – the parameters essential for exposure.

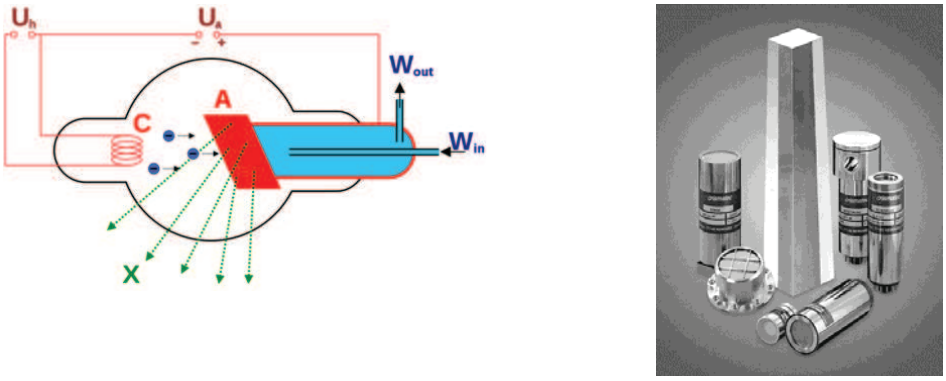

Figure 9A Basic appearance of an x-ray tube. (Wikimedia 2010) B Scintillator.crystal surrounded by detector elements. (Saint-Gobain Crystals 2008)

Figure 9 shows the basic appearance of an x-ray source. X-rays are generated in vacuum tubes that use high voltage to accelerate electrons from the heated cathode and release them onto a target, the anode. The electrons collide on the anode and create x-rays in form of *Bremsstrahlung*. Bremsstrahlung is radiation of a continuous spectrum that is produced when electrons are scattered near the high-Z nuclei. The maximum energy of the produced photon is limited by the energy of the incident electron which is equal to the applied tube voltage (a tube voltage of 100 kV can create x-rays with a maximum energy of 100 keV). In addition, x-ray fluorescence is created when an electron has enough energy to remove an electron out of the inner shell whose place is then filled up by an electron from an outer, higher energy level, emitting x-rays at this time for the conservation of energy. Typical targets are rhenium, tungsten, molybden or even copper – all of them producing a material specific spectrum of x-rays consisting of the continuous bremsstrahlung and several material characteristic spikes.

Angiographic flat panel units operate at lower tube voltages for better contrast visibility of iodide, but in addition, recent studies show a significantly higher dose reduction through lower tube voltage as well. But decrease in tube voltage can lead to higher image noise. High quality imaging with flat panel detector angiographic units – and CBCT can be incorporated in such a unit – is obtained by performing *automatic exposure control* (AEC) which has its equivalent in attenuation based tube current modulation in MSCT (Strobel 2008).

MSCT detectors

Figure 9B shows a *scintillator crystal* and detector elements. When the crystal is hit by an incoming particle it absorbs its energy and reemits light which can be detected by a row of *photomultiplier tubes* or *photodiodes* as it is the case in CT detectors as shown in Figure 10A.

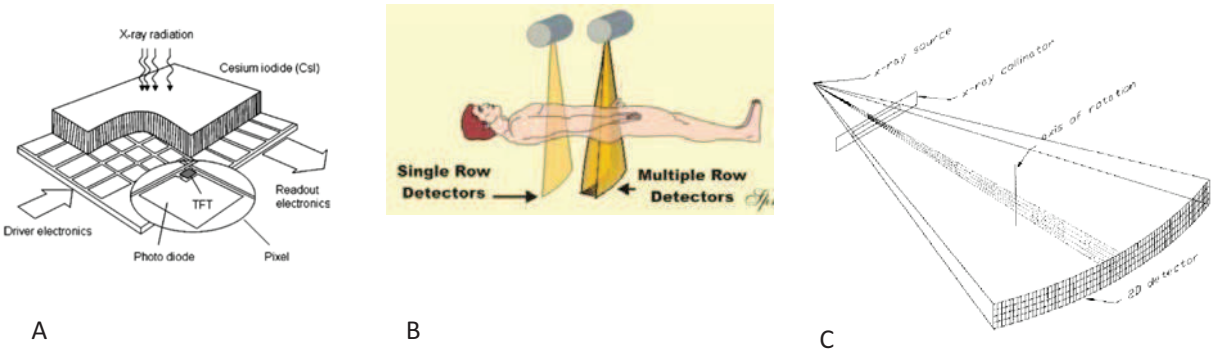

A B C

Figure 10A State of the art CT detector with scintillator and semiconductor. (Strobel 2008) B Single vs. Multi Slice detector matrix. (http://www.ct-scan-info.com/64slicect.html; last accessed 2012_06_18) C One detector element showing the x-ray source, the collimator and the 2D detector matrix. (Hu 1998)

Figure 10B shows the difference between an old single slice detector row compared to a modern multi slice detector matrix. In front of the matrix is the collimator which ensures that only parallel x-ray beams reach the detector crystals.

Flat Panel Detectors

Unlike a detector row as in MSCT, a *flat panel detector* (FPD) contains a whole matrix of detector elements (see Figure 10B).

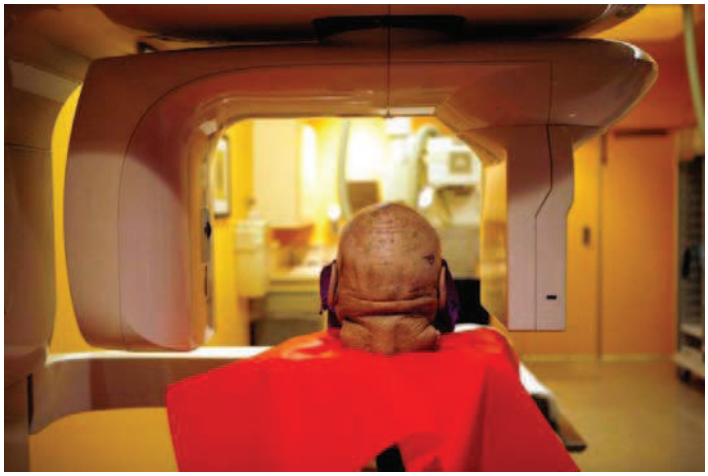

Figure 11 Dental Cone Beam CT Unit with a Flat Panel Detector on the right and the x-ray source on the left. Johns Hopkins Outpatient Radiology Center.

Figure 11 shows a flat panel detector unit as it is installed within a dental cone beam scanner. The x-ray source is on the right opposite the FPD. Figure 11 shows the configuration of the scanner for the scans of the head specimen. A patient stands upright between source and detector. Compared to a MSCT, flat panel CBCT is superior in spatial resolution (Gupta et al. 2004; Gupta et al. 2006), and Flat Panel CT units can be used for angiography (in fact, they are implemented on angiography units) due to the wide field of view and the capability of shooting in video refresh rate. Contrast resolution, on the other hand, is still inferior to MSCT and MSCT in general is faster since it can acquire up to 900 – 1200 projections during a single rotation within 0.5s – the slower cesium iodine scintillator materials used in flat panel detectors limit the acquisition time to 3-20 seconds per volumetric scan (Gupta et al. 2008).

Geometry of CT Systems – MSCT vs. CBCT

The original clinical CT scanner was introduced by Sir Godfrey Hounsfield in 1967. The first gantries translated and rotated around the patient, and data acquisition was based on translate-rotate parallel-beam geometry where beams were directed at a detector opposite the source (Miracle and Mukherji 2009a). The transmitter intensity of photons incident on the detector was measured (Figure 12).

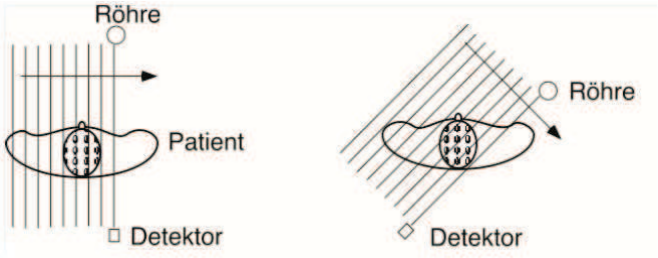

Figure 12 First generation CT system as introduced by Hounsfield.(Dössel 2000)

CT technology changed rapidly, but the general principle is still in use.

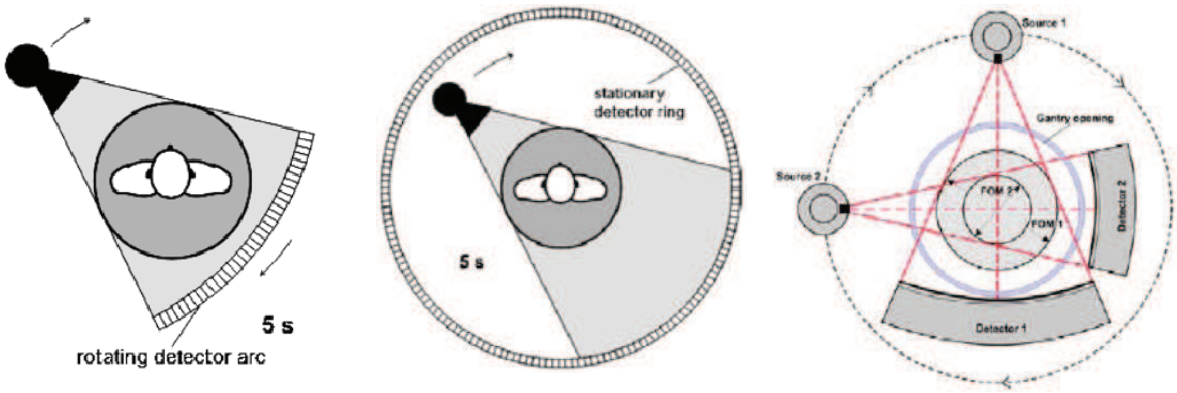

Figure 13 New generation CT technologies. A 3rd generation CT; B 4th generation CT; C Dual source CT. (Kalender 2006)

Figure 13 shows the current technical state-of-the-art conventional Multi-Slice CT techniques and generations, the main difference lies either in the detector geometry or in the source. As it can be seen, current developments in MSCT focus predominantly on faster acquisition rates for real time heart imaging rather than high resolution – and resolution is where CBCTs have their advantages.

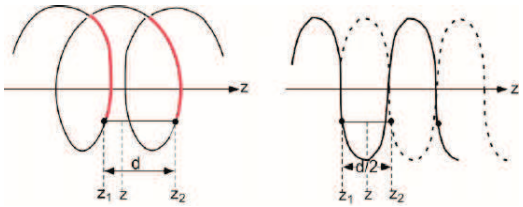

Figure 14 Helical vs. Spiral mode. (Dössel 2000)

Another feature of MSCT systems is the possibility to drive the *gantry* – i.e. the mechanical system carrying source and detector – in *helical/spiral* mode compared to the step mode. *Helical mode* is faster, but the reconstruction algorithms have to take this into account and less spatial resolution is achieved in comparison with *step scan mode*, where the source and detector are rotated in *closed circles* around the patient.

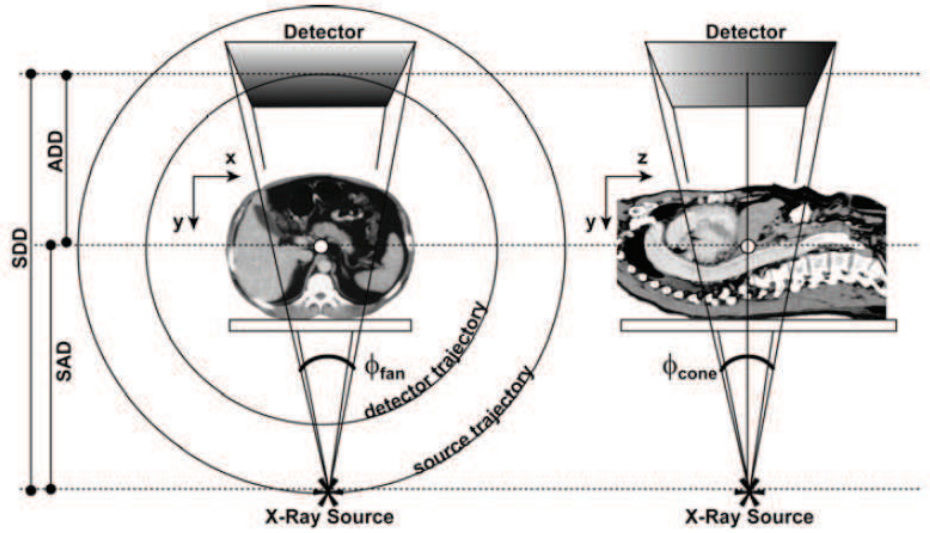

Figure 15 Schematic of a volumetric Cone Beam Computed Tomography. (Siewerdsen 2008)

Figure 15 shows the schematic of a cone beam volume CT. It is similar to MSCT, but the detector is not a row of detector elements with a collimator in front of the scintillator, but a 2D matrix. SDD in the picture is the source-detector distance, SAD the *source to axis distance*, ADD the *object to detector distance* and the *fan angle* Φ_{fan} is the same as on a MSCT and the *cone beam angle* Φ_{cone} defines the longitudinal z coverage. The system geometry is linked to the imaging performance: the magnitude of cone beam artifacts depends on the *z distance* above or below the axial plane. The magnitude of scatter depends on the volume size and on the *object-to-detector distance*. Spatial resolution depends on the magnification (the ratio of ADD to SDD) (Siewerdsen 2008).

2.3.3. Fundamental Principles of CT

The *attenuation* of a monochromatic x-ray beam through a homogeneous object is described by the *Lambert Beer law*:

$$I = I_0 \, e^{-\mu x}$$

with I as the transmitted photon intensity, I_o as the original intensity, μ as linear attenuation coefficient and x as length of the x-ray path through the object. The expression changes for inhomogeneous tissues to

$$I = I_0 \, e^{-\int \mu x dx}$$

Line integrals of the linear attenuation coefficients can be obtained by taking the negative logarithm of this expression, with the line integral at the angle Θ through the object defined as ray sum – a set of which at given Θ constitutes a projection. μ can then be obtained from a large number of projections at varying angles around the object. The basis of this is the theory formulated by Radon in 1917.

Radon Transformation

The Fourier transform of a projection of an object at a given angle yields a slice of the Fourier Transform of the object at the corresponding angle in the Fourier domain.

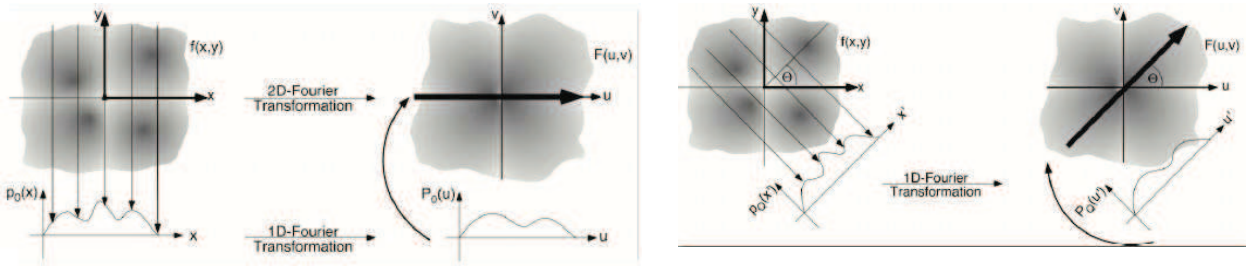

Figure 16 The Radon transformation at any given angle explained. (Dössel 2000)

Basically, the signal obtained by one acquisition is a 1D projection data (Figure 16 left). The projection of an object at any given angle is a set of line integrals which represent the attenuation of the x-ray. Out of multiple such projections and with the help of the 1D Fourier transform, the image space is filled up; and after the inverse 2D Fourier transformation, the whole image can be reconstructed out of the single projections. The mathematical background behind that is the *Fourier slice theorem*. It says that if we have an infinite number of 1D projections of an object, taken at an infinite number of angles, we can reconstruct this *sinogram* of the object through the *inverse Radon transformation*. It starts with *f(x,y)* as a 2D function with the projection *f(x)* onto the x axis in *p(x),* where

$$p(x) = \int_{-\infty}^{\infty} f(x,y)dy.$$

And with the Fourier transform of *f(x,y)* as

$$F(k_x, k_y) = \int_{-\infty}^{\infty}\int_{-\infty}^{\infty} f(x,y)e^{-2\pi i(xk_x+yk_y)}dxdy,$$

the slice is

$$s(k_x) = F(k_x, 0) = \int_{-\infty}^{\infty}\int_{-\infty}^{\infty} f(x,y)e^{-2\pi ixk_x}dxdy = \int_{-\infty}^{\infty} p(x)e^{-2\pi ixk_x}dx$$

which is the Fourier transform of *p(x).*

3D Filtered Back projection and Feldkamp Algorithm for CBCT

The simple idea behind back projection is that if we have a finite number of projections of an object, the projections can be run back through the image domain to obtain an estimation of the original image, which is the unknown volume. For parallel beams, the *back projection* is expressed as the Radon transform which is related to the Fourier transform.

The gold standard algorithm for reconstruction of CBCT projected data is the *Feldkamp algorithm*. It's a generalization of the filtered back projection as described above. The difference is that each voxel in the final image is a weighted sum of cosine-corrected, filtered projection values (Gupta et al. 2008).

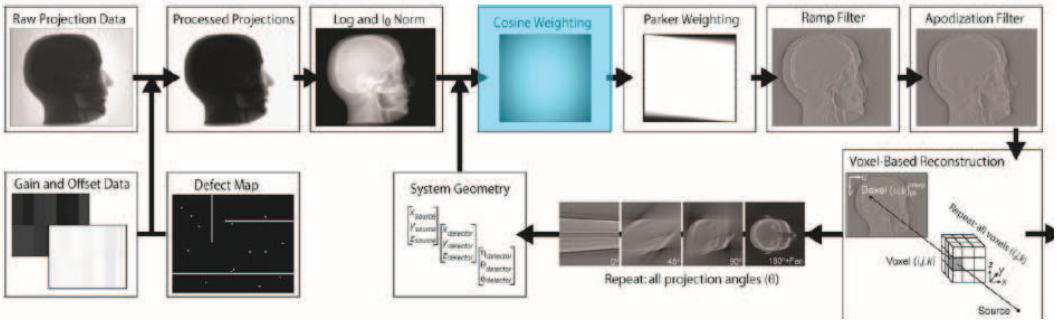

Figure 17 3D Filtered Backprojection. (Siewerdsen 2011)

Figure 17 gives a more advanced view of how the filtered back projection works – basically, various weighting and ramp filters are added before the reconstruction of the projected data is done.

The sense of using a filtered back projection instead of a non-filtered back projection is that due to setting all image pixels along the projection axis to the same value, the resulting image looks blurry. Common filters for filtered back projection are weighting filters like the *Shepp and Logan* or *Ramachandran and Lakshimirayan* filter.

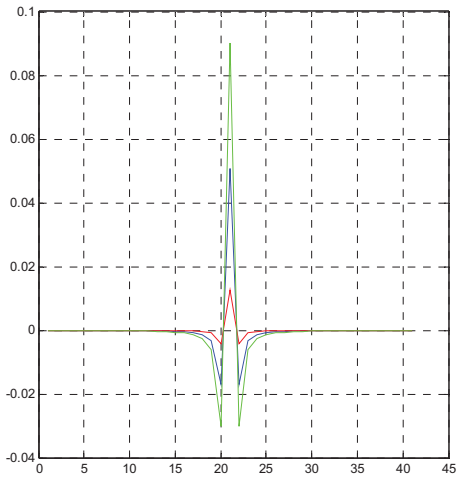

$$h_k = -\frac{1}{\pi^2 a^2}\frac{1}{4k^2 - 1}$$

Figure 18 Example of the Shepp and Logan weighting filter for 3D filtered back projection.

2.3.4. DICOM

The *DICOM* standard stands for *Digital Imaging and Communications in Medicine* and it includes a file format definition that enables the integration and exchange of data from different imaging modalities onto servers, workstations, printers and network databases as the *PACS* system (*Picture Archiving and Communication System*). For CT scanners, the interesting parameters stored together with the image data itself are available via a *dicominfo* file (e.g. accessible over the *dicominfo* command integrated in the Matlab image processing toolbox (MathWorks, Matlab, Natick, MA, USA)).

Such parameters are e.g. *slice thickness* (mm), *tube current* (mA), *tube voltage* (kVp), *reconstruction convolution kernel* (Hounsfield, *Edge Enhancement*, *smooth*, *sharp*, *normal* etc.), protocol name, patient and examiner data etc.

Image Reconstruction

The simplest method is *multi planar reconstruction* (MPR) of the CT data stack. A volume is stacked together out of the single axial slices. Software algorithms cut the slices in three usually orthogonal volumes, but slice planes can be adjusted by the user and oblique slicing is commonly used.

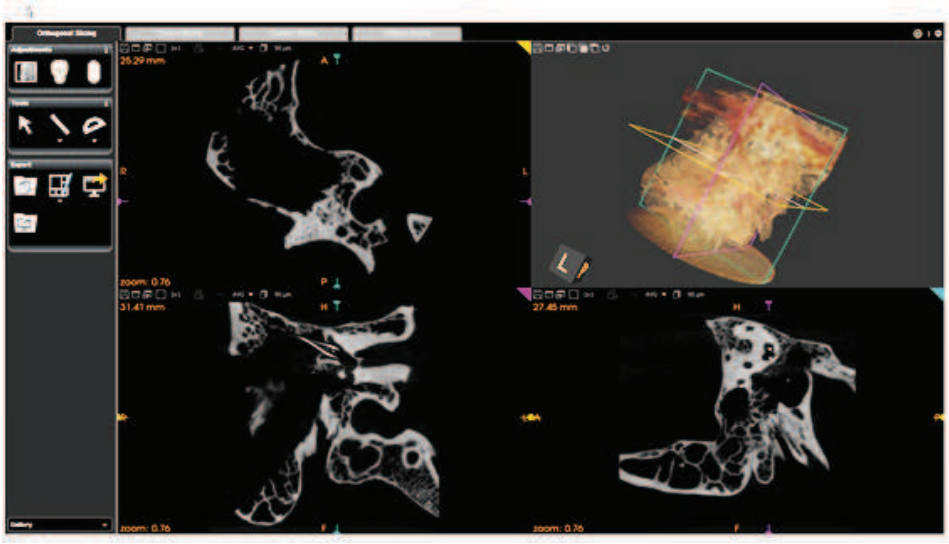

Figure 19 Dicom viewer with a loaded image stack in orthogonal slicing and volume rendering. Kodak/Carestream 3D viewer.(Carestream Health, Rochester, NY, USA).

Figure 19 shows a typical DICOM viewer with a temporal bone CBCT scan loaded. The three slices are orthogonal to each other, but the viewer allows also oblique slicing or curved plane slicing which, for example, is used to visualize bent vessels at once.

Surface and volume rendering algorithms are also often applied within even the simplest viewers. Usually, a threshold radio density value has to be set by the user and then the software constructs a 3D model with edge detection algorithms for *surface rendering*. In *volume rendering* as on Figure 20, transparency and different colors are used to allow a better representation of the entire volume instead of just the surface of the image stack.

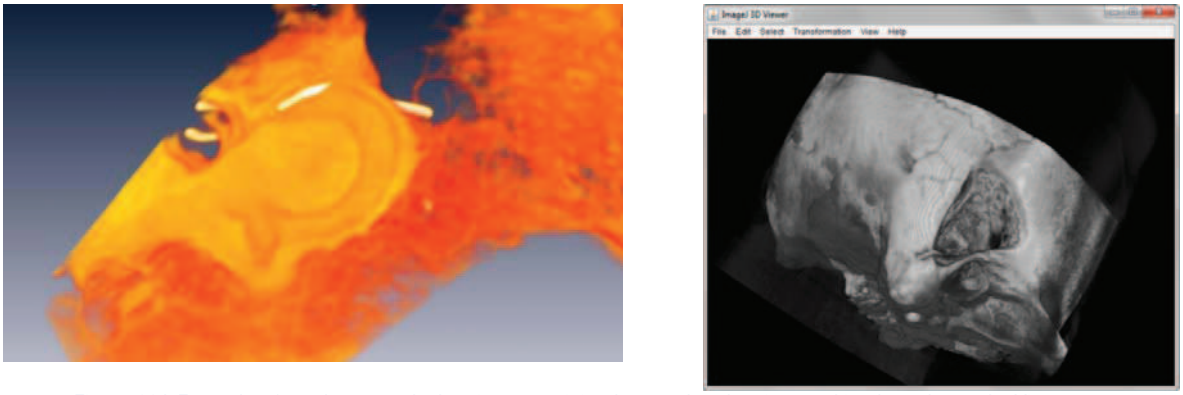

Figure 20A Example of a volume stack showing a semicircular canal and an inserted implant electrode. View generated in Amira. (Amira Visage Imaging, San Diego, CA, USA). B Surface rendering of an image with of a temporal bone specimen with inserted cochlear implant electrode. Image generated in ImageJ (Wayne Rasband, NIH).

2.3.5. Partial Volume Averaging

One of the main artifacts of CT is the *partial volume artifact* or *partial volume averaging*. It occurs when an object lies just partly within a voxel or slice (i.e. if the object is thinner than the slice). The scan shows then an average of the density of object and surrounding material (Figure 21) – dense, small bone pieces can look like soft tissue due to that.

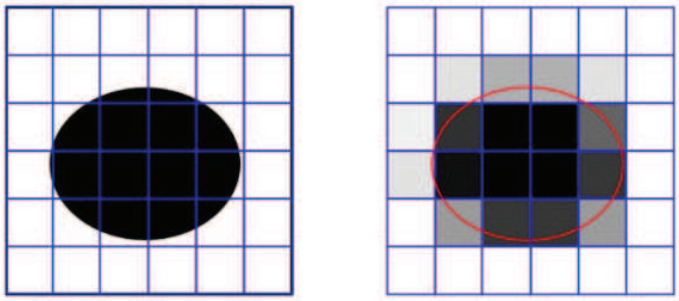

Figure 21 Partial volume averaging of a round structure. The surrounding pixels show an average of the real density values.

2.3.6. Binning, Dose, Scatter and Image Quality

One of the main advantages of CBCT compared to MSCT is a lower overall radiation dose for patients. This is just partly true if CBCT scans are acquired with high resolution 1X1 binning protocols: for a better *signal-to-noise ratio* (SNR), the average dose has to be increased in CBCT.

Binning in CT is a method to reduce noise. In an unbinned image, the signal from each pixel is associated with a certain amount of noise. In a 2 x 2 binning protocol, four pixels form one functional *superpixel*. Four pixels associated with four separate noise events. By combining an array of pixels, the signal is accumulated from four pixels but read noise is reduced to just one read noise event instead four. Although noise reduction is an advantage in binning, it increases the pixel size and decreases spatial resolution.

Dose Units

Absorbed dose – or *total ionizing dose* – is the unit measuring the energy deposited in a certain tissue or mass (it depends on the tissue or absorbing material). It is equal to the energy deposited per unit mass of the medium, measured in *joules/kilograms* and represented as *Gray* (Gy) given by the following equation

$$\overline{D_T} = \frac{\int_T D\ (x,y,z)\rho(x,y,z)dV}{\int_T \rho(x,y,z)dV}$$

and with $\overline{D_T}$ as mass-averaged absorbed dose of the object *T, T* as the object, *D(x,y,z)* as the dose as function of space, ρ as density as function of space and *V* as Volume.

The absorbed dose alone is not a measure for the effect of radiation on human tissue since it does not take the type of radiation, the dose rate or the parameters of the tissue into account. The *equivalent absorbed radiation dose* or *equivalent dose* (which is not the same as the dose equivalent!) is an average measure of radiation absorbed by a certain type of mass or tissue. This is an adequate unit to quantify the health risks or radiation exposure. To get the equivalent dose out of the absorbed dose, the following calculation can be done:

$$H_T = \sum_R W_R * D_{T,R}$$

with H_T as *equivalent dose* absorbed by the tissue *T*, $D_{T,R}$ as the absorbed dose in tissue *T* by radiation type *R* and W_R as a radiation weighting factor[3] which is by regulation defined as for example for x-rays as 1 and for alpha rays as 20. The SI unit for the equivalent dose is *Sievert* (Sv), defined as *Joule/Kilogram*. (Dössel 2000)

The Austrian radiologic society gives limits for the yearly dose of patients and professionals dependent on their area of operation. The dose for a regular patient cannot be more than 50 mSv/a and must not exceed more than 100 mSv over the period of four years (Lechner 2011). Several standard organ or bone programs for plain x-ray or CT have been analyzed and typical radiation exposures are listed in Table 1.

Application	Skin surface dose (mGy)	
	μ	σ
CT Head (120 kV, 100 mAs)	7	
CT Torso (120 kV, 100 mAs)	2	
Catheder heart	410	40 – 1020
Mammography	25	2 – 100
Gastro intestinal	160	10 -1300
Abdomen	12	4 – 150
Thorax	1	0.7 – 2.5

Table 1 Typical dose values for diagnostic x-ray for CT and plain radiography. (Dössel 2000; International Commission of Radiological Protection 2010)

[3] The radiation weighting factor represents the relative biological effectiveness of radiation and corrects the effects of different types of radiation on biological tissue.

The *American Association for Physicists in Medicine* publishes the average dose values as recommendations for each individual scan protocol on a CT scanner – therefore, alert values are recommended that should be set and confirmed by phantom experiments by the resident clinical physicist to guarantee that no patients are hurt (American Association for Physicists in Medicine 2011). X-ray imaging is essentially noninvasive, but risks are evident due to the ionizing effect of x-rays. Usually, these risks are acceptable provided that the diagnosis and visualization of a certain condition gratifies the use.

Application	CTDIvol[4] notification value (mGy)
CT Head (120 kV, 100 mAs)	80
CT Torso (120 kV, 100 mAs)	50
Pediatric Head < 2 years	50
2-5 years	60
Pediatric Torso <2 years	25
2-5 years	10
Brain perfusion	600
Cardiac	150

Table 2 Notification values recommended by the AAPM working group on standardization of CT nomenclature and protocols. (American Association for Physicists in Medicine 2011; International Commission of Radiological Protection 2010)

However, the best result in terms of image quality is not the best in terms of radiation exposure for the patient. In plain x-ray, much detail is lost in the radiographic process because of the superposition of a volumetric structure on a 2D image. A large percentage of radiation detected is due to scatter from the patient and especially this scatter limits the signal-to-noise ratio. The problem was overcome partly with the introduction of Multi Slice CT – with its possibility of collimation and the relatively simple algorithms. *Scatter*, in fact, is a massive limiting problem in Cone Beam CT, where no collimation is possible due to the different detector unit.

CT Dosimetry – MSCT and CBCT

Whereas dose measurements with a simple dosimeter in conventional x-ray are rather simple, CT dosimetry is more advanced since a whole series of exposures is made. In order to calculate dose, the *Computed Tomography Dose Index* (CTDI) has to be calculated. The CTDI was developed in

[4] CTDI (Computed Tomograpy Dose Index) is defined as the average dose in a single axial scan measured with a standardized dosimeter and phantom over 14 slices.

the context of axial CT scans and takes average multiple scan dose profiles and discrete contiguous axial scans into account. The formula is given as

$$CTDI = \frac{fX}{T} L$$

with f as the *exposure-to-dose factor* in mGy/R, X as exposure (R), L as length of the ion chamber and T as slice thickness. Standard cylindrical phantoms that are usually used for dose measurements cannot be used for CBCT dosimetry due to their inappropriate size. For CBCT, a weighted variant of the CTDI, the $CTDI_W$ was recently proposed, which takes the geometry and properties of the cone beam scanner into account. It can be calculated as:

$$D_W = \frac{1}{3} D_{center} + \frac{2}{3} \overline{D_{periphery}}$$

with $\overline{D_{periphery}}$ as the *mean peripheral dose* (Schafer et al. 2012; Miracle and Mukherji 2009a). Currently, CBCT scanners do not incorporate exact comparable dose measurements within their DICOM protocols.

Effects of Radiation and ALARA principle

There are two categories of biological effects observed on irradiated persons: *Deterministic effects* are observed after exposure to a large dose of radiation and are a consequence of radiation induced cellular death where a great amount of cells have been killed by radiation and the loss cannot be compensated by cellular proliferation. Inflammatory processes follow together with secondary systemic phenomena as fever or dehydration. Patients suffering from deterministic effects may have necrotic changes in skin, fibrotic changes in inner organs, acute radiation sickness, cataract or sterility. Doses required to produce deterministic changes are in excess of 1-2 Gy, but radiotherapy can already lead to such effects. Deterministic effects have a practical threshold dose below which the effect is not evident.

In contrast, *stochastic effects* are those that might lead to malignant neoplasms and hereditary mutations. The reasons for stochastic effects are that irradiated but surviving cells may become modified by induced mutations. Below 100 = 200 mGy, potential effects cannot be measured anymore and there is always the risk of spontaneous mutations not related to radiation which cannot be differentiated qualitatively from actual radiation injuries. The approximate risk of radiation induced cancer is roughly at 5% increase after a whole body dose of 1 Sv, but no statistically significant effects have been measured below 0.05 Sv (International Commission of Radiological Protection 2010). In comparison: On a transatlantic flight from Frankfurt to New York, the resulting dose is around 0.1 mSv (Lechner 2011). CT scans of abdomen or pelvis utilize about 10 mSv, but care should be taken for multiple CT scans and they should be justified – which is stated through the *ALARA/ALARP* principle. ALARA stands for As Low As Reasonably

Achievable and ALARP for As Low As Reasonably Practicable – a term introduced by the UK Health and Safety law and generally used to state that the residual risk has to be as low as possible so far as it is reasonably practicable.

Scatter

Increased x-ray scatter is one of the main disadvantages of CBCT compared to MSCT, limiting the image quality. *Scatter* is defined as off-axis low-energy radiation generated in the patient during image acquisition. It is the contribution of photon fluence (or flux) at the detector not coming from the incident primary beam. *Collimation* eliminates scatter in MSCT, but due to the geometry of CBCT systems, collimation is not possible. Scatter is represented as *scatter-to-primary ratio* (SPR) and can be as high as 3 in CBCT compared to less than 0.2 in MSCT (Peltonen et al. 2007). Increased scatter also increases patient dose and reduces image contrast resolution and it can produce streak and cupping artifacts. Scatter can be reduced by imaging geometry (maximizing the air gap) (Siewerdsen and Jaffray 2000) or by modifying the x-ray beam profile (Miracle and Mukherji 2009a). Minimizing the field of view is another possibility of reducing scatter, but since the geometry of CBCT scanners is usually a given fact, software algorithms for scatter detection and minimization are the matter of choice (Siewerdsen et al. 2006; Gupta et al. 2006). One of the first algorithms was the so-called *Monte Carlo simulation* which predicts scatter on the basis of voxel density models of the entire acquired volume and then subtracts the estimated scatter before reconstruction (current metal artifact reduction algorithms work just the same way). *Antiscatter grids* have been tested but have not been proved to be optimal for every kind of imaging need – especially not for certain geometries of the objects were a large air gap is the case – and in addition, dose is again increased (Schafer et al. 2012). Another method of scatter reduction is filtration of the source and compensating filtration with *copper bow tie* or *wedge* filters that modulate the beam profile by increasing photon intensity at the center of the cone and reducing it at the periphery.

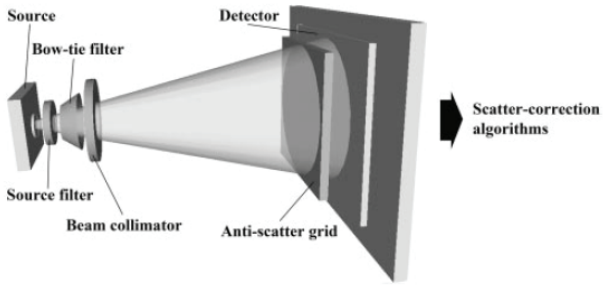

Figure 22 Methods for scatter reduction: source filtration, compensating filtration (bow tie filter), beam collimation, antiscatter grids and scatter subtraction preprocessing algorithms. (Miracle and Mukherji 2009a)

Figure 22 shows a CBCT unit with optimal scatter correction, although in reality, just a few of these methods are implemented (if they are implemented at all).

Contrast, Noise, Resolution and Binning – Factors of Image Quality

The CT pixel values have units of the attenuation coefficient μ, (mm^{-1}), commonly converted to *Hounsfield Units* (HU) through the equation

$$HU' = 1000 * \frac{\mu' - \mu_{water}}{\mu_{water}} * (+1000)$$

μ' is the density of tissue and the HU scale is used to determine the grayscale representations of tissue. Water has therefore an attenuation of 0 HU while air has -1000 HU, bone typically around 400 HU and metal implants 1000 HU and more. To calculate HU out of CT pixel data values, a linear transformation with rescale slope and rescale intercept tagged parameters from the DICOM file have to be done, the simple operation can be implemented e.g. in Matlab by calculating `HU = PixelValue*Slope+Intercept`.

The result of a 3D acquisition is a 3D volume of data sampled on a discrete 3D grid with elements called *voxels* which contain the signal intensity.

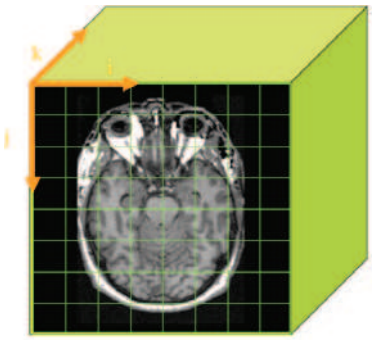

Figure 23 Representation of a 3D volume acquisition in a discrete dataset of voxel. (Pujol 2012)

Image noise as shown in Figure 24 is referred to as standard deviation in voxel values in an otherwise uniform region of interest. It is dependent on the dose product, detector efficiency, voxel size and on filtering and secondary reconstruction techniques.

Secondary reconstruction in this case means that the CT image is reconstructed from the original, raw and unprojected signal stack once more. To perform a secondary CT reconstruction, the region of interest can be chosen by using the sinogram image which is usually shown in real time during a CT acquisition. By reducing the volume of the *region of interest* (ROI), the resulting voxel size after the secondary reconstruction is also reduced which results in better spatial resolution.

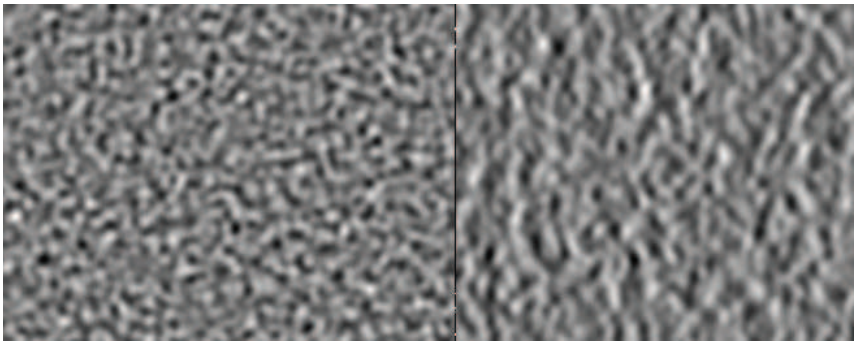

Figure 24 General appearance of Image Noise. (Siewerdsen 2011)

To evaluate noise, the *Noise-Power-Spectrum* as a function of the longitudinal and axial domains can be calculated and filtered with a band-pass. Talking about noise in CT data, *NEQ* and *DQE* are two other terms: NEQ refers to the effective number of quanta used at each spatial frequency (*Efficiency * Flux*). DQE (*Detector Quantum Efficiency*) is a metric for characterizing the overall efficiency of a detector and it describes the fraction of quanta used at each frequency, or the square of the input SNR divided by the square of the output SNR which is slightly different than the NEQ.

Temporal resolution means the ability of an imaging system to discriminate sequentially acquired projection data separated by small time intervals (Miracle and Mukherji 2009a). The higher the temporal resolution, the higher is the rate of projected datasets over a fixed gantry rotation interval. Compared to MSCT, CBCT have limited temporal resolution compared to the ceramic detector elements in the detector rows. This might lead to another problem of CBCT: image ghosting and after-glow, with memory effects and streak artifacts in addition.

Spatial Resolution or spatial frequency on the other side is one of the big advantages of CBCT and is referred to as the ability to discriminate between two objects of different attenuation at small distances. It is measured in line pairs/cm and the *modulation transfer function* (MTF) relates the percentage of contrast to the spatial frequency of the inserts in a CT phantom. Spatial frequency is the product of the Fourier transform of functions describing blur, unsharpness, contrast response and the ability to distinguish line pairs, the limiting factor is usually image blurring.

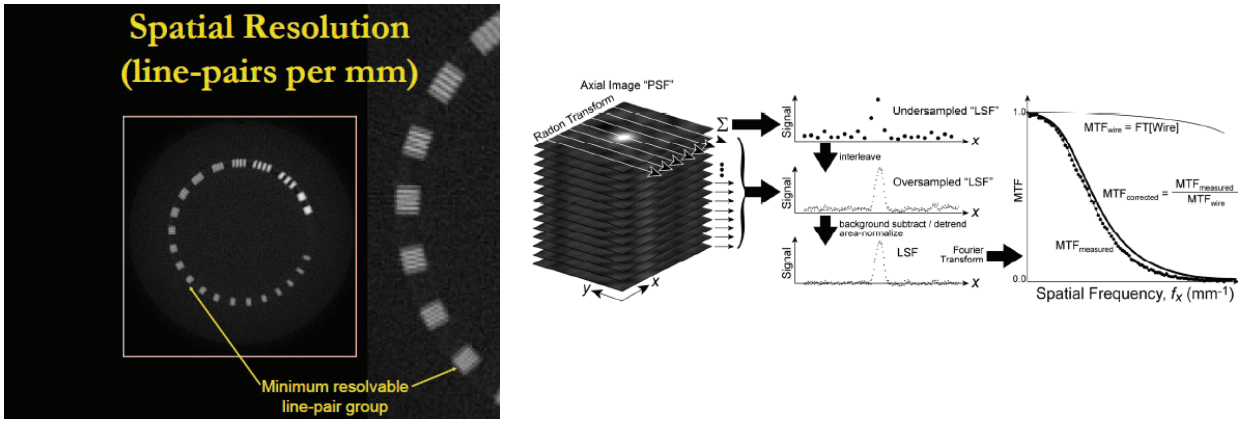

Figure 25 Illustration of spatial resolution in a phantom with different line pairs and visualization of the MTF (Siewerdsen 2011)

Figure 25 shows an illustration of a spatial resolution phantom and of the MTF. Other factors affecting spatial resolution are typically focal spot size, system geometry (and magnification due to the geometry), the detector configuration and several reconstruction parameters like interpolation algorithms or voxel size limitations in secondary reconstructions (Siewerdsen 2011; Miracle and Mukherji 2009a).

Binning means the grouping of detector elements together for the transmission of one uniform signal. The highest spatial resolution is achieved by *1x1 binning*, but the SNR is decreased significantly at constant dose. Usually, scanners provide a 2x2 or 3x3 binning which improves the SNR. A detector is built out of a matrix of sensors – pixels. by combining adjacent pixels one *superpixel* is created. Binning reduces the read noise which is an intrinsically random and unavoidable type of noise every time the chip is read and the image information is transferred. The noise becomes less random when the information of multiple sources is combined – as in the 2x2 binning, 4 pixels are combined, or in the 3x3 binning 9 pixels. By making a larger pixel the SNR is made larger, too – the sensor acts as if it was more sensitive to light, but at the price of less resolution.

2.3.7. A note on Micro CT (µCT)

In its architecture, µCT can be compared to conventional CT units – it's just smaller. It consists of a specimen support and an image detector; some scanners rotate the specimen in a fixed x-ray beam, some rotate the gantry. µCTs are usually used for small animal imaging and for general in vivo and ex vivo imaging. From the standpoint of scanning technique, various methods are employed for the magnification of the primary detected image including also a cone beam approach using direct projections. The *field of view* (FOV) is around 3 – 13 cm and the isotropic voxel size lies around 0.136 mm with a slice thickness of 1 mm. µCT are considered the high

resolution CT standard compared to conventional CT and CBCT. Applications of μCT are assessment of bone architecture and mineralization, visualization of structural heart valve failures or endodontology (Robinson et al. 2005).

3. Material and Methods

Multi slice computed tomography can overestimate the size of a semicircular canal dehiscence, but diagnosis of the SCD syndrome depends mostly on CT imaging. Current developments on the imaging sector bring up Cone Beam CTs as an alternative to MSCT. They deliver a higher spatial resolution and studies show that the radiation exposure for patients is minimized. This makes CBCT the favorite candidate for inner ear imaging. Our aim was to show the current status of high resolution inner ear imaging of CBCT compared to the clinical standard MSCT. Recent studies have evaluated cadaveric temporal bone scans by asking experts for a qualitative assessment of the image quality – and they have confirmed a better definition of fine bone structures (Gupta et al. 2004). Another, even more recent study showed that image quality can be compared with simple image post processing algorithms without the need of having experts define the image quality on a subjective scale (Penninger et al. 2011; Tavassolie et al. 2012).

To drive the post processing further, we evaluated the influence of several secondary reconstruction kernels and of *off-line* filtering of the DICOM image on the accuracy of the scans. We also evaluated if the risk of a false-positive SCD case (detecting a dehiscence where there is still a thin layer of bone) can be eliminated to a certain degree. The goal was to come to a recommendation of standards for scan parameters of dehiscence or inner ear imaging.

This chapter deals with our methods, focusing on the specimens and phantoms used for our study and on the different CT scanners were we acquired our images. In addition, the process of preparing our specimen is described and the software and algorithms we used is mentioned.

3.1. Specimens and Phantoms

To evaluate the accuracy of CBCT versus MSCT, we made phantoms out of bone substitute and prepared a cadaveric whole head specimen with fixed tissue and created an artificial superior canal dehiscence on one side and four cadaveric temporal bone specimens with again fixed tissue which we opened via mastoid approach and where we inserted cochlear implants.

3.1.1. Bone Cement Phantom

The bone cement phantoms consist of injectable HA (*hydroxylapatite*) bone substitute as it is used for SCDS procedures (Hydro Set injectable HA bone substitute, Stryker, Kalamazoo, MI, USA). We filled the liquid bone cement paste into 105 x 70 x 7 mm thick silicone rubber molds (Figure 26) as used for sample preparation for electron microscopy (Pelco embedding molds, Ted Pella

Inc., Redding, CA, USA) and inserted surgical suture of various thicknesses (Plain Gut absorbable suture, Covidien, Mansfield, MA, USA). This sterile surgical suture has a protein base, and is composed of purified connective tissue derived from the serosal layer of bovine intestines originally packed in isopropanol, water and triethanolamine.

Figure 26 Preparation of bone cement phantoms. A: Silicone mold with surgical absorbable suture. B: Mold filled with bone cement.

It is therefore ideal to evaluate the capability of CT to distinguish between bony and tissue structure. We used the suture sizes 3-0, 4-0, 5-0, 6-0 and 0 which corresponds to metric 0.3, 0.2, 0.15, 0.1 and 0.4 mm, respectively. The best estimated resolution of CBCT should be around 90 µm (0.09 mm), and 0.1 should still be visible and able to be resolved with a CBCT scan. Figure 28 shows a volume rendering of a high resolution CBCT scan of four bone cement pieces.

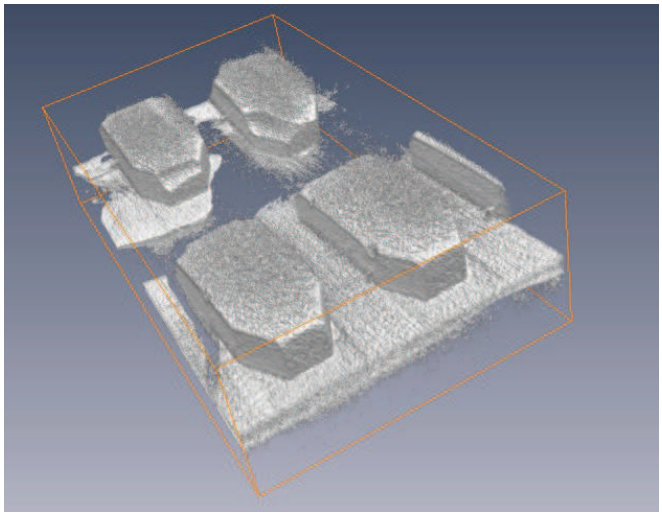

Figure 27 Volume rendering of the Siemens high resolution Dyna CT scan of the bone cement phantoms.

As another measure, we drilled holes into the bone cement pieces in the sizes 0.3, 0.4, 0.5 and 0.9 mm, but due to the good resolution of the scanners, the comparison of the smaller holes containing suture could be used.

3.1.2. Whole Head Specimen with Artificial Dehiscence

Thin bone might appear open over a semicircular canal. To mimic this situation we used a thawed whole male head specimen with fixed tissue and scanned both ears with various settings (Figure 28). The head specimen was obtained from the Anatomy Board of Maryland (Baltimore, MD, USA) and used in accordance with the ethics committee and under Institutional Review Board (IRB) approval.

Figure 28 Whole head specimen in a dental cone beam scanner at the Johns Hopkins Outpatient Center.

We made a surgical *middle fossa craniotomy* and thinned the bone overlying the superior semicircular canal so that it looked almost translucent (Figure 29). The cavity was filled with bone cement as it is done in an SCD procedure and put the piece of cut bone and the tissue back onto the skull, fixing it with suture. Then we re-scanned the head with different CT settings on CBCT and MSCT. After the final scans, we dissected the head and removed both labyrinths of the inner ears, cut them to approximately 5 x 5 x 5 cm cubes and scanned them with a μCT which is the gold standard for high resolution scans.

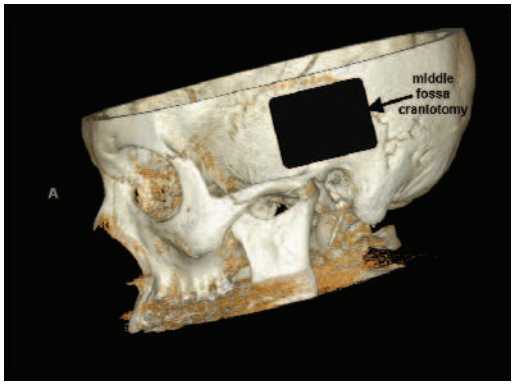

Figure 29A: Middle fossa craniotomy of the head specimen to thin the bone overlying the superior semicircular canal. Craniotomy performed by advisor and author of the thesis. B: Site of the middle fossa craniotomy (Lee 2011).

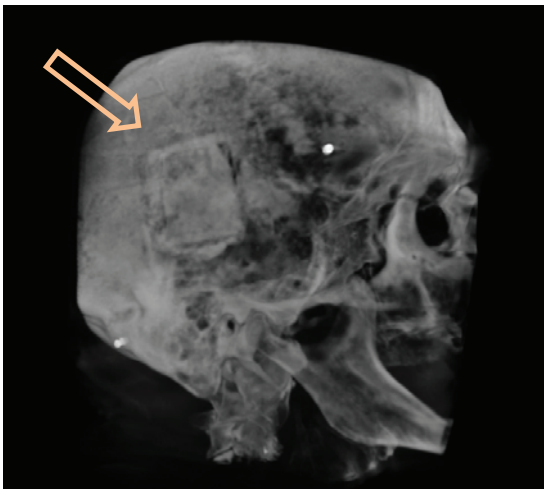

Figure 30 Middle fossa approach on our specimen. Image reconstructed with AMIRA, scanned with the Siemens Artis Zee Dyna CT.

The whole head specimen also allows for correct dose calculations, since all other studies so far used only temporal bone specimen where the radiation exposure of the different imaging settings cannot be generalized to real patient scans and are of no value in terms of dose prediction.

3.1.3. Temporal Bone Specimen with CI

We prepared four cadaveric temporal bone specimens that were also obtained from the Anatomy Board of Maryland (Baltimore, MD, USA) and used in accordance with the ethics committee and under IRB approval. The fixed temporal bone specimens (Figure 31A) were thawed and soft tissue is removed and the bone is cleaned using periosteal elevators.

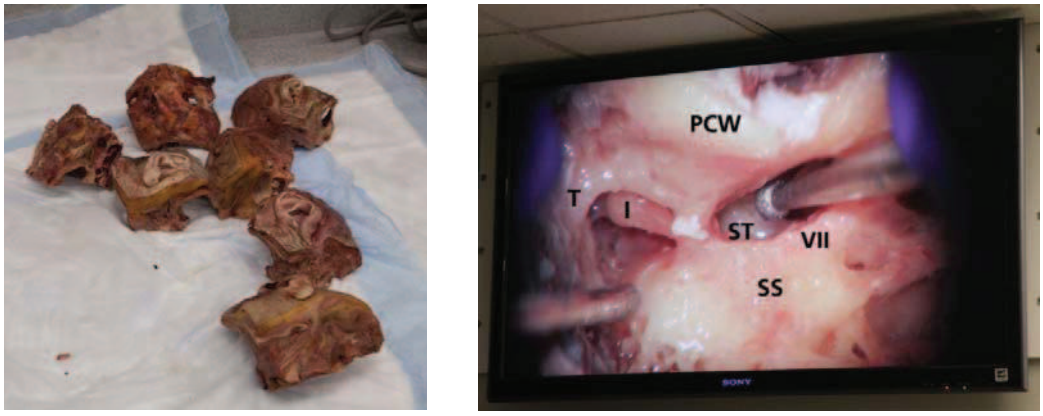

Figure 31A Fixed temporal bone specimens. Facial recess. PCW: posterior bony canal wall; T tegmen; SS Sigmoid Sinus; I incus; VII facial nerve; ST stapes

Then a *mastoid approach* was used to open up the middle ear structure. Cutting diamond burrs from 0.6 to 0.1 mm were used to cut along the temporal line and down towards the mastoid tip, opening a triangularly shaped region. The air cells are removed and after the *mastoidectomy* a *facial recess approach* is continued to enter the tympanic cavity and open the cochlea for inserting a CI electrode as shown in Figure 32.

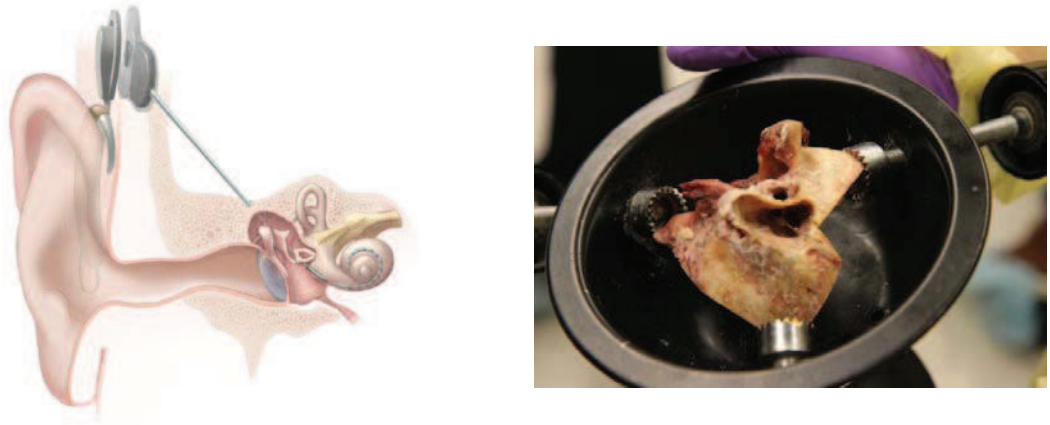

Figure 32A Cochlear Implant schematic. (2005) B: Dissected temporal bone with CI electrode.

3.2. Apparatus

This chapter describes the imaging devices use for our study. Since we wanted to compare MSCT with CBCT, we scanned our specimen and phantoms with a clinical standard MSCT first. Then we used a standard CBCT and another CBCT unit with the possibility to reconstruct images with a secondary reconstruction for high spatial resolution. We used

- a newly developed Carestream Kodak dental unit Cone Beam CT (CS 9300)
- a Siemens high-resolution C-arm CT angiography unit (HR-Dyna CT)
- a regular Siemens C-arm CT (Dyna CT)
- a clinical MSCT from Toshiba (Aquilion) and a Micro CT
- a Micro CT for small animal imaging.

After describing the machines, the experimental setup is explained and scanning parameters and modes are described.

3.2.1. Imaging Devices

Carestream CS 9300 CBCT

Images were acquired with the Carestream CS 9300 Point-of-Care 3D CT (Carestream Health, Rochester, NY, USA). It is a CT scanner for dento-maxillo-facial and ENT scans designed especially for sinus and temporal bone applications. The system includes an x-ray tube, a flat panel x-ray detector, a patient positioning system, a gantry for source-detector rotation about the patient by 180 degrees (for our programs) and a computer system for the control of the imaging system and the reconstruction of the 3D images. For the imaging of the inner ear structures, the left and right unilateral ear protocols were used, with manual instead of automatic setting of mA and kVp for the 20 second scan protocol. Scan settings varied between 3.2 – 15 mA tube current and 60 – 90 kVp tube voltage, which resulted in a dose between roughly 550 mGy/cm^2 – 1500 mGy/cm^2. Scan resolution was set to the highest accuracy, which had a voxel size of 90 µm (and 0.09 mm slice thickness) for the 5x5 scan program – the program with the smallest FOV and the highest resolution. Scan mode was set to pulsed mode. Comparable effective dose measurements have currently been published by (Ludlow 2011).

For image reconstruction, the Feldkamp algorithm for cone beam CT was used with a *normal* Hounsfield filter kernel. Image resolution is 553 x 553 pixel, 16 bit color depth. The scanner uses no beam hardening filters or antiscatter grids. Reconstruction is done directly after the image acquisition with no possibility of adjusting the reconstruction parameters or filter kernels. Image analysis can be done on multiple modalities, included in the system is the Kodak/Carestream 3D DICOM viewer (Figure 33).

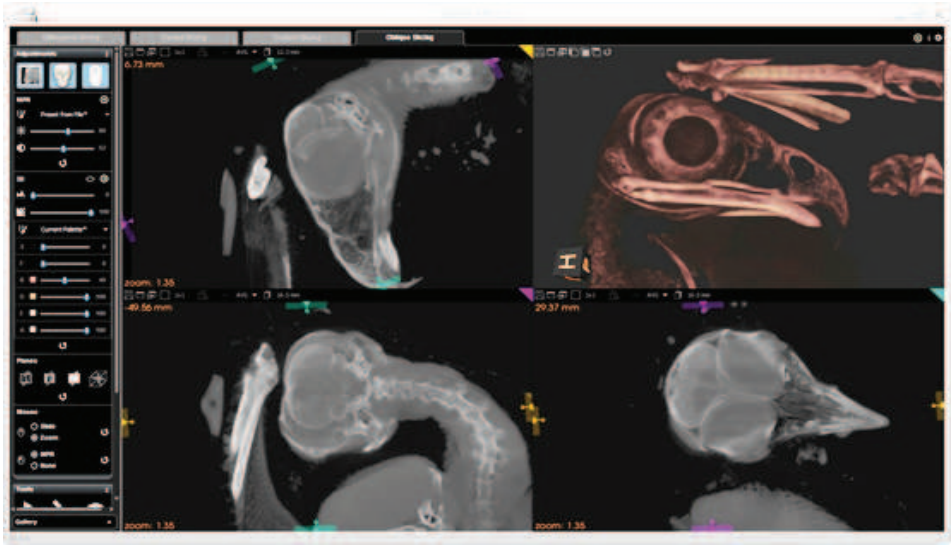

Figure 33 Example of the Kodak/Carestream 3D DICOM viewer for CBCT images. Example shows the scan of a hawk. Scan aquired by the author at the Johns Hopkins Outpatient Center.

Siemens HR-Dyna C-Arm CT with 1x1 Binning

The Siemens Axiom Artis Zee C-arm syngo HR-Dyna CT with 1x1 binning protocol (Siemens Medical, Erlangen, Germany) is a C-arm type cone beam CT which is not yet approved for use on humans (only the regular Dyna CT with 2x2 binning is approved). The 1x1 binning allows higher resolution after a secondary reconstruction step which has to be performed on the Siemens Leonardo (Siemens Medical, Erlangen, Germany) workstation by the operator.

We used the 1x1 binning high-resolution head protocol, collimated to the smallest possible FOV and acquired images with tube voltages ranging from 50 – 120 kVp and tube currents from 100 – 180 mA. Acquisition time was approximately 30 seconds and collimation was set to 0.5 mm, which was the smallest possible setting. Since the scanner is driven with automated dose control, only either tube current or dose per frame could be set, resulting in an automatically adjusted tube current. This might be fine for patient applications, but limits the possibilities for research since not every desired setting can be realized.

No	kV	mA	Dose µGy/frame	Edge (%)	Cu (mm)
01	70	41	1.2	20	0.0
02	63	180	1.2	20	0.3
03	65	184	1.2	20	0.9
04	72	173	2.4	20	0.9
05	73	172	2.4	50	0.9
06	78	161	3.6	20	0.9

Table 3 Example of a specimen scanning session with different scan parameters.

Dose was altered ranging from 1.2 mGy/frame to 5.4 mGy/frame and for the primary image reconstruction, various settings were tested: edge enhancement was applied (0, 20 and 50%, respectively), and beam hardening was tried by increasing the Copper filter thickness from 0 to 0.3, 0.6 and 0.9 mm (see Table 3 as an example scan protocol for the specimen scan in Figure 34).

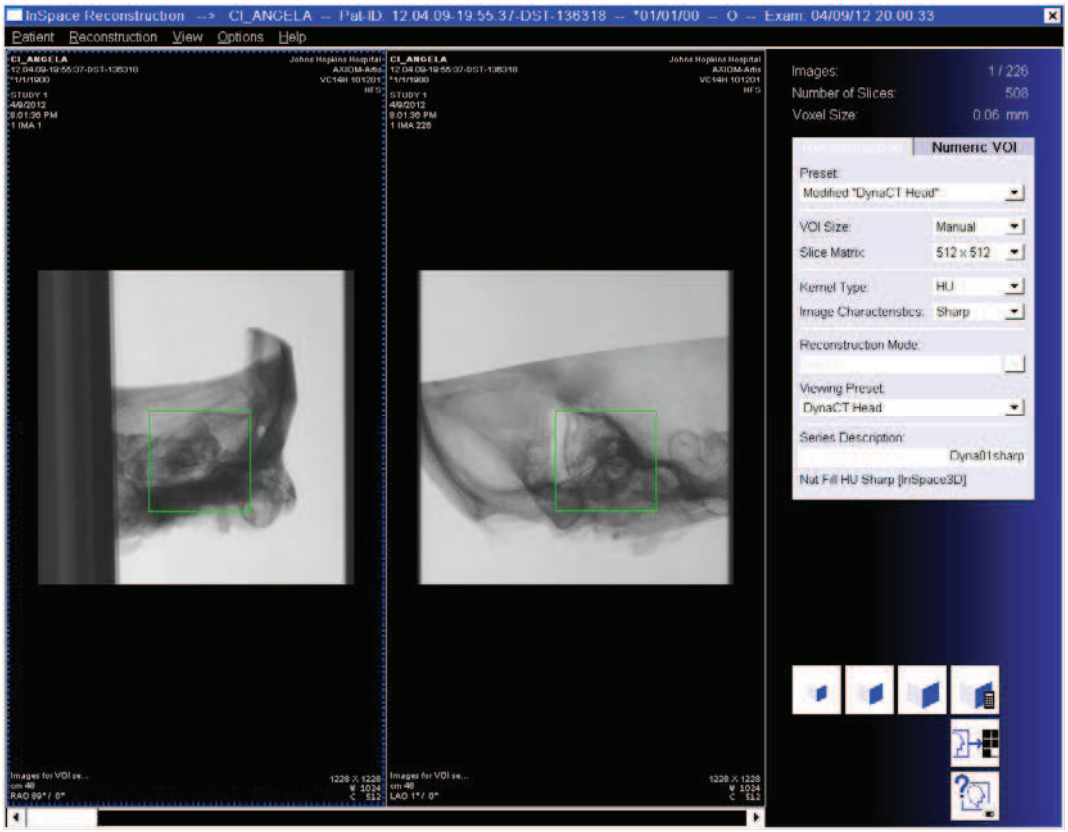

Figure 34 Screenshot of the Leonardo Workstation for secondary image reconstruction. The screenshot shows the original 3D sinogram and the selected ROI for a secondary reconstruction with – in this case – a sharp HU kernel.

As mentioned, to get the full high resolution of the scanner, a secondary reconstruction out of the original, sinogram had to be made on the Leonardo workstation. The ROI had to be reduced again in software, using the z-projection images (Figure 34), resulting in a voxel size of around 0.06 – 0.05 mm as smallest possible option. Different filter kernels were used for the secondary reconstruction: we used both, the Hounsfield and Edge Enhancement kernel with sharp, normal and smooth image characteristics.

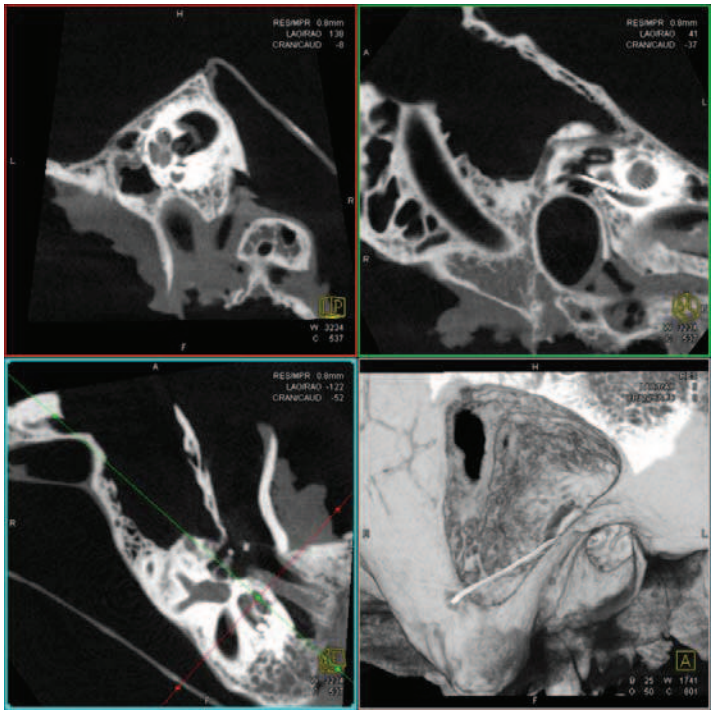

Figure 35 Example data set in Leonardo Workstation - showing a temporal bone specimen in high resolution reconstruction in multi planar view and 3D surface reconstruction.

The resulting image matrix had a resolution of 512 x 512 pixels and bit depth is also 16 bit. The scanner itself can be positioned in any desired position around the patient. X-ray source and flat panel detector are mounted on a mobile C-arm as it is used in most angiography units.

Regular Siemens Dyna CT Angiographic Unit

Everything said about the HR-Dyna CT applies for the regular Dyna CT as well, the only *real* difference lying in the binning which – as described in chapter 2.3.6 – improves the SNR for the cost of less resolution. In terms of CT, another factor has to be considered: the 1x1 binning results in higher patient dose which might be comparable to regular MSCT instead of the low dose known from CBCT machines. The use of HR-CBCT has therefore to be justified.

Toshiba Aquilion MSCT

As a *control* (since still the gold standard for most 3D imaging diagnostic aims) we used a Toshiba Aquilion 64 Multi Slice CT (Toshiba America Medical Systems, Tustin, CA, USA). The scanner has a 64 row detector, images were acquired in non-helical step mode with 2 mm increments in z-direction and no overlap in the scans. The gantry was upright and the specimens were placed in the isocenter. Scan time was 1 second per rotation and a 0.5 mm slice thickness. Although collimated, the scanner uses a Feldkamp reconstruction algorithm to reduce cone beam artifacts on the detector rows. FOV was approximately 18 cm and as protocol the standard protocol for SCD diagnosis – a modified head protocol – was used. After image reconstruction, the data was sent to a Vitrea workstation (Vital Images, Minnetonka, MN, USA) and the DICOM data could be exported externally. The resulting image resolution is 512 x 512 pixels and the reconstruction was done with a *normal* Hounsfield filter kernel. Acquisitions were made with the clinical standard, i.e. a tube voltage ranging from 135 – 120 kVp and a tube current of around 250 mA for a 0.5 second exposure time for each step.

Animal Lab Micro CT

The Micro CT is part of the Johns Hopkins Small Animal Imaging Resource Program (SAIRP)[5] and the scanner is a pre-clinical type CT (Gamma Medica X-SPECT, Northridge, CA, USA) for small animal and specimen studies. We set the scanner to its highest reconstruction resolution of 50 µm voxel size at 1024 x 1024 pixels. Tube voltage was manually set to 75 kVp and tube current to 230 mA. Rotation angle was 360 degrees and to minimize noise, the 2x2 binning protocol was used. The FOV is 150 x 150 mm, specimen should have a size of 50 x 50 mm to stay within the isocenter of the scanner.

Since this is a research scanner, only the raw data is stored and the DICOM files have to be generated first. To do so, the raw files (Figure 36A) can be loaded in AMIRA (Amira Visage, San Diego, CA, USA) (Figure 36B) and converted to readable DICOM files that can be imported into any DICOM viewer or Matlab (Figure 37).

[5] http://www.hopkinsradiology.org/sairp

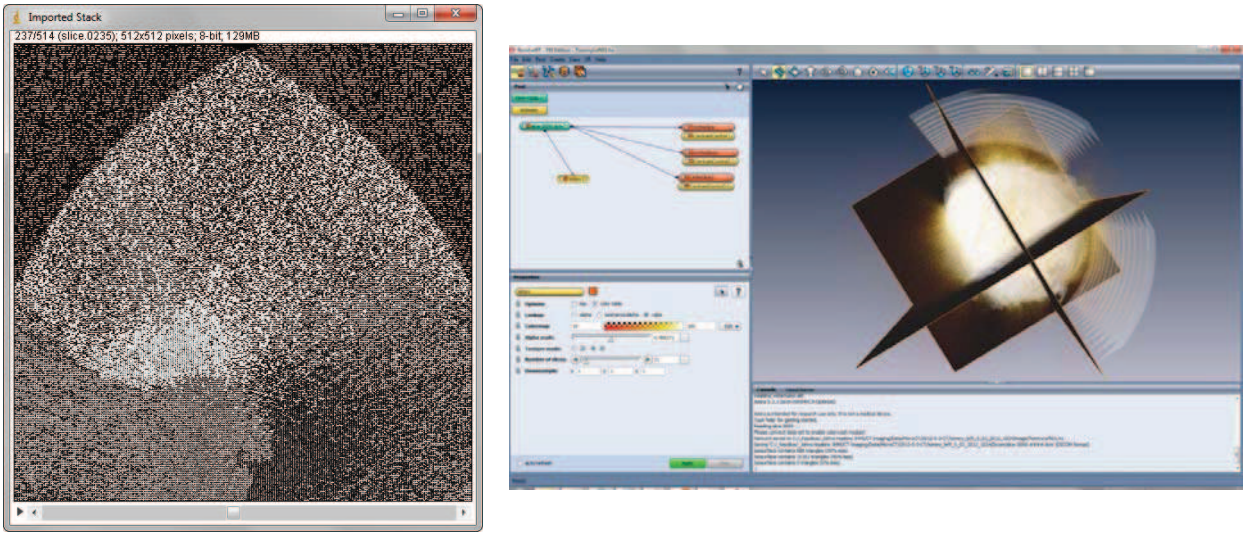

Figure 36A Raw, unprojected micro CT data slice of a vestibular organ in ImageJ. B conversion in DICOM file format via AMIRA.

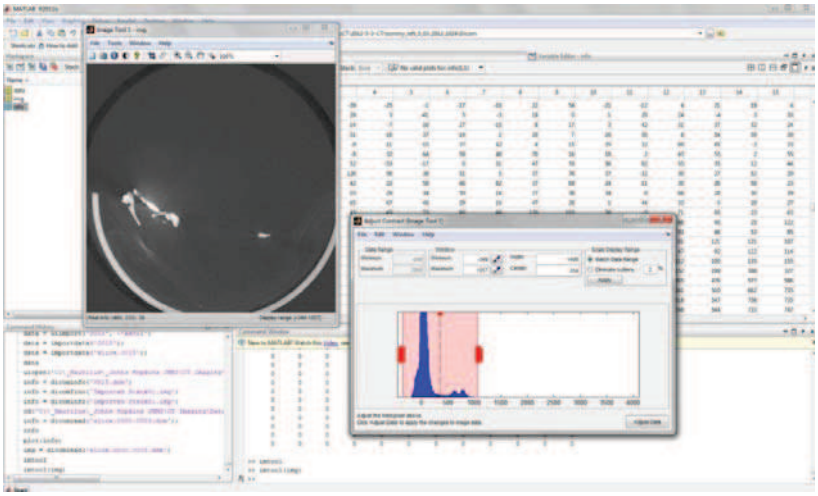

Figure 37 Final DICOM data frame loaded into Matlab.

3.2.2. Workstations and Image Analysis Tools

Having a range of different CT scanners, image analysis is not an easy task. First, the original, unprojected data is reconstructed directly after the scan, but the original data stack was stored wherever possible – various reconstruction parameters can be adjusted in a secondary reconstruction step which will be done on some of the scans after this preliminary study. Also,

exact dose measurements are possible from the head scans that we acquired: Siemens has phantoms to re-calculate the dose when the original data is stored.

Almost all CT machines come with an optimized workstation for data viewing – Leonardo for the Siemens Dyna CT, the Kodak/Carestream 3D viewer for the Carestream CS 9300, Vitrea for the Toshiba Aquilion 64 and AMIRA and Matlab for the Gamma Medica X-SPECT. The goal is, to analyze all data from all modalities within the same vendor-independent environment, which are Matlab (Matlab R2011b, MathWorks, Matlab, Natick, MA, USA), ImageJ and AMIRA. For this thesis, most image analysis was done in Matlab.

Leonardo (Siemens)

We use Leonardo basically to make secondary high-resolution reconstructions with varying filter kernels – smooth, normal, sharp and Hounsfield and Edge Enhancement kernels.

ImageJ (NIH)

ImageJ is a Java based open source imaging software tool designed at the *National Institutes of Health* (NIH). Since it's an open source application, users can contribute with plug-ins and scripts. The basic GUI has already a lot of mathematical operations and filters like edge detection algorithms, fourier analysis, geometric transformations, contrast manipulation etc. included (Figure 38).

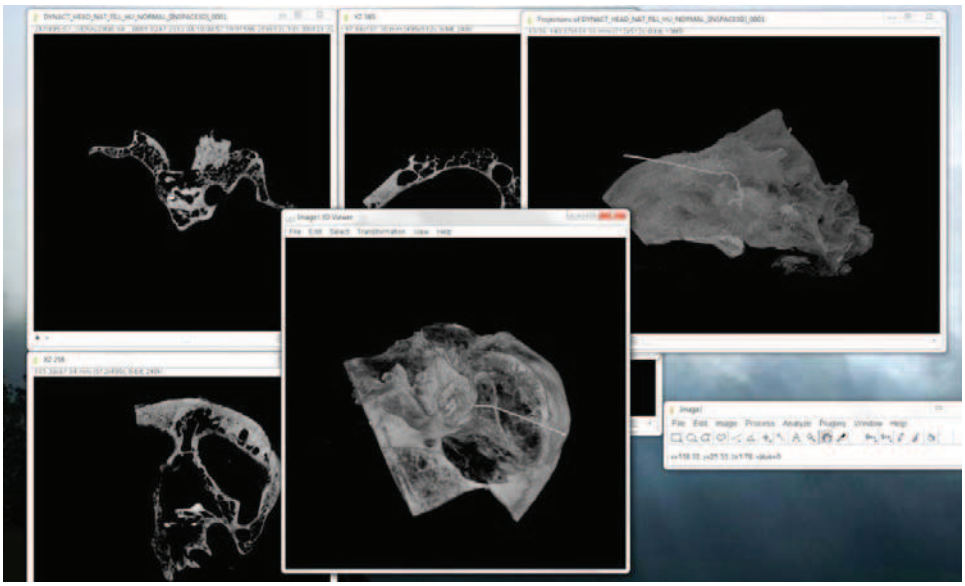

Figure 38 Example of data loaded with ImageJ (showing a temporal bone specimen with an CI electrode array)

AMIRA

AMIRA is a scientific, non-clinical software tool for 3D and 4D data visualization, developed by the Zuse Institute Berlin, Germany. It's not only used for regular CT or MRI data stacks, but can also be used for Micro CT and for data from microscopy, biology, material science, molecular biology, quantum physics, astrophysics, computational fluid dynamics or finite element modeling. The strength lies in image segmentation and geometry reconstruction (see the example in Figure 39) – once a 3D volume is marked, several analysis tools can calculate volumetric, shape or density analysis, respectively and 3D models for simulations or rapid prototyping can be built.

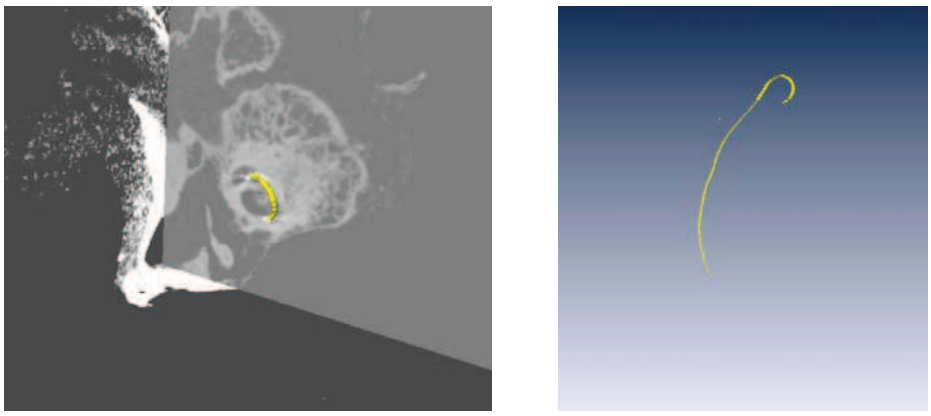

Figure 39 Example of a CI electrode segmentation performed in AMIRA.

3.3. Experimental Setup

The specimens were placed in the same way into the scanner as patients scans would be acquired, with the z-axis of the scanner passing through the plane of the superior canal.

On the MSCT, the gantry was orthogonal to the z-axis (tilt of 0 degrees), on the CBCT, the gantry or C-arm, respectively, rotated 180 degrees around the head/specimens.

To place the head onto the C-arm CT and MSCT patient benchtop, a carton box was filled with beans that used as head holder. Previous scans verified that the bean box did not affect image quality. For the Carestream CBCT, a tripod was used in addition to hold the head and specimen in shoulder height.

Figure 40 Experimental setup on the Carestream CS9300 (left, top), Siemens HR Dyna CT/regular Dyna CT (right, top), Toshiba Aquilion 64 MSCT (Image from http://www.toshiba-medical.eu/en/Our-Product-Range/CT/Systems/Aquilion-64/), Gamma Medica X-SPECT (Image from http://mips.stanford.edu/aboutus/facilities/clark/sci3/instruments.html).

For the Micro CT, the dissected temporal bone pieces were placed in the same way: the z-axis of the scanner being in the plane of the superior canal. The specimens were placed directly onto the holder of the Micro CT.

We made scans with each imaging modality, varying the parameters like tube voltage, dose and/or tube current and – if possible – Copper filter thickness and reconstruction parameters to get the best possible image out of the scanner. On the Multi-Slice CT, we used the clinical standard protocol for SCD diagnosis since we want to compare our new imaging approaches to the gold standard.

3.3.1. Bone Cement Scans

Toshiba Aquilion vs. Siemens regular Dyna CT 1x1 binning

As a first step, we compared Toshiba Aquilion Multi-Slice CT scans with Siemens Dyna CT Cone Beam CT scans with the regular scan protocol, 1x1 binning and with a comparable isotropic voxel size of 186 µm for the MSCT and 198 µm for the CBCT, respectively. The Toshiba scan was acquired at 135 kVp tube voltage, 125 mAs tube current, 0.5 mm slice thickness in 0.5 s pulsed and non-helical mode for highest resolution in z-axis. Reconstruction was done with a *normal* Hounsfield kernel. The resulting DICOM files had a dimension of 512 x 512 px; the protocol used for the scans was an already optimized MSCT protocol used for SCDS diagnosis at Johns Hopkins. The data was exported to PACS on a network workstation and the reconstructed data was stored externally. The Siemens scans on the Artis Zee Angiography scanner were acquired with the high-resolution 1x1 Dyna CT binning protocol, but to compare CBCT with the clinical gold standard MSCT, we first reconstructed the image with approximately the same voxel size as the MSCT scanner. Scans were made at a tube voltage of 50 kVp, a tube current of 114 mA and an exposure of 20 seconds in 4.2 ms pulsed mode. Images were reconstructed with the same *normal* Hounsfield kernel. No Copper pre-filter was used and dose was set to 1.2 mGy/frame. At this scanner, we used the Dyna CT head protocol which is optimized for sinus and temporal bone scans by the manufacturer.

Siemens High Resolution Dyna CT 1x1 binning

The Siemens High Resolution Dyna CT with 1x1 binning gains its highest resolution by performing a secondary reconstruction on the Siemens Leonardo workstation. By reducing the volume on the sinogram of the raw data stack, the voxel size can be minimized as well. For the secondary bone cement reconstructions, we took the same Dyna CT scan as described above and reconstructed the image with a sharp HU filter kernel. This kernel should give highest spatial resolution according to the manufacturer.

3.3.2. Head Specimen Scans

One aim of this thesis is to use the algorithm and approach developed with the bone cement phantoms for a head specimen with an artificial dehiscence. We made several scans with different CTs and varied the scanning parameters – a future project is to use the approach tested within this thesis to compare the different scans as described below. The advantage of having a whole head in this case is that the resulting dose is very close to what can be expected for scans with humans, giving the opportunity to find the best dose for the highest spatial resolution at the lowest patient dose.

Toshiba Aquilion 64 Slice MSCT

We scanned the head with the clinical standard parameters for the diagnosis of semicircular canal dehiscence used at Johns Hopkins. The same settings were used as for the bone cement phantoms, i.e. 135 kVp, 125 mAs, 0.5 mm slice thickness in 0.5 s pulsed and non-helical mode for highest resolution in z-axis. The resulting isotropic voxel size is 186 µm and one DICOM slice has a size of 512 x 512 pixels with 16 bit per pixel. Data was exported to an external hard drive for further analysis.

Siemens High Resolution Dyna CT 1x1 binning CBCT

For our current head specimen analysis, we used a scan from of the Siemens Artis Zee Dyna CT without high-resolution secondary reconstruction but 1x1 binning. Scan parameters for this scan were 89 kVp tube voltage, 140 mA tube current and a 20 second scan time. Edge enhancement was set to the default 20%, dose to 1.2 mGy/frame and the copper filter was set to 0.0 mm. This is the default head program as recommended by the manufacturer. Original FOV was 48 centimeters resulting in a 512 x 512 pixel matrix. Voxel size is 198 µm; for the reconstruction, we used a *normal* HU kernel. Data was stored in the DICOM format in the usual 16 bit format.

This is enough data for this thesis, but for further optimizations of the CT scan protocols, we varied the scan parameters (see Table 1 for an example protocol of a scanning session with different scan parameters). In future, we want to establish the best possible scan protocol for the diagnosis of dehiscence but with emphasis on the ALARA principle to have as less radiation dose as possible for the patient. Within this thesis, we only want to show the principle of the data analysis and processing to evaluate dehiscence. Therefore, no evaluation of high resolution secondary reconstructions were done so far – this will also be part of a future project.

Carestream CS 9300 CBCT

Just as with the Siemens CBCT, we made several scans with a high resolution Carestream dental scanner. Again, we made various different scans of the left and right inner ear of the head (before and after creating the artificial dehiscence) with several scan parameters. As mentioned in chapter 3.2.1, we scanned with tube voltages from 60 – 90 kVp, a tube current ranging from 3.2 – 15 mA, resulting in a dose from 550 – 1500 mGy/cm^2. The Carestream scanner allows no secondary reconstruction, but FOV can be set to 5 x 5 cm prior to the scan, resulting in a voxel size of 90 90 µm (and 0.09 mm slice thickness). The DICOMs have a size of 553 x 553 pixel and 16 bit color depth. No beam hardening filters or antiscatter grids are included on the scanner.

µCT

The µCT is used as a gold standard for high resolution scans. We set the scanner to 75 kVp at 230 mA. FOV was 150 x 150 mm and the images were reconstructed with a 1024 x 1024 image size, resulting in a voxel size of 50 µm.

3.3.3. Temporal Bone Specimen

For the temporal bone specimen, the same scanning parameters as for the head were used and varied. In the case of the data shown in chapter 3.4.3, we scanned the specimen with the Siemens Artis Zee Dyna CT scanner with 1x1 binning. We scanned the dry temporal bone with 70 kVp, 40 mA and the 20 s head protocol as used for the head specimen, too. The copper beam hardening filter was set to 0.0 mm and edge enhancement was set to 20%. We did a secondary reconstruction with a *normal* HU kernel – isotropic voxel size was 198 µm and the size of one DICOM file was 512 x 512 pixel with 16 bit depth.

3.4. Data Analysis

3.4.1. Bone Cement Phantoms

To develop an algorithm for the quantitative analysis of the different scanners, we started with the relatively simple comparison of bone cement phantoms. Different image analysis workstations, different observers in observer studies, computer screens with a wide range of resolutions and luminosities, different windowing presets and similar things contribute to non-systematic, random errors that make the comparison of DICOM files from different modalities imprecise. Our approach is to find mathematical algorithms that make it possible to compare the sizes of the holes in the bone cement phantoms and distinguish them from the noise level of the surrounding solid material with statistically significant certainty.

Processing of Bone Cement Data

To do so, the 3D image stack has to be pre-processed and cut due to the large amount of data. This is done in AMIRA, since the graphical user interface makes handling the data stack easier. Data can be exported as DICOM files from AMIRA. A Matlab function was then written to import the DICOM files of a directory into a 3D matrix structure. Another function allows browsing the 3D matrix and selecting the slices of interest. Just for display, the slices are converted from 16 to 8 bit data to allow the manual selection of the region where the hole is in the phantom, and another region of random noise in the solid material.

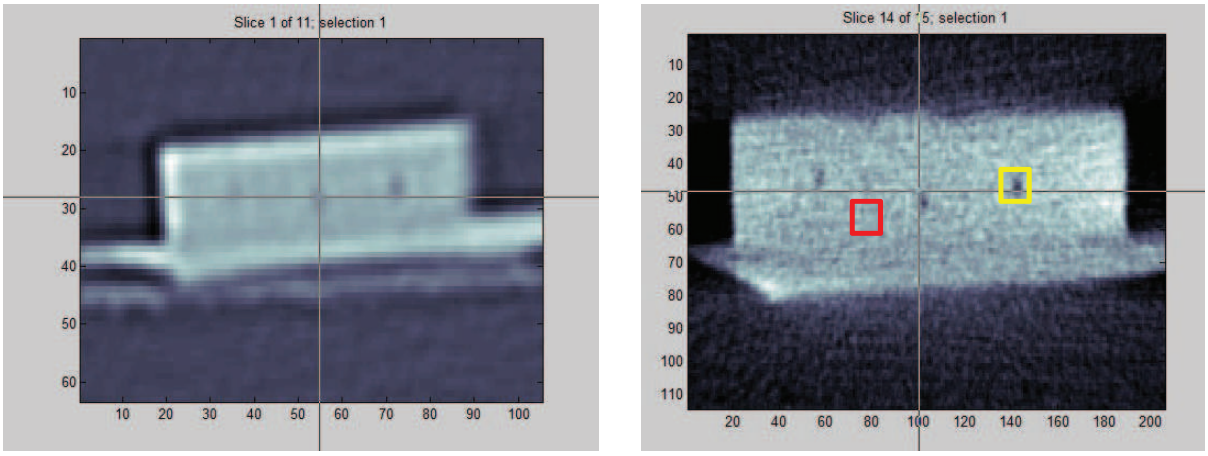

Figure 41 Manual selection of the ROI. A 5 x 5 px matrix is then placed over the selected region. Left: Toshiba Aquilion MSCT; Right: Siemens HR Dyna CT. The yellow (slightly magnified) matrix indicates the selection of a hole. The red matrix contains only image noise.

For this, the hole has to be picked manually and a 5 X 5 pixel matrix (which covers the entire hole) is then cut out of the data – for the high resolution secondary reconstruction, we used a 13 x 13 pixel matrix which has the same diameter of about 200 microns as the matrix from the regular CT scans.

Quantitative Analysis of Bone Cement Data

We calculate the mean HU values, the standard deviation and variance of the 5x5 or 13x13 pixel matrices. Then, we want to estimate the noise level of the solid material by statistical means – to compare standard deviation and means of the data matrix cut off the holes with the data matrix of the solid material. Statistical analysis can be performed with a Wilcoxon signed rank test for two independent samples (statistical analysis was performed using Matlab) – after testing the data for being normally distributed.

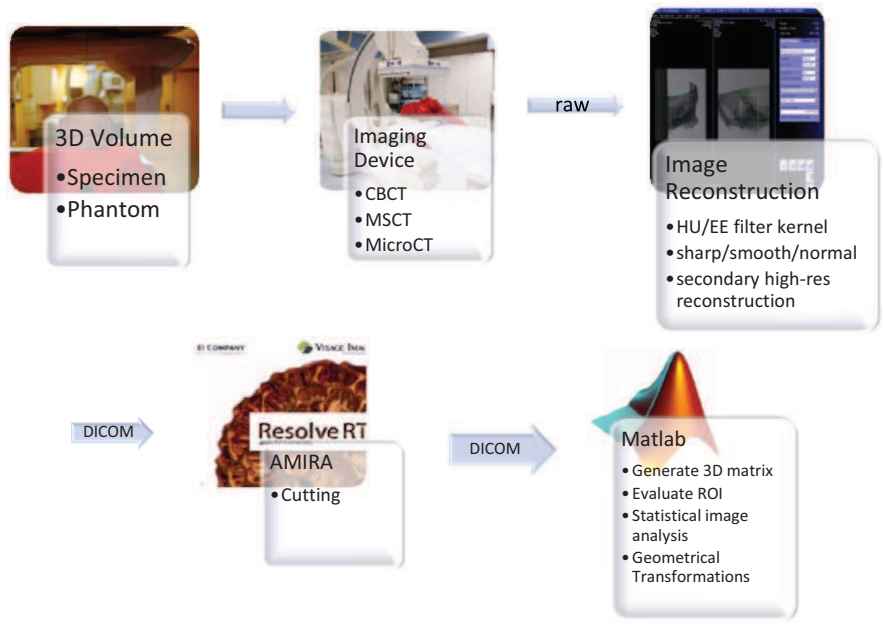

Table 4 Process of data analysis using the DICOM file format standard, AMIRA and Matlab.

Once we know about the statistical parameters of the population, our goal is to predict the probability of detecting a hole – or dehiscence – when taking one slice as a sample and comparing

the variance of this with the noise level. For this, the χ^2-test could be used to test if variances of two populations are equal if the distribution of the data would be normal. But since the data were in our case not distributed normally, we had to use a different approach: we used a modified ANOVA (Brown-Forsythe) and compared a random selection of noise matrices with the ROI matrix. The ANVOA gives us a good estimation by comparing the different standard deviations of the whole data set and tells us if the sample of the ROI contains a hole or just random noise. Another approach is to use the Fligner-Killeen test: a median test for the homogeneity of variances which is most robust against departures from normality.

Brief description of the Matlab Code

The Matlab functions are included in the Appendix of this thesis; image analysis can be done by calling the following functions/scripts:

Function/Script	Brief Description/ Purpose	Call/Input

ReadDicomStack.m	Reads a stack of 3D data from a directory into a 3D matrix and stores the matrix.	`[Data3D, Info] = ReadDicomStack('.dcm');`
		
		`input required - function asks for:`
		`(1) either '.dcm' or '.ima'`
		`(2) a directory with a dicom stack`
		`(3) data in the list other than dicom files will be ignored`

DispDicomStack.m	For an overview and a slice selection, the 3D matrix can be visualized using this function.	`DispDicomStack(MyVolumeMatrix);`
		
		`input required - function asks for:`
		`(1) an image volume matrix with a m x n image matrix in z dimensions`

DicomHist.m	Within the script, the manual selection of the ROIs (holes and solid material) is performed, followed by the calculation of histograms, mean, standard deviation and variance of the data.	`DicomHist;`
		
		`no input required`

DicomStat.m	After having done the analysis, all 3D image matrices and statistics can be combined into a single structure using this function.	`DicomStat;` `no input required`
DicomStatEval.m	After calling DicomStat and storing the whole data set into one structure, statistical analysis and plotting is done herein.	`DicomStatEval;` `no input required`
DicomAnova.m	Perform an analysis of variance and a Fligner-Killeen test between random noise on solid material with any ROI where a hole should be detected.	`DicomAnova;` `no input required`
DicomStatPlot.m	Plotting of results from DicomAnova.m.	`DicomStatPlot` `no input required`

DicomAverage.m	Function that averages over three 3D image slices for noise reduction.	`[ImgAveraged] = DicomAverage(Data3D);`
		`input required - function asks for:`
		`(1) a 3D image matrix in the format n x m x z`

imfilt_test.m	To test various digital filter techniques on CT images of the canals or the bone cement phantoms.	`imfilt_test.m`

Table 5 Matlab workflow for the bone cement data analysis.

3.4.2. Semicircular Canals

The analysis of the canal data is less straight forward than the analysis of the bone cement data – with the main challenge being the *random* orientation of the canal within the 3D data stack; the bone cement phantoms were aligned orthogonal about the planes of the scanner. A good term of the data analysis deals with overcoming this problem. The principle of the statistical, final analysis of the CT intensity values inside and outside of the canal is basically the same as shown with the bone cement phantoms in the previous chapter.

Principle of Canal Analysis – Geometrical Transformations

Figure 42 gives an idea of the transformations that have to be done to get slices along the upper part of the superior canal. To achieve such a projection, a number of calculations have to be done. Thereby we want to generate thin, orthogonal slices of the round canal with the overlying bone. In each slice we can then measure if the bone overlying the canal is dehiscent, very thin or intact.

The basis of the 3D data analysis is a volume which includes at least the whole superior canal – the data stack is cut out of a larger data volume using AMIRA. This is the first step of the data processing. Then – just as it is done with the bone cement phantoms – the DICOM files are imported into Matlab using the same functions as for the phantoms. A 3D matrix with the images is stored. To find the superior canal, we manually picked a number of points lying inside the canal (Figure 43).

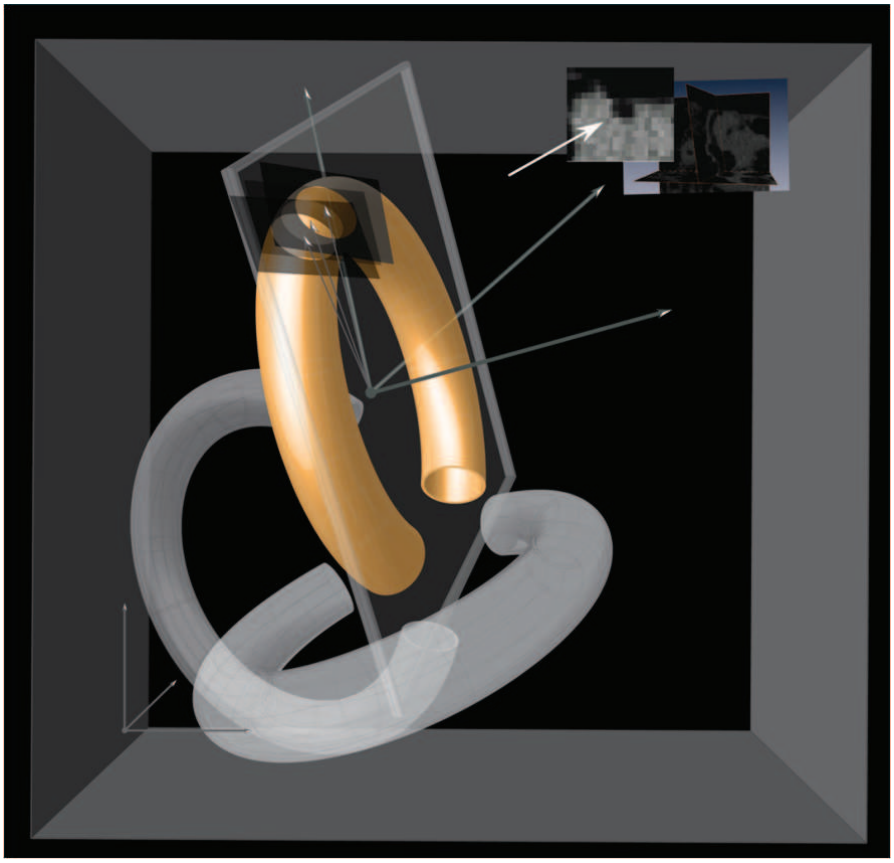

Figure 42 Principle of getting slices along the top of the superior canal. The outer frame indicates the full 3D data stack. The frame indicates a plane along center points of the canal where a circle is fitted. The circle is needed to compute slices normal to the canal.

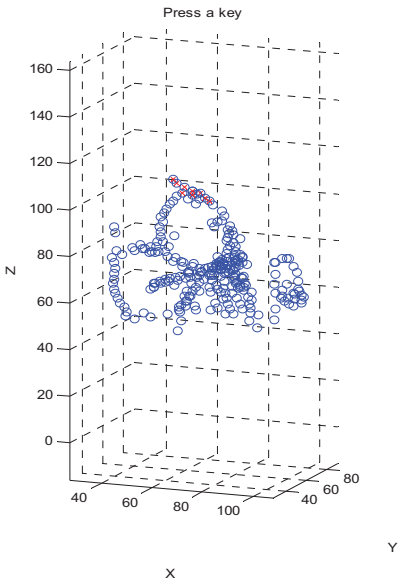

Figure 43 Manually picked points inside the canals.

After that, the rough position of the canals is known. The interesting, upper part of the superior canal is then cut out of the data once more, before a circle is fit to the superior canal which is necessary to generate slices along the canal.

To fit the circle, we need to find the center of the canal tube first. To find the center of the tube on each slice, we first rotate the 3D volume into the y-z plane instead of looking at the data *from above* (in the x-y plane). Then a 11 x 11 px hole detection convolution filter is used which is optimized to find the middle of the superior canal tube on the DICOM images (Figure 44).

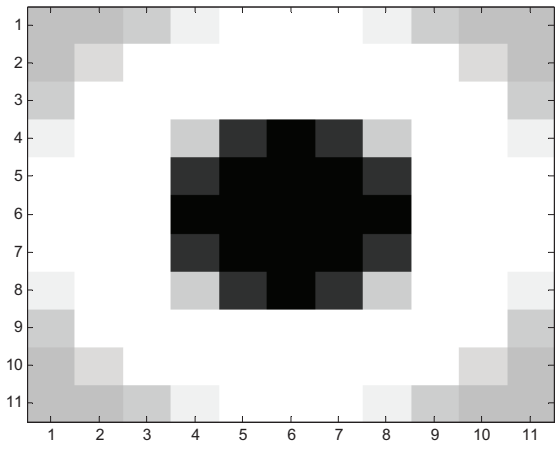

Figure 44 Hole Detection filter to find the center of the superior canal tube on the DICOM slices.

A maximum is automatically rejected if the new position of the canal center on the next slice is too far off the position of the canal center on the previous slice.

Then, the 3D positions of the canal centers are projected onto a plane. This plane is then rotated so that the canal points lie onto the x-y plane. Having done this, a least square fit problem is formulated and solved to compute the center of a circle which fits best to the computed canal center positions – and finally, the circle is projected back to the original orientation of the canal center points. In addition, an arc is selected marking the upper part of the superior canal as region of interest (Figure 45, green).

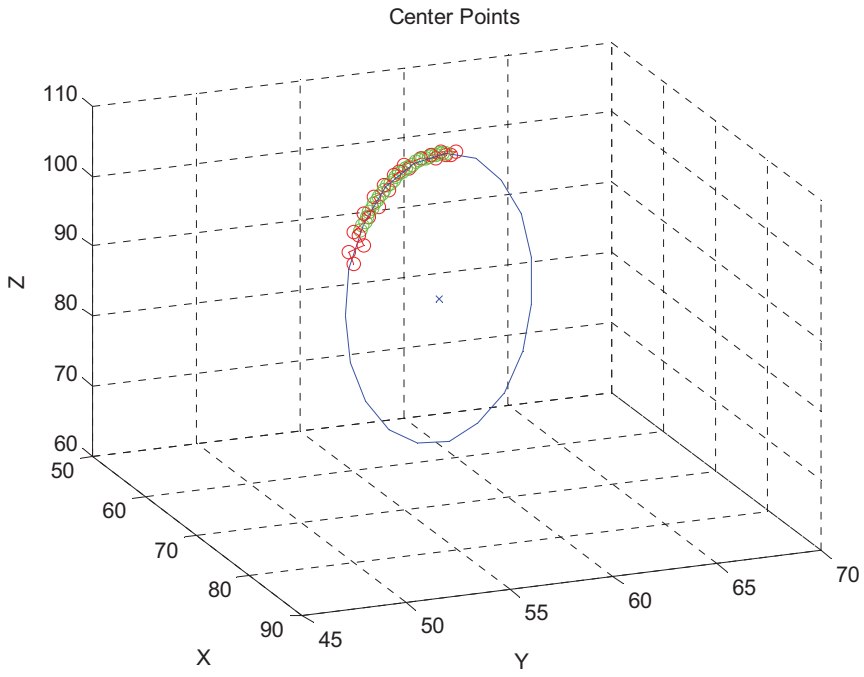

Figure 45 Canal center points with fitted circle describing the superior canal in the 3D image volume.

Now, slices of the upper part of the canal tube have to be made as indicated in Figure 42. First, a row of coordinate systems sitting on the arc are generated to cut slices through the canal. Once the slice planes are calculated, the data stack is cut and the slice planes are made by again *a back projection*, using the same function that did the back projection of the canal circle already. Figure 46 shows the cut out data stack in red, the arc segment containing the canal cut slices in green and the canal and canal circle fit data points in blue/magenta.

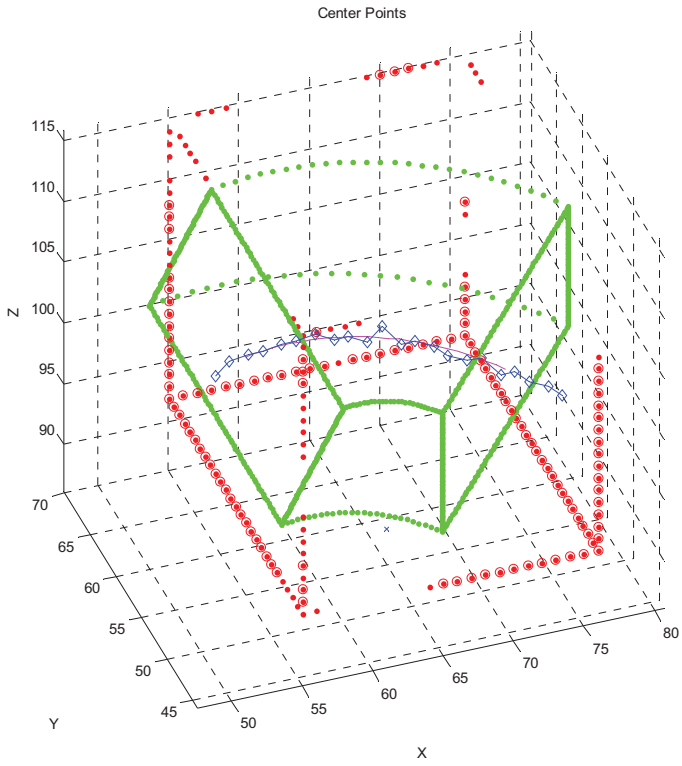

Figure 46 Segment selection for slices through the superior canal (center of the canal is marked blue). The image stack which is cut out of the 3D data stack is indicated in red and the slices through the canal lie whithin the green area.

The slices through the canal are stored in a separate image stack – with images containing the round canal and showing the overlying (eventually dehiscent) bone (Figure 47).

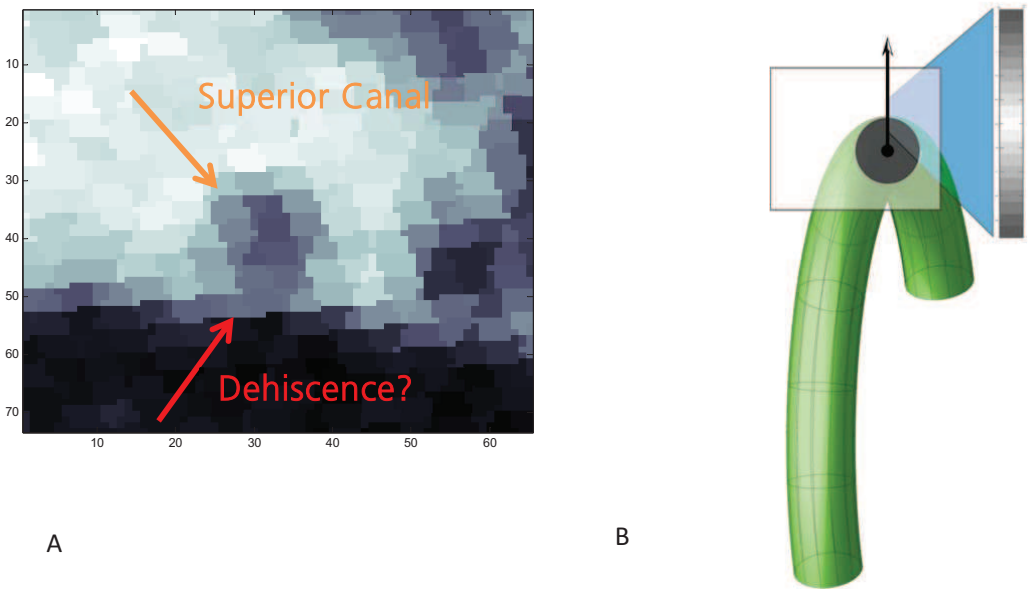

Figure 47A One of the slices through the superior canal with thinned bone overlying the canal. B Path from the center of the canal to the outside. The standard deviation of intensity along the path line can be statistically evaluated.

After that, data along a line following the radius from the center of the canal to the outside can be stored in a vector to see the intensity values along this line.

The single lines can be plotted as in Figure 48 and Figure 49. Figure 48A shows a set of paths through the superior canal set together; Figure 48B shows the corresponding stack with the path marked yellow.

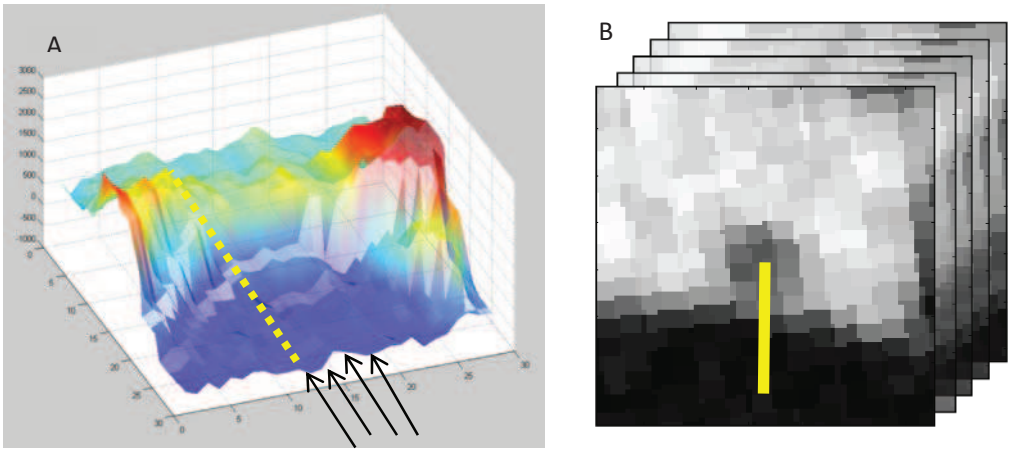

Figure 48 Several paths - one on every slice through the canal - through the superior canal set together. A shows the whole stack of paths set together in one surf plot, with the yellow dotted line indicating a single path as obtained from one slice. B shows a set of slices through the canal with the path line marked yellow.

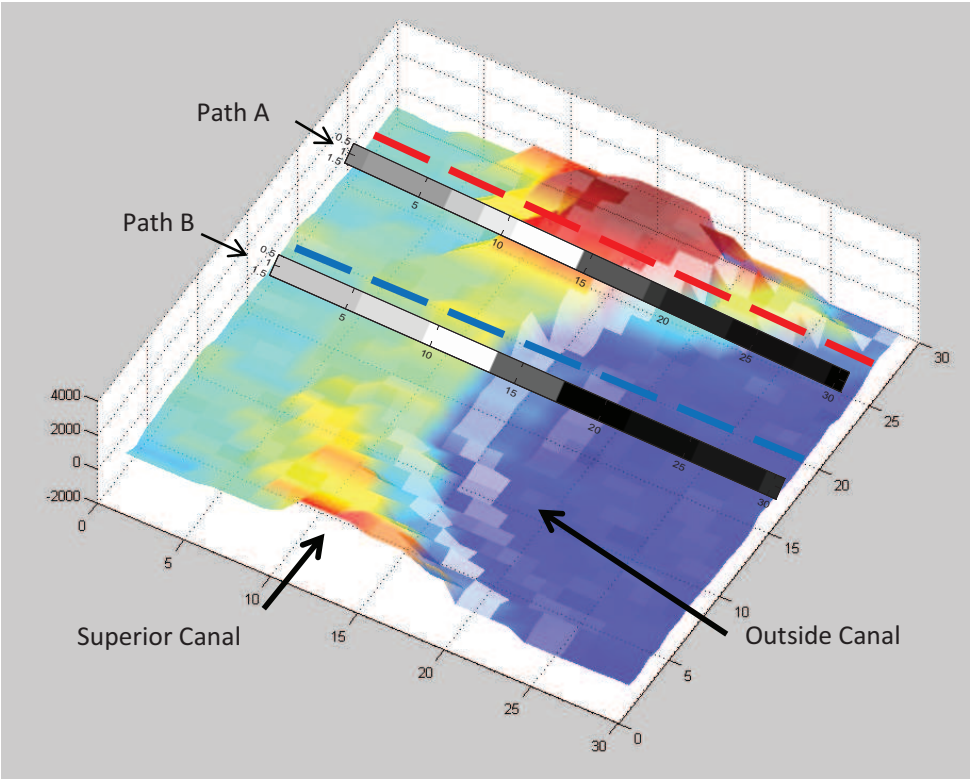

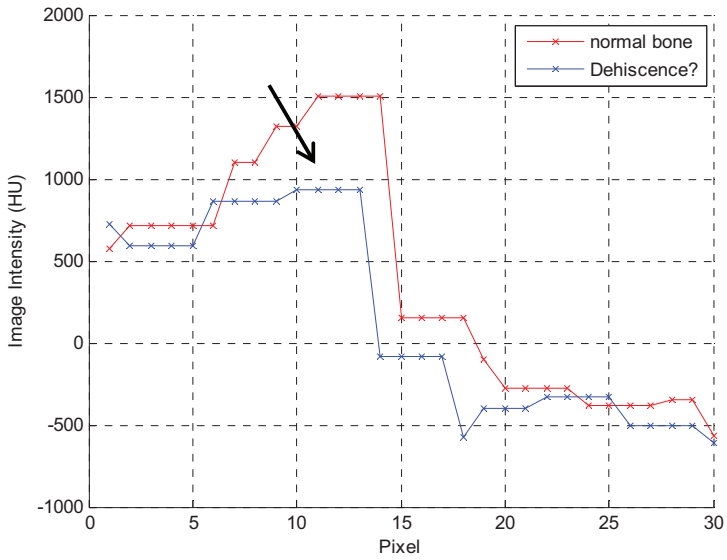

Figure 49A 3D plot of intensity values of the CT scan. The view from above (lower plot) shows the circular shape of the superior canal. The red (path A) and blue (path B) lines correspond to the red and blue graph in (B) below. B The two lines as inserted in (A) plotted as HU intensity values. The black arrow in B shows that there is still a maximum which indicates that there is still bone over the canal and no dehiscence. No peak like this would be a hint for a dehiscence of the canal.

Principle of Canal Analysis – Statistics

Now, a similar analysis can be done with the standard deviations and means of the lines from the canal center towards the outside of the canals. In theory, the intensity profile of one line should have a distinct curvature (i.e. a rise in intensity) in the middle – just where the bone of the canal can be seen. A very low profile can indicate a dehiscence.

Figure 47B shows a graphical explanation of selecting a path from the canal center to the outside. The bar on the right indicates the detected HU intensities along the path. Out of that, further statistical tests can be performed, like an analysis of standard deviations of the path or a comparison of several standard deviations of multiple paths with known bone in the middle. All in all, the goal should be to summarize the data in a receiver operating characteristic (ROC) (Park et al. 2004) to find the HU threshold under which a dehiscence is statistically significant to predict.

Brief description of the Matlab Code

Function/Script	Brief Description	Call/Input
ReadDicomStack4.m	Reads a stack of 3D data of Semicircular Canals from a directory into a 3D matrix – including manual marking of the canal.	`ReadDicomStack2;` `script; no input required`
CanalProjection.m	*** adapted from Thomas Haslwanter *** Best-fit plane: y = ax + bz + c Note that this assumes that the data are somehow lying in the x-z-plane! For all data: [X Z 1] * [a;b;c] = Y The function takes (1) Center Points (3D vectors) of the canals as input and computes (1) points of the canal projected onto the xz plane	`[CenterPoints_projected] = CanalProjection(CenterPoints);`
rot2mat.m	*** from Thomas Haslwanter *** This function takes a rotation vector "rot", and calculates the corresponding rotation matrix.	`R = rot2mat(rot);`

circfit.m	*** By: Izhak bucher 25/oct /1991 *** Source: Matlab FileExchange Optimization function fitting a circle into a set of data points.	`[xc,yc,R,a] = circfit(x,y);`
CanalBackProjection.m	The function takes (1) Center Points (3D vectors) of the canals as input (2) rotation matrix as calculated by CanalProjection.m (3) coefficients abc from CanalProjection.m (4) shift logical 'true' or 'false' - use false if only orientation is rotated back, use true for back projection of positions and computes (1) points of the circle back projected into 3D space	`[CirclePoints] = CanalBackProjection (CirclePoints_projected,R,abc,true);`

3.4.3. Qualitative Volume Analysis in AMIRA

For the evaluation of the placement of the cochlear implants and the vestibular implant, we used AMIRA. The advantage of AMIRA is that it allows relatively fast and easy processing and manipulating of DICOM data sets for non-clinical use. For our studies, we collected scans of several modalities from temporal bone specimen. We inserted cochlear implants into four of them, and a vestibular implant into one. In addition, we used a dry temporal bone and inserted just a vestibular implant electrode into it.

Up to now, image quality has only been evaluated by observer studies; observers were trained ENT surgeons of the Johns Hopkins University School of Medicine. The observers were asked about image quality, noise and spatial resolution to find structures like the inner ear ossicles, the stapes footplate and the placement of the implant electrodes. No computational analysis of the temporal bone specimen was done so far, but one of the next steps – and another project – will be the assessment of several metal artifact reduction algorithms. The aim is to overcome the problem of metal streak artifacts overlying exactly the regions of interest inside the cochlear and canals to determine the exact location of the electrode.

4. Results

4.1. Bone Cement Phantoms

4.1.1. Toshiba Aquilion MSCT vs. Siemens regular Dyna CT

The comparison of the Multi Slice CT and the regular Dyna CT with 1x1 binning shows no better performance of MSCT compared to CBCT.

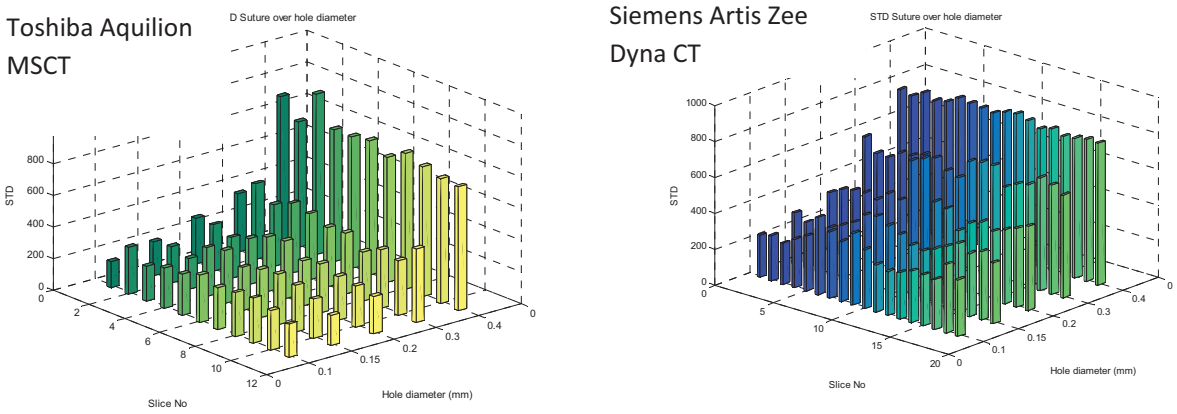

Figure 50 Comparison of Standard deviation over a 5x5 px matrix placed over the hole, separted in hole diameter, Slice number and standard deviation (HU).

Figure 50 shows a comparison over multiple slices of the connection standard deviation in Hounsfield Units over a 5 x 5 pixel matrix placed over the highest intensity pixel over the hole and the hole diameter in mm. A difference that can be seen is that partial volume artifacts are more prominent at the MSCT compared to the CBCT since the curve of standard deviations of the different bore holes scanned with the MSCT is raising steeper compared to the curve obtained from the CBCT.

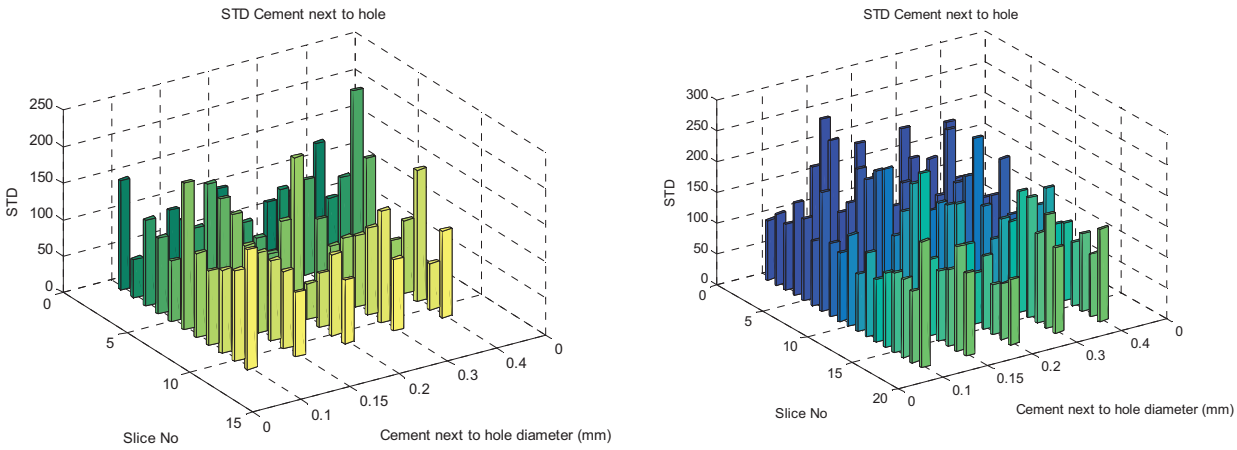

Figure 51 Standard deviation of image noise captured over a 5 x 5 px matrix over solid material. Left: Toshiba MSCT; right: CBCT.

Figure 51 shows the image noise which was also measured by manually selecting a region inside the solid material. Noise was measured on the same slices as where the standard deviation of the holes was calculated.

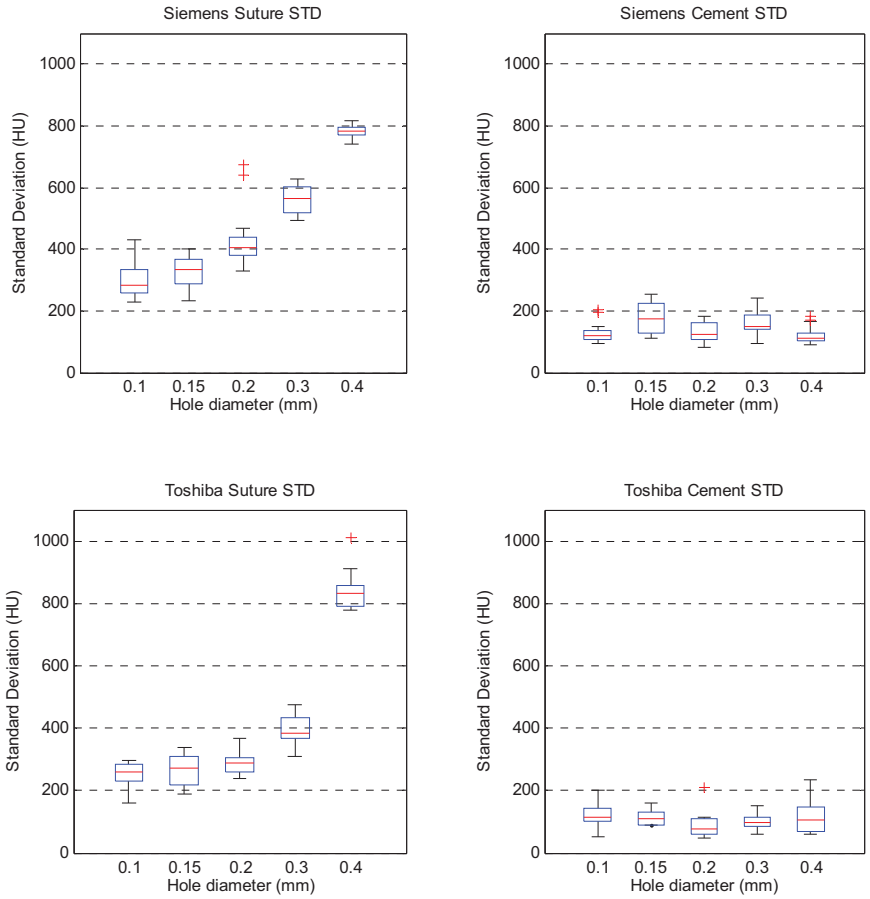

Figure 52 Standard deviation of HU means over different hole diameters over a 5 x 5 pixel matrix acquired with both, the Siemens CBCT and Toshiba MSCT scanners.

The same can be seen in Figure 52 where the standard deviations of the extracted image matrices are calculated over multiple slices and visualized as boxplot. All in all, standard deviations of the image matrix over the hole and solid material are comparable for MSCT and CBCT. As expected, standard deviation increases with the hole diameter, but for both, the MSCT and CBCT, the noise level is well below the standard deviation level of the smallest hole. Both scanners can distinguish significantly between solid material and holes – even the smallest hole (0.1 mm diameter) is detectable by significant statistic means.

4.1.2. Siemens HR Dyna CT 1x1 binning

To evaluate the highest accuracy of the Siemens HR Dyna CT with 1x1 binning, a secondary reconstruction was made. According to the manufacturer, the highest resolution can be achieved by using a sharp HU filter kernel. Other kernels – as the smooth, normal and EE kernel – have yet to be analyzed.

A

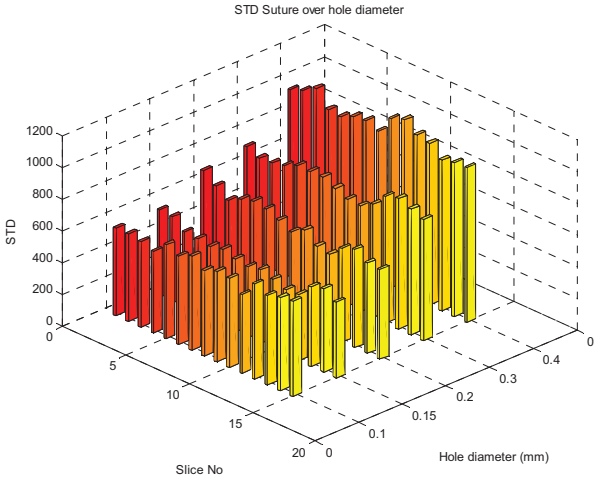

B

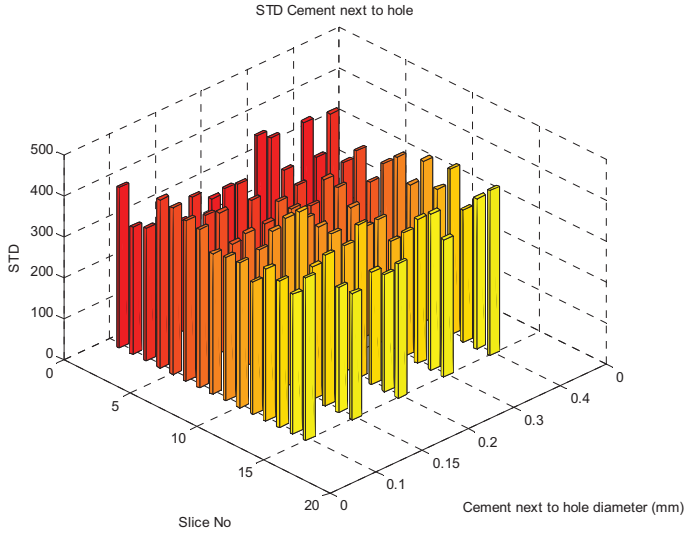

Figure 53 Standard deviation of a 13 x 13 pixel matrix placed over a hole (A) and over random noise (B) in the bone cement.

Compared to Figure 50, the standard deviation of a matrix placed over a hole is higher for the sharp, high resolution reconstruction as shown in Figure 53A. But as shown in Figure 53B, the average noise level is also about twice as high. This can also be seen in the boxplots shown in Figure 54. The standard deviation of the 0.1 mm hole seems to be higher than of the 0.15 mm hole – but the difference can still be considered as within the amount of random noise.

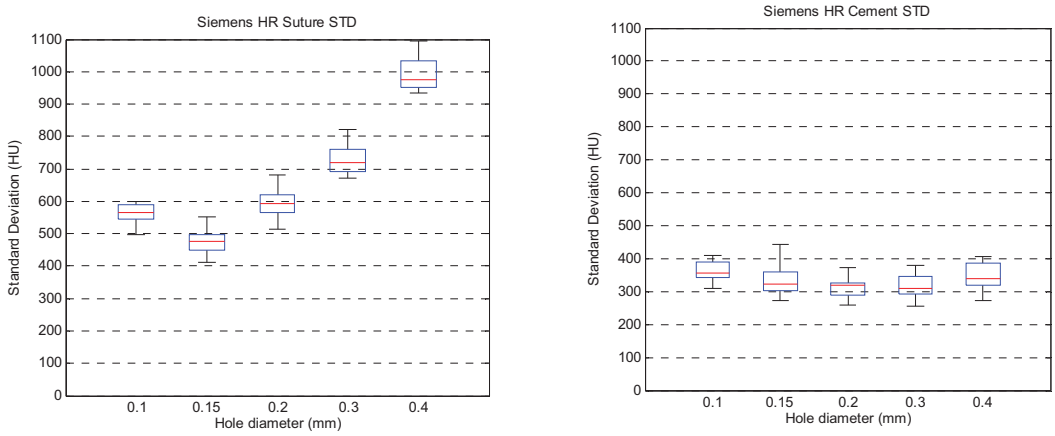

Figure 54 Boxplot of standard deviation over a hole and noise (cement).

4.1.3. Comparison of Noise

Noise is one of the main issues when comparing 1x1 binning high resolution CBCT scans with 2x2 binning MSCT scans, where noise can be expected to be lower. Noise is not a problem to detect a hole as long as the standard deviation of noise is lower than the standard deviation of a selection with a hole – this is the case for all acquired images.

One observation is shown in Figure 55: image noise is considerably higher on images acquired with the 1x1 binning protocol from Siemens, which is expected since 1x1 binning produced more noise than the 2x2 or 3x3 binning used in regular protocols. The comparison of noise in the regular 1x1 binning protocol and after a sharp kernel secondary reconstruction, however, shows less difference in noise.

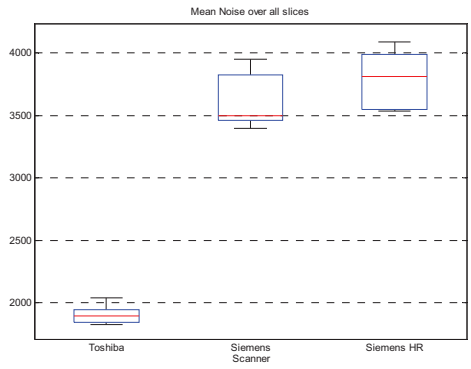

Figure 55 Standard deviation of image noise measure over solid, homogenous material over a 5 x 5 (for 180/190 micron voxel size) and 13 x 13 (for the 80 micron voxel size of the HR reconstruction) pixel matrix. Noise was calculated over a total of 90 slices.

Therefore, limitations of detecting the hole over the noise level exist and are higher for the Siemens 1x1 binning unit compared to the clinical standard MSCT.

The following noise statistics could be calculated:

	Scanner		
	Toshiba MSCT	Siemens CBCT	Siemens HR CBCT
μ	1907	3621	3788
σ	113	286	267
var	12790	81973	71051

Table 6 Statistical noise characteristics of MSCT and CBCT with and without secondary reconstruction.

Table 6 gives the statistical noise characteristics of the CBCT and MSCT scanners.

Noise over solid material and the distribution of HU over holes was tested of normality. Normality was rejected ($p = 7.06*10^{-5}$ for random noise samples) using the one-sample Kolmogorov-Smirnoff test in Matlab (Matlab *kstest*, at 0.05 significance level).

A statistical comparison of noise versus suture can be done by using the non-parametric Wilcoxon ranksum test (Matlab *ranksum*). The aim of this test is to find out if there is a highly significant difference in the median standard deviations of a group of random noise matrices compared to a group of hole matrices.

The null hypothesis is rejected for every scanner and hole diameter. The following p-values were calculated (Table 7):

	Toshiba MSCT	Siemens Dyna CT	Siemens HR Dyna CT
Hole diameter (mm)	p value $*10^{-5}$		
0.1	0.001398	0.03228	0.3392
0.15	0.000815	0.05311	0.6152
0.2	0.000815	0.03228	0.3392
0.3	0.000815	0.03228	0.3392
0.4	0.000815	0.03228	0.3392

Table 7 P-values of comparing a group of noise samples with a group of hole samples with different diameters. Values given as $p*10^{5}$.

To overcome the noise problem of the high resolution reconstruction, several possibilities exist: using a different filter kernel (*normal* or *smooth* instead of *sharp*) is one. Another *quick and dirty* fix would be to do some averaging. Just for a trial, the intensities of three DICOM slices (n-1, n, n+1; n: number of slice) where summed up and divided by three. The result is an average image with a loss in resolution but an overall SNR improvement. The boxplot including the averaged high resolution reconstruction is shown in Figure 56.

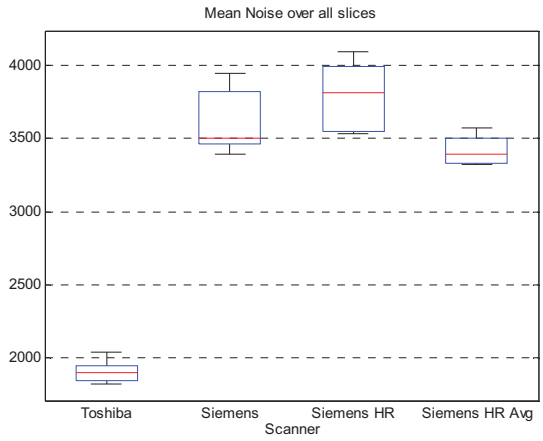

Figure 56 Mean noise over all slices, including an averaged *version of the high resolution reconstruction.*

Noise is now lower in standard deviation – almost comparable to the MSCT scanner – and lower in mean.

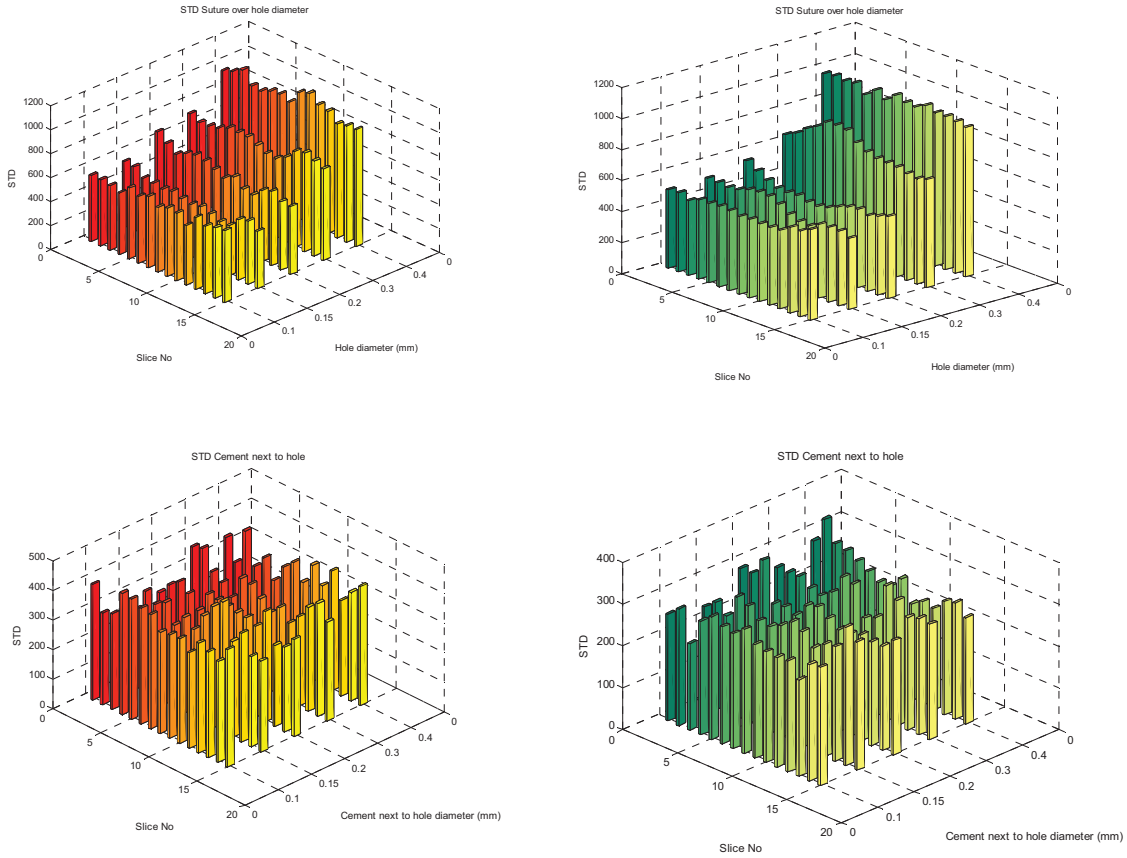

Table 8 Comparison of noise before (left, red) and after (right, green) averaging.

Table 8 shows a comparison of the same slices before and after averaging over three image matrices.

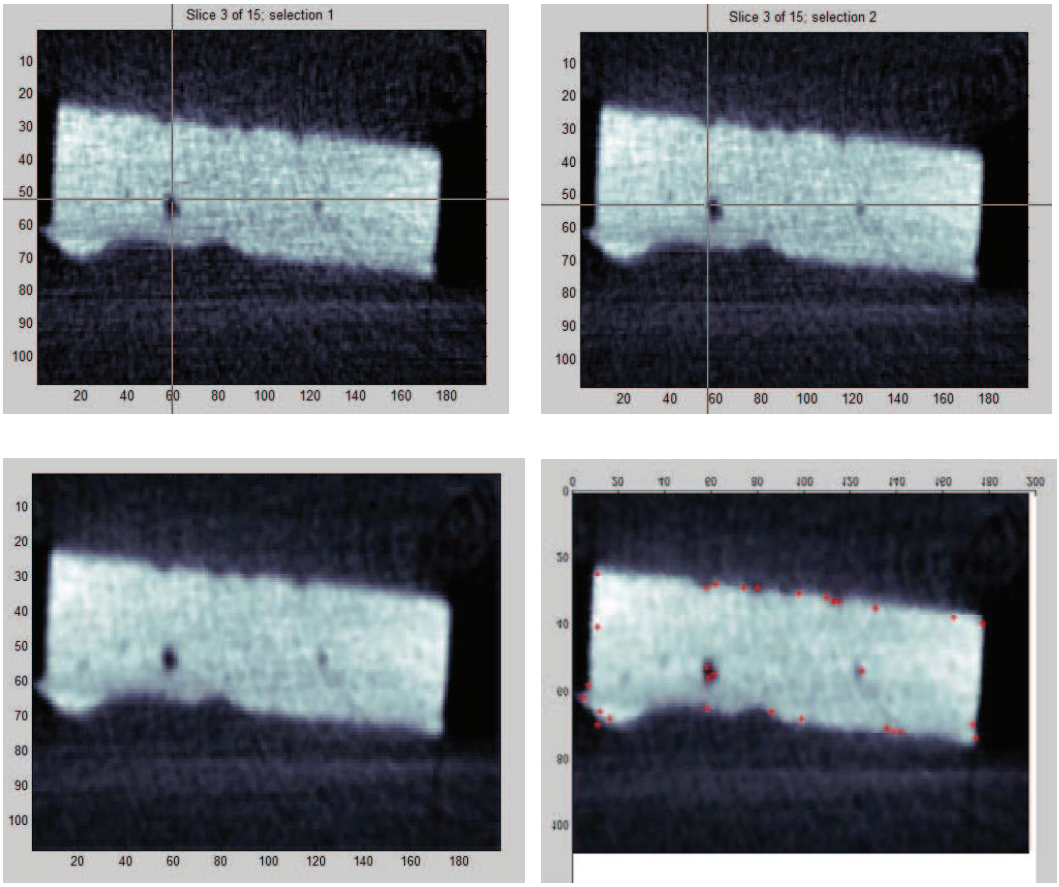

Figure 57 Left up: Siemens high resolution 1x1 binning; Right up: with averaging over 3 slices. Left down: Noise reduction by using a median filter with a 2 x 2 matrix and an additional Gaussian lowpass filter with a 3 x 4 matrix and a sigma of 0.5. Right down: Same slice with adaptive Wiener filtering using a 3 x 3 matrix and a manually set noise threshold (100,000) In addition, a Harris corner detection algorithm was applied (red dots) – usage of that could be to automatically detect the prescence of a hole whithin the slice.

Figure 57 shows a comparison of the regular high resolution image on the left. On the right, the same DICOM with averaging over three slices is shown. Of course, more advanced filter techniques have yet to be tested for usability of detecting holes and removing noise for our purposes. Common filter techniques used for CT imaging would be regular median filters, adaptive Wiener filters and wavelet thresholding (Ribeiro et al. 2007). The advantage of averaging over multiple slices in this case is, though, that noise can be removed without influencing the appearance of the possible hole itself. The only consideration that has to be made is that by averaging, the slice thickness is artificially thickened again – but with a slice thickness of < 80 microns this should be tolerable – at least for detecting a dehiscence.

4.1.4. Comparison of the Standard Deviations

The main aim is to find out if there is a statistical test that tells us if we – by taking one random matrix – can find out if due to the difference in standard deviations the random sample contains a hole or just noise. So a test is needed to compare a group of noise data with a single selected slice.

Although the data is not normally distributed, an ANOVA (Table 9) can be made by using the Brown-Forsythe version of it. Basically, it calculates a standard one-way ANOVA with a centering transformation which is done by subtracting each value from the group median or mean and compares it to the critical value of the F-distribution. To see the functioning of the ANOVA test, a sample slice of either noise or a hole was taken and compared to a stack of noise matrices. The aim was to figure out if there is a significant difference in the ANOVA when a hole slice was added.

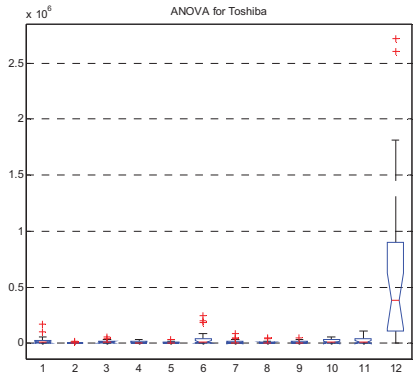

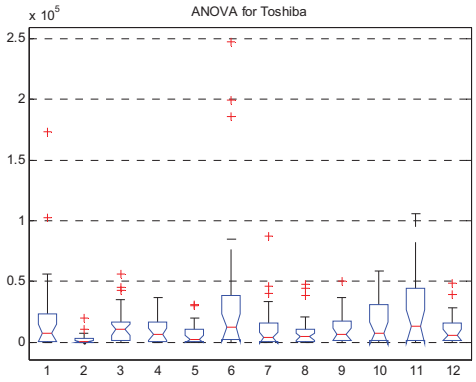

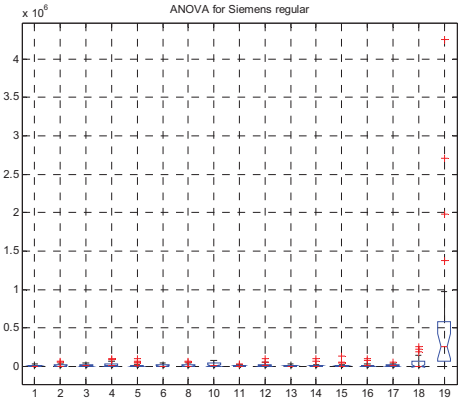

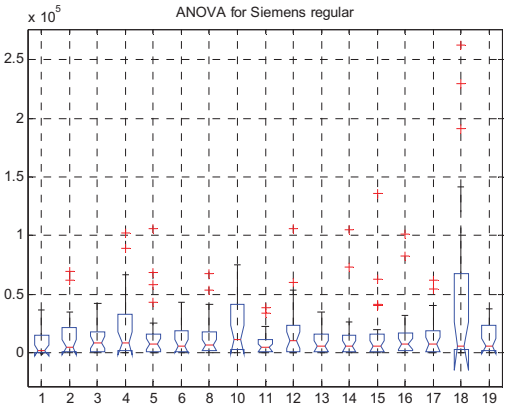

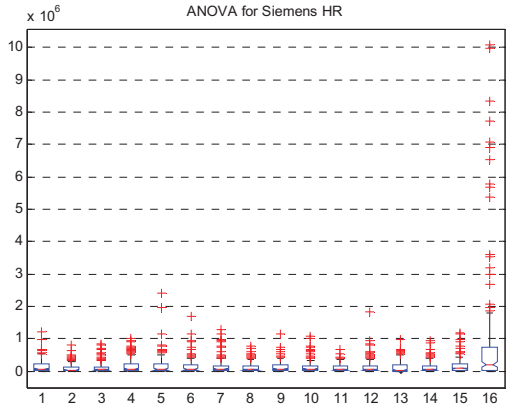

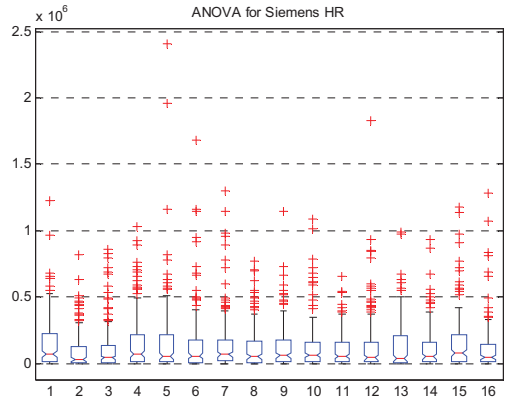

Table 9 ANOVA for Toshiba, Siemens regular and Siemnes HR scans; Left: the last data stack is a matrix containing a hole with 0.1 mm diameter. Right: the last right stack of data is a matrix containing only noise.

Table 9 shows the results of the ANOVA with a hole matrix and a noise matrix as final element, respectively. It can clearly be seen that every scanner detects a hole of 0.1 mm with this method but noise can also be seen as such. This would be a qualitative approach to evaluate whether noise or a hole can be seen on the selected area.

Another test that is suitable to distinguish between an area with a hole and an image containing only noise is the Fligner-Killeen test (Table 10).

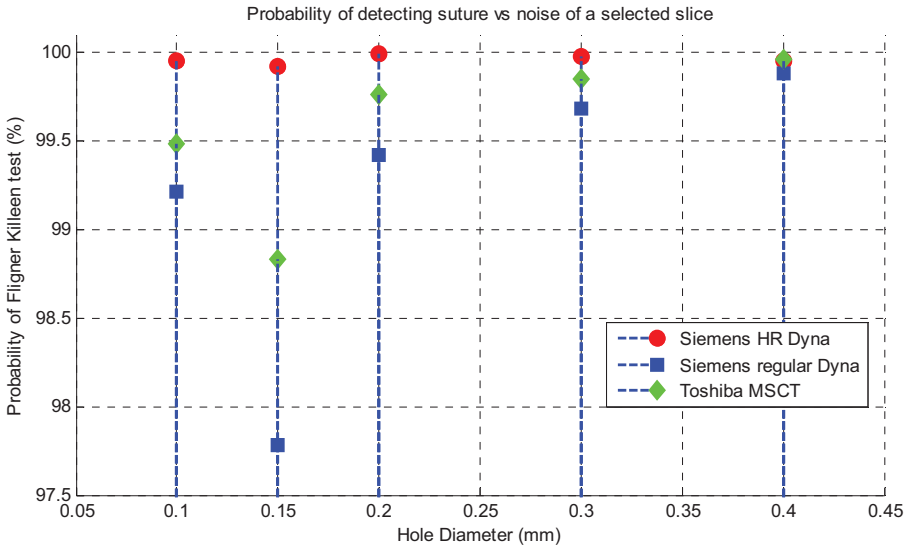

Table 10 P-values after testing a randomly selected hole image against a the median of a group of noise data. The results for all three scanners are shown.

The Fligner-Killeen test as shown in Table 10 and Table 11 was used to test whether a randomly picked image matrix containing a hole could be detected with which certainty. Probability of having the area containing a hole is plotted against hole diameter. The test shows that the best results could be achieved using the secondary high resolution reconstruction of the Siemens CBCT Dyna CT, followed by the Toshiba MSCT and finally by the regular Siemens Dyna CT without high resolution reconstruction. The good results of the MSCT are because noise is very low on images acquired with the MSCT compared to CBCT, where noise is a problem. Finding small structures under a lot of noise makes finding a hole difficult.

The drawback of the high resolution reconstruction, however, is that the rate of detecting false-positives is also very high. This can be seen in the following tables, showing first (Table 11) the p-values when a group of noise is compared to a slice containing a hole. The p-value in this case gives the probability of having detected a hole instead of random noise.

Hole vs Noise	Toshiba MSCT	Siemens Dyna CT	Siemens HR Dyna CT
Diameter (mm)	p-value of Fligner-Killeen test		
0.1	0.0052	0.0079	0.0005
0.15	0.0117	0.0222	0.0008
0.2	0.0024	0.0058	0.0001
0.3	0.0015	0.0032	0.0002
0.4	0.0004	0.0012	0.0005

Table 11 P-values of Fligner Killeen test comparing a slice with a hole with noise data. P-value indicates the probability of having detected a hole.

Performing the same test with a slice containing noise (Table 12) gives the same probability of having detected a hole – the low values of the high resolution Dyna CT indicate that due to the amount of noise, a noise sample is more likely to be detected as a hole. This makes the high resolution reconstruction the wrong candidate for detecting a hole – at least for bone cement phantoms.

Noise vs Noise	Toshiba MSCT	Siemens Dyna CT	Siemens HR Dyna CT
Diameter (mm)	p-value of Fligner-Killeen test		
0.1	0.198	0.773	0.082
0.15	0.824	0.852	0.009
0.2	0.585	0.608	0.028
0.3	0.558	0.632	0.002
0.4	0.344	0.403	0.004

Table 12 P-values of Fligner Killeen test comparing a slice with only noise with noise data. P-value indicates the probability of having detected a hole.

4.2. Results Canal Dehiscence / Head Specimen

A similar principle as shown with the bone cement phantoms can be used to detect a dehiscence or thin bone overlying the superior canal. The difference is, that in this case not a hole has to be detected but the standard deviation along a path from inside to outside of the canal can estimate whether there is a dehiscence or not. The scan we used for our study is acquired from a head specimen with very thin bone which is still intact.

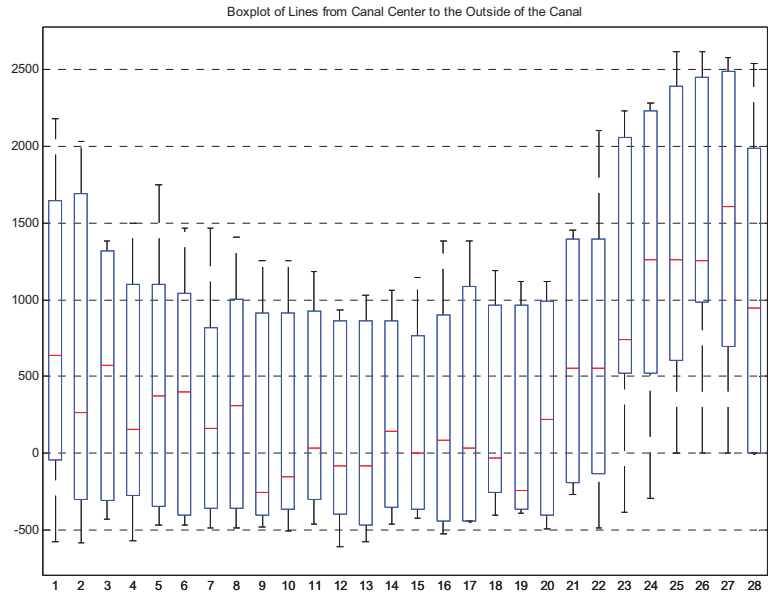

Figure 58 Statistical distribution of HU intensities along lines from the center of the canal towards the outside. A significant lower standard deviation would indicate a dehiscence. A large standard deviation indicates a layer of bone between the inside of the canals and the outside.

Figure 58 shows a boxplot graph of paths from inside a canal to the outside – from several slices through the tube of the superior canal. At least, the boxplot indicates the thinning of the bone – in order to detect a dehiscence or to distinguish between dehiscence or thin bone, the statistical test parameters have to be optimized; a receiver operating characteristic (ROC) analysis would also be a possibility: to find a HU threshold under which an opening of the canal is the case – as suggested by (Tavassolie et al. 2012). A ROC curve is an illustration of the performance of a binary classifier system and its discrimination threshold; plotted are true positives against false positives at various threshold settings.

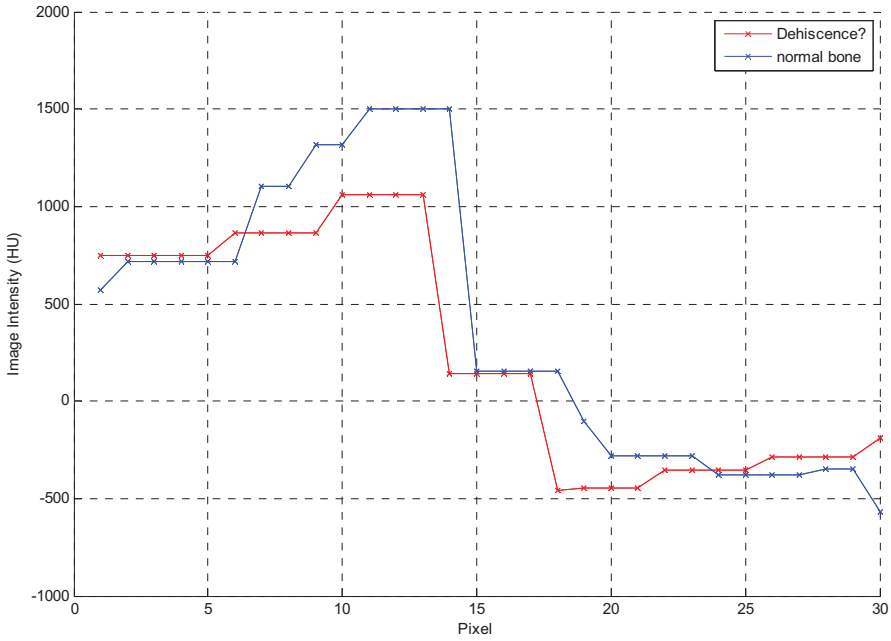

Figure 59 Two intensity lines; one (blue) showing a normal *CT with bone and a higher variation in intensity, the other one (red) might indicate either dehiscence or a very thin bone.*

The blue graph in Figure 59 indicates at least thin bone, whereas the red line has a curvature as expected: showing a higher standard deviation in HU values; a higher standard deviation in HU values means that there are both: light bone and dark material in- and outside of the canals.

4.3. Qualitative Volume Analysis in AMIRA

Three cadaveric temporal bones were drilled open and cochlear implants (CIs) were inserted. Another temporal bone specimen was provided with both, a cochlear implant and a vestibular implant. This can be of interest for intra-operative CT imaging, since re-implantation after electrode migration of CIs is still a problem (van der Marel et al. 2012). The question that should be answered with the scans of the vestibular implant was whether the implant electrodes were on the right location or inserted too far into the canals. That would result in a wrong or insufficient vestibular stimulation if implanted in patients. Up to now, we assessed only qualitatively the accuracy and resolution of the CBCT images. Figure 60 shows a volume rendering of a dry temporal bone with a vestibular implant electrode in the three canals (arrows on the left image).

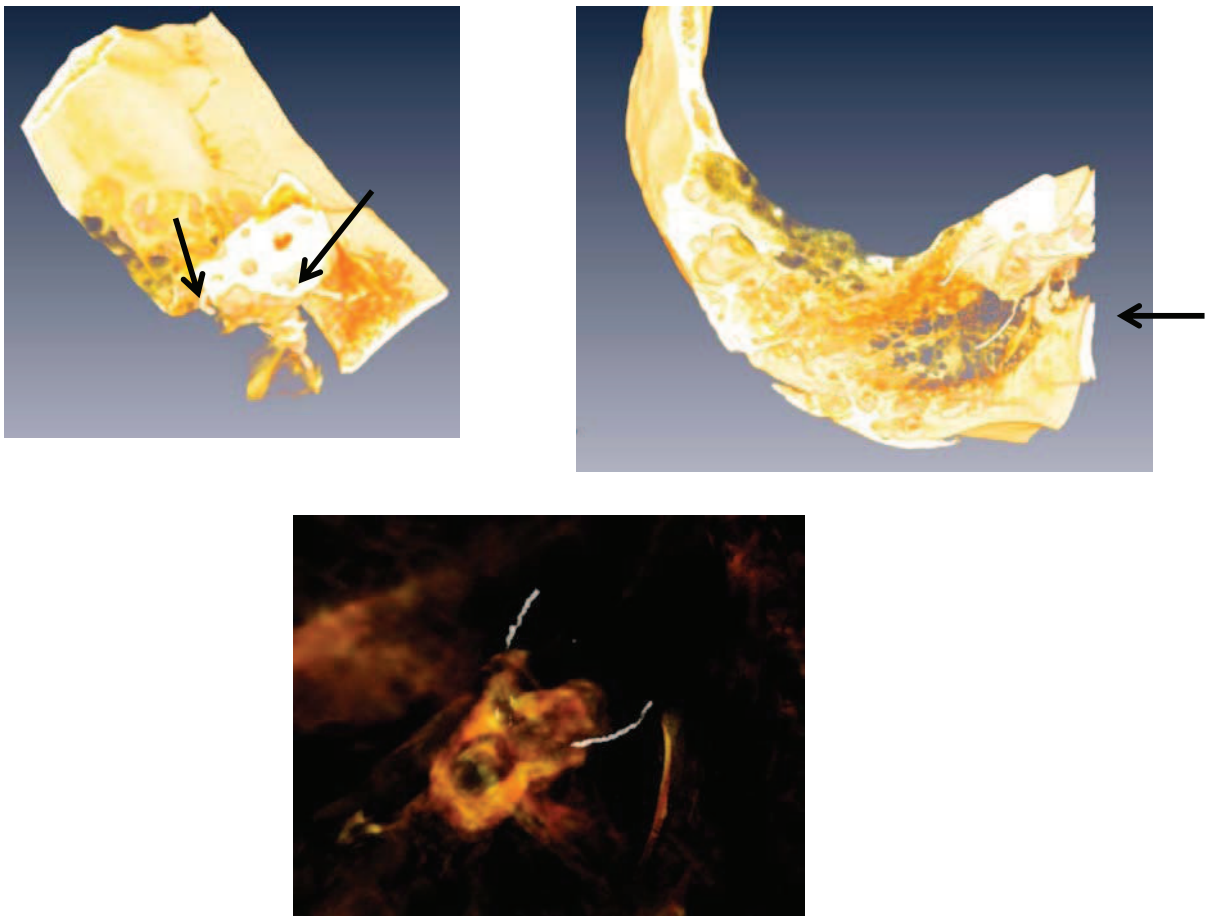

Figure 60 High resolution CBCT scan of a dry temporal bone with a vestibular implant. The arrows on the upper left image indicate the vestibular implant electrodes in the canals. The arrow on the upper right image marks the inner ear ossicles. On the lower image, the labyrinth with the electrodes is reconstructed as MIP image.

Our conclusion by evaluating the scans is that for the application of the assessment of the placement of vestibular implants, CBCT can be used. CBCT scans allow resolving structures like the inner ear ossicles and the canals in enough detail so that the right placement can be seen. The advantage of using CBCT in this case is that even the regular head protocols with standard kVp and mAs deliver satisfying results in terms of resolution, leading to less radiation exposure for patients in comparison with MSCT scans.

5. Discussion and Outlook

5.1. Discussion and Summary

The best way to diagnose a semicircular canal dehiscence is to *see* the dehiscence - it's a clear opening on the upper part of the canal. It's not surprising, that diagnosis of dehiscence is therefore based on Computed Tomography scans of the inner ear. And the gold standard for imaging of the temporal bone has always been Multi Slice Computed Tomography – from the beginning of SCD studies onwards (Crane et al. 2008). A problem with MSCT is that it can overestimate the size of the dehiscence. In worst cases, it leads to a false positive diagnosis and to an unnecessary surgical procedure (Penninger et al. 2011; Tavassolie et al. 2012).

Recently, Cone Beam CTs are evaluated for their ability to resolve fine structures of the head – including sinus and temporal bone scans (Damstra et al. 2011; Fahrig et al. 2006; Kau et al. 2009; Miracle and Mukherji 2009b; Peltonen et al. 2009). Most of the recent studies which compare image quality of CBCT with MSCT are human observer-based. In our study, we wanted to use another, quantitative and objective approach to compare spatial resolution. We made bone cement phantoms and inserted surgical suture of different diameters (the thinnest had a diameter of 0.1 mm). We wanted to know, if we can program an algorithm in Matlab that can distinguish between a hole structure and image noise on the CT scans. By cutting orthogonal slices through the bone cement phantoms we could place a 5 x 5 pixel matrix over an area of interest – either noise or a possible hole. Noise is one of the main disadvantages of CBCT, and noise is even increased with the new 1x1 binning protocols that we tested. Fine structures can disappear in noise on high resolution CBCT scans if dose is kept at the same level as without 1x1 binning. A secondary reconstruction reduces voxel size for the price of another increase in noise. However, all scanners could detect small holes in the bone cement phantoms.

We compared the standard deviations in Hounsfield Units of hole and noise areas of the 25 pixel image matrix and used a Fligner-Killeen test for non-normally distributed populations. We showed that both, CBCT and MSCT can significantly resolve structures smaller than 0.1 mm in diameter.

After having shown that small holes on CT scans can be detected with statistical methods, we investigated if we could detect a canal dehiscence with this method. We developed an algorithm to transform a 3D data volume containing a superior canal in such a way that we could show if there is still bone overlying the superior canal. To show that, we used a human cadaveric head specimen, opened the skull and created an artificial dehiscence on the superior canal of the right ear. Then we scanned the specimen with several scan parameters and scanners. Based on such a scan, we developed the algorithm to transform the DICOM stack of a dehiscence scan. It is a combination

of a series of 3D projections, rotations of the data volume and filtering with a hole detection filter to find the canal structure. By calculating paths from the inside of the canal to the outside, we get the same type of data as with the bone cement phantoms. A large standard deviation shows that there is still intact bone between the inside of the canal and the outside. A lower standard deviation indicates an opening of the canal. This means we have found a method to perform a reliable analysis method to help finding out if a dehiscence is likely on a scan where a human observer is not certain if he can see a dehiscence or not.

5.2. Outlook

However, this is not the end of the line: what we did in our first study was to compare the spatial resolution of a Toshiba high-accuracy 64 slice MSCT with a newly developed Siemens Artis Zee Dyna CBCT unit with 1x1 binning protocol for highest resolution. If we compare the MSCT with the *regular*, standard 1x1 binning protocol, the CBCT is slightly better in spatial resolution, but not superior. We then can do a secondary reconstruction of the sinogram to achieve a higher resolution – which in this case means reducing the voxel size from about 200 microns to 60 microns – the latter being as good as a µCT. The secondary reconstruction really enhances spatial resolution, but adds a lot of noise to the resulting DICOM images. Again, it has to be said that the analyzed scans were taken with a standard and not optimized protocol – there is still a lot of room for improvement on this end. The increase in noise resulted in less detectability of fine structures, but with simple averaging over three DICOM slices, noise could strongly be reduced and the SNR could be increased. A next step for further analysis would be to optimize the scanner parameters so that noise reduction is done at the acquisition. For this, we made several scans with the CBCT unit and in a next step can evaluate image quality versus dose and see if maybe a slight increase in dose could be a benefit for at least a patient with a prior borderline CT – that means a scan where it is unclear whether there is dehiscence or not.

All the analysis of image noise for detecting fine structures was done with bone cement phantoms were holes were drilled and surgical sutures with standardized diameters were inserted. In the first part of this thesis it was shown that noise and image quality could be analyzed based on a statistical comparison of standard deviations of an image matrix. This image matrix was in our case a 5 x 5 or 13 x 13 pixel (depending on the voxel size) matrix manually placed over an area of interest where a hole was expected.

Once it could be shown that the noise analysis and hole detection over standard deviations worked, the next step was to use this principle for the analysis of semicircular canal dehiscence.

We used a head specimen, scanned the inner ears with several scanning parameters and developed an image processing algorithm to manipulate the image so that the thinnest part of the superior canal is detected. This is the basis for performing a statistical analysis and to get a ROC out of the CT data. The goal is to find a HU threshold where a dehiscence can be detected with statistical significance. This approach is also the basis to quantitatively compare the scans that we made with the different CT scanners and to finally do a non-observer based evaluation of CBCT and MSCT. In addition, we can optimize the parameters of the CBCT scanners to get the best possible parameter set for inner ear imaging for several aims – like diagnosis of SCDS. The parameters that we varied in our scans include dose, tube current, tube voltage, Copper beam hardening filter,

edge enhancement algorithms prior to the backprojection, different backprojection and reconstruction kernels (Hounsfield and Edge Enhancement; normal, smooth and sharp) and high resolution secondary reconstructions with 1x1 binning protocols: all in all, about 300 GB of CT data that can be analyzed.

A further outlook on what can be done with our CT scans is an evaluation of metal artifact reduction algorithms. The goal in this case is to optimize the filter parameters and the reconstruction in a way that intra operative imaging during a CI implantation is feasible – the placement of the electrodes and re-implantations are still a known and common problem in CI users (Aschendorff 2011; Barker et al. 2009; Cerini et al. 2008; van der Marel et al. 2012).

Another study we started with our scans is a comparison of dose and image quality – by taking a whole head for the head scans (instead of using just temporal bone specimen), we can now give exact dose values and measure image quality with the same scanning protocols as we can do with patients afterwards.

6. References

1. Cochlear Implant. 2005. Wikimedia Commons, NIH.
Ref Type: Art Work

2. Cochlear Duct Histology. 2011. University of Michigan.
Ref Type: Art Work

3. American Association for Physicists in Medicine. AAPM Dose Check Guidelines . (version 1.0). 4-27-2011. http://www.aapm.org/pubs/CTProtocols/documents/NotificationLevelsStatement.pdf.
Ref Type: Conference Proceeding

4. Aschendorff A (2011) Imaging in cochlear implant patients. GMS Curr Top Otorhinolaryngol Head Neck Surg 10:Doc07

5. Aw ST, Todd MJ, Aw GE, Magnussen JS, Curthoys IS, Halmagyi GM (2006) Click-evoked vestibulo-ocular reflex: stimulus-response properties in superior canal dehiscence. Neurology 66:1079-1087

6. Aw ST, Welgampola MS, Bradshaw AP, Todd MJ, Magnussen JS, Halmagyi GM (2010) Click-evoked vestibulo-ocular reflex distinguishes posterior from superior canal dehiscence. Neurology 75:933-935

7. Barker E, Trimble K, Chan H, Ramsden J, Nithiananthan S, James A, Bachar G, Daly M, Irish J, Siewerdsen J (2009) Intraoperative use of cone-beam computed tomography in a cadaveric ossified cochlea model. Otolaryngol Head Neck Surg 140:697-702

8. Brandt T, Strupp M (2010) Clicking the eye muscles? The diagnostic value of sound-evoked vestibular reflexes. Neurology 75:848-849

9. Brödel, Max. Walters Collection Illustration #933. 1936. Johns Hopkins University School of Medicine, Walters Collection of the Max Brödel Archives, Department of Art as Applied to Medicine.
Ref Type: Art Work

10. Carey JP, Minor LB, Nager GT (2000) Dehiscence or thinning of bone overlying the superior semicircular canal in a temporal bone survey. Arch Otolaryngol Head Neck Surg 126:137-147

11. Cerini R, Faccioli N, Barillari M, De IM, Carner M, Colletti V, Pozzi MR (2008) Bionic ear imaging. Radiol Med 113:265-277

12. Chen B, Ning R (2002) Cone-beam volume CT breast imaging: feasibility study. Med Phys 29:755-770

13. Chiarovano E, Zamith F, Vidal PP, de WC (2011) Ocular and cervical VEMPs: a study of 74 patients suffering from peripheral vestibular disorders. Clin Neurophysiol 122:1650-1659

14. Chien WW, Carey JP, Minor LB (2011) Canal dehiscence. Curr Opin Neurol 24:25-31

15. Chittka L, Brockmann A (2005) Perception Space - The Final Frontier. PLoS Biol 3:e137

16. Colebatch JG, Halmagyi GM, Skuse NF (1994) Myogenic potentials generated by a click-evoked vestibulocollic reflex. J Neurol Neurosurg Psychiatry 57:190-197

17. Crane BT, Minor LB, Carey JP (2008) Three-dimensional computed tomography of superior canal dehiscence syndrome. Otol Neurotol 29:699-705

18. Cremer PD, Minor LB, Carey JP, Della Santina CC (2000) Eye movements in patients with superior canal dehiscence syndrome align with the abnormal canal. Neurology 55:1833-1841

19. Curthoys IS, Iwasaki S, Chihara Y, Ushio M, McGarvie LA, Burgess AM (2011) The ocular vestibular-evoked myogenic potential to air-conducted sound; probable superior vestibular nerve origin. Clin Neurophysiol 122:611-616

20. Curthoys IS, Markham CH, Curthoys EJ (1977) Semicircular duct and ampulla dimensions in cat, guinea pig and man. J Morphol 151:17-34

21. Damstra J, Fourie Z, Huddleston Slater JJ, Ren Y (2011) Reliability and the smallest detectable difference of measurements on 3-dimensional cone-beam computed tomography images. Am J Orthod Dentofacial Orthop 140:e107-e114

22. Dössel O (2000) Bildgebende Verfahren in der Medizin. Springer, Berlin, Heidelberg

23. Fahrig R, Dixon R, Payne T, Morin RL, Ganguly A, Strobel N (2006) Dose and image quality for a cone-beam C-arm CT system. Med Phys 33:4541-4550

24. Gupta R, Bartling SH, Basu SK, Ross WR, Becker H, Pfoh A, Brady T, Curtin HD (2004) Experimental flat-panel high-spatial-resolution volume CT of the temporal bone. AJNR Am J Neuroradiol 25:1417-1424

25. Gupta R, Cheung AC, Bartling SH, Lisauskas J, Grasruck M, Leidecker C, Schmidt B, Flohr T, Brady TJ (2008) Flat-panel volume CT: fundamental principles, technology, and applications. Radiographics 28:2009-2022

26. Gupta R, Grasruck M, Suess C, Bartling SH, Schmidt B, Stierstorfer K, Popescu S, Brady T, Flohr T (2006) Ultra-high resolution flat-panel volume CT: fundamental principles, design architecture, and system characterization. Eur Radiol 16:1191-1205

27. Halmagyi GM, Colebatch JG (1995) Vestibular evoked myogenic potentials in the sternomastoid muscle are not of lateral canal origin. Acta Otolaryngol Suppl 520 Pt 1:1-3

28. Haslwanter, T. Ampulla of Semicircular Canal. 2-6-2011a. Wikimedia Commons.
Ref Type: Art Work

29. Haslwanter, T. Otoliths w Cross Section. 2-15-2011b. Wikimedia Commons.
Ref Type: Art Work

30. Hu H (1998) Multi Slice Helical CT: Scan and Reconstruction. Med Phys 26:5-18

31. International Commission of Radiological Protection (2010) Radiation and your Patient: A guide for Medical Practitioners. International Commission on Radiological Protection

32. Kalender WA (2006) Computed Tomography. Wiley,

33. Kapila S, Conley RS, Harrell WE, Jr. (2011) The current status of cone beam computed tomography imaging in orthodontics. Dentomaxillofac Radiol 40:24-34

34. Kau CH, Bozic M, English J, Lee R, Bussa H, Ellis RK (2009) Cone-beam computed tomography of the maxillofacial region--an update. Int J Med Robot 5:366-380

35. Lechner N (2011) Qualitaetssicherung iin der Roentgendiagnostik. Strahlenschutz in der Medizindiagnostik. Skriptum zur Vorlesung

36. Lee, D. Middle Fossa Craniotomy. 2011. Otosurgery.org.
Ref Type: Art Work

37. Leigh RJ, Zee DS (1999) The Neurology of Eye Movements. Oxford University Press, New York

38. Ludlow JB (2011) A manufacturer's role in reducing the dose of cone beam computed tomography examinations: effect of beam filtration. Dentomaxillofac Radiol 40:115-122

39. Ludlow JB, Ivanovic M (2008) Comparative dosimetry of dental CBCT devices and 64-slice CT for oral and maxillofacial radiology. Oral Surg Oral Med Oral Pathol Oral Radiol Endod 106:106-114

40. Manske, M. Cochlea Crosssection. 11-6-2004. Wikimedia Commons.
Ref Type: Art Work

41. Minor LB (2000) Superior canal dehiscence syndrome. Am J Otol 21:9-19

42. Minor LB (2005) Clinical manifestations of superior semicircular canal dehiscence. Laryngoscope 115:1717-1727

43. Minor LB, Cremer PD, Carey JP, Della Santina CC, Streubel SO, Weg N (2001) Symptoms and signs in superior canal dehiscence syndrome. Ann N Y Acad Sci 942:259-273

44. Minor LB, Solomon D, Zinreich JS, Zee DS (1998) Sound- and/or pressure-induced vertigo due to bone dehiscence of the superior semicircular canal. Arch Otolaryngol Head Neck Surg 124:249-258

45. Minor LB, Carey JP (2010) Chapter 30 - Superior semicircular canal dehiscence syndrome and perilymphatic fistula. In: Scott DZE (ed) Handbook of Clinical Neurophysiology
Vertigo and Imbalance: Clinical Neurophysiologyof the Vestibular System. Elsevier, pp 415-427

46. Miracle AC, Mukherji SK (2009a) Conebeam CT of the head and neck, part 1: physical principles. AJNR Am J Neuroradiol 30:1088-1095

47. Miracle AC, Mukherji SK (2009b) Conebeam CT of the head and neck, part 2: clinical applications. AJNR Am J Neuroradiol 30:1285-1292

48. Park SH, Goo JM, Jo CH (2004) Receiver operating characteristic (ROC) curve: practical review for radiologists. Korean J Radiol 5:11-18

49. Peltonen LI, Aarnisalo AA, Kaser Y, Kortesniemi MK, Robinson S, Suomalainen A, Jero J (2009) Cone-beam computed tomography: a new method for imaging of the temporal bone. Acta Radiol 50:543-548

50. Peltonen LI, Aarnisalo AA, Kortesniemi MK, Suomalainen A, Jero J, Robinson S (2007) Limited cone-beam computed tomography imaging of the middle ear: a comparison with multislice helical computed tomography. Acta Radiol 48:207-212

51. Penninger RT, Tavassolie TS, Carey JP (2011) Cone-beam volumetric tomography for applications in the temporal bone. Otol Neurotol 32:453-460

52. Pujol, S. Data Loading and 3D Visualization in Slicer 4.1. 2012.
Ref Type: Slide

53. Ribeiro S, Mascarenhas N, Salina F, Cruvinel P (2007) Noise reduction on CT Set of Projections by Wiener Filtering and Wavelet

Thresholding. Workshop de Visão Computacional

54. Robinson S, Suomalainen A, Kortesniemi M (2005) Mu-CT. Eur J Radiol 56:185-191

55. Saint-Gobain Crystals. A scintillation crystal surrounded by various packaged scintillation products. 2008. Wikimedia Commons.
Ref Type: Art Work

56. Schafer S, Stayman JW, Zbijewski W, Schmidgunst C, Kleinszig G, Siewerdsen JH (2012) Antiscatter grids in mobile C-arm cone-beam CT: effect on image quality and dose. Med Phys 39:153-159

57. Shin JY, Song HS, Koo JW, Lee HS, Kim JS (2009) Abnormal vestibular evoked myogenic potentials in medial medullary infarction. J Clin Neurol 5:101-103

58. Siewerdsen, J. Assessment of Image Quality. C. Image Quality in Flat-Panel Detector CT. 2008. Toronto, RSNA 2008 Annual Meeting. Categorical Course in diagnostic radiologiy physics. CT and MR imaging. RC 232.
Ref Type: Report

59. Siewerdsen, J. Lecture on CT technique. 2011. iStar Lab Johns Hopkins.
Ref Type: Audiovisual Material

60. Siewerdsen JH, Daly MJ, Bakhtiar B, Moseley DJ, Richard S, Keller H, Jaffray DA (2006) A simple, direct method for x-ray scatter estimation and correction in digital radiography and cone-beam CT. Med Phys 33:187-197

61. Siewerdsen JH, Jaffray DA (2000) Optimization of x-ray imaging geometry (with specific application to flat-panel cone-beam computed tomography). Med Phys 27:1903-1914

62. Strobel N (2008) Imaging with Flat Detector C-arm systems. Siemens AG

63. Tavassolie TS, Penninger RT, Zuniga MG, Minor LB, Carey JP (2012) Multislice computed tomography in the diagnosis of superior canal dehiscence: how much error, and how to minimize it? Otol Neurotol 33:215-222

64. US News and Health Report. US Best Hospitals 2011-12. http://health.usnews.com/best-hospitals/rankings . 7-16-2011.
Ref Type: Online Source

65. van der Marel KS, Verbist BM, Briaire JJ, Joemai RM, Frijns JH (2012) Electrode Migration in Cochlear Implant Patients: Not an Exception. Audiol Neurootol 17:275-281

66. Vandenberghe B, Jacobs R, Yang J (2007) Diagnostic validity (or acuity) of 2D CCD versus 3D CBCT-images for assessing periodontal breakdown. Oral Surg Oral Med Oral Pathol Oral Radiol Endod 104:395-401

67. Vanspauwen R, Salembier L, Van den Hauwe L, Parizel P, Wuyts FL, Van de Heyning PH (2006) Posterior semicircular canal dehiscence: value of VEMP and multidetector CT. B-ENT 2:141-145

68. Welgampola MS, Carey JP (2010) Waiting for the evidence: VEMP testing and the ability to differentiate utricular versus saccular function. Otolaryngol Head Neck Surg 143:281-283

69. Welgampola MS, Migliaccio AA, Myrie OA, Minor LB, Carey JP (2009) The human sound-evoked vestibulo-ocular reflex and its electromyographic correlate. Clin Neurophysiol 120:158-166

70. Welgampola MS, Myrie OA, Minor LB, Carey JP (2008) Vestibular-evoked myogenic potential thresholds normalize on plugging superior canal dehiscence. Neurology 70:464-472

71. Wikimedia. Basic appearance of an x-ray tube. 10-4-2010. Wikimedia Commons.
Ref Type: Art Work

7. Figures and Tables

7.1. Figures

7.2. Tables

8. Abbreviations

ALARA	As Low As Reasonably Achievable
aVOR	angular Vestibulo-Ocular Reflex
CBCT	Cone Beam Computed Tomography
CI	Cochlear Implant
CT	Computed Tomography
CTDI	Computed Tomography Dose Index
cVEMP	cervical vestibular evoked myogenic potential, also 'cervical VEMP'
DICOM	Digital Imaging and Communications in Medicine
DQE	Detector Quantum Efficiency
FDD	Focus to Detector Distance
FID	Focus to Isocenter Distance
FOV	Field of View
FPD	Flat Panel Detector
EMG	Electro Myography
HA	Hydroxylapatite
HIT	Head Impulse Test
HR-CT	High Resolution Computed Tomography
HU	Hounsfield Unit
IRB	Institutional Review Board
MIP	Maximum Intensity Projection
mIP	Minimum Intensity Projection
MPR	Multi Planar Reconstruction
MSCT	Multi Slice Computed Tomography
MTF	Modulation Transfer Function
NEQ	Noise Equivalent Quanta
NIH	National Institutes of Health
PACS	Picture Archiving and Communictaion System
ROC	Receiver Operating Characteristic
ROI	Region of Interest
SCDS	Superior Canal Dehiscence Syndrome
SCM	Sterno-Cleido-Mastoid muscle
SFOV	Scan Field of View
SID	Source to Image Distance
SNR	Signal to Noise Ratio
SPL	Sound Pressure Level (120dB (SPL) ≙ 20 Pa Sound Pressure ≙ 1 W/m^2 Sound Intensity)
SPR	Scatter to Primary Ratio
oVEMP	ocular vestibular evoked myogenic potential, also 'ocular VEMP;
VEMP	Vestibular Evoked Myogenic Potential
VOG	Videooculography
VOR	Vestibulo-Ocular Reflex